AES/TG/13-19

Facies and permeability prediction based on analysis of core images

August 2013, **Idtz S. Wieling**

Thesis Committee

Principal Tutor	:	Dr. G. J. Weltje
Supervisor	:	Ir. M. R. Bloemsma
Committee Member	:	Dr A. Barnhoorn
Committee Member	:	Prof. Dr. S. M. Luthi
Committee Member	:	Dr. E. van de Graaff

TU Delft Delft University of Technology

Challenge the future

Title	:	Facies and permeability prediction based on analysis of core images
Author(s)	:	Idtz S. Wieling
Date	:	August 2013
Professor(s)	:	Dr. G. J. Weltje
Supervisor(s)	:	Ir. M. R. Bloemsma
TA Report nr	:	AES/TG/13-19
Postal Address	:	Section for Petroleum Engineering Department of Geoscience & Engineering Delft University of Technology P.O. Box 5028 The Netherlands
Telephone	:	(31) 15 2781328 (secretary)
Telefax	:	(31) 15 2781189

Preface

The thesis presented here has been carried out as part of the MSc Petroleum Engineering curriculum. The research was performed at the faculty of Applied Earth Sciences at the TU Delft. In this thesis the viability of image analysis as a core description tool is analyzed, which is still a broadly underdeveloped technique. To me this is a very interesting new technique in which geological knowledge is combined with statistical models. I have always been interested in geology and due to my background as BSc Aerospace Engineer I wanted to combine my interests in geology with my interest in engineering. This ultimately led me to this project, which combines my two interests as it uses mathematical procedures to obtain a geological model of a drill core.

Special thanks go out to my principal tutor Gert Jan Weltje and supervisor Menno Bloemsma, who supervised the project, gave cristal clear feedback when I struggled during the process and arranged the projects logistics. Without their support and knowledge, this project would not have given the same results.

Thanks goes out to Mike Burns of Panterra Geo-consultants in Leiderdorp for letting me perform measurements on their brand new Pressure Decay Profile Permeameter. With the help of Mike Burns the measurements could not have gone any smoother as he was always available to help me out when I had troubles with the device. I would also like to thank all other employees of Panterra that assisted me during my measurements.

Thanks go out to the Royal Netherlands Institute for Sea Research (NIOZ) at Texel, who let me use their XRF-CoreScanner to analyze the cores. During my measurements at the NIOZ, I was assisted by Rik Tjallingii and Rineke Gieles, who not only introduced me to the device, but gave me a grand tour through the whole institute. Some of the measurements, which I could not perform due to lack of time, were performed by Rineke Gieles, which saved me a great amount of stress. I would like to thank both of them for their support.

I would like to thank Bert de Wijn of Wintershall Noordzee BV who made core E10-3 available for this research. Due to the many different lithologies present in this core and the overall quality of the core, the potential of image analysis could be analyzed perfectly.

Further on I would like to express my thanks to everyone I cannot thank individually who provided me with support, both technically and personally.

Abstract

The present standards for core interpretation do not contain the acquisition of high resolution images from core slabs; images are taken on a very low resolution under a poor light source for administrative purposes only. The advantages of taking high resolution images and subsequent analysis of these images could be substantial and are investigated in this project. Besides the possible advantages image analysis could have, these images provide a safe way to store core information, as they are not prone to deterioration over time, which cores themselves are.

Obtaining a high resolution description of facies and permeability by means of image analysis is a promising new technique, which could ease the operation of core analysis. This technique is relatively new because of the trend of increasing resolution of digital cameras and increasing processing power of computers, which make it possible to obtain high resolution images and process them without losing detail.

In this project a routine is developed to analyze the images and the routines accuracy is compared to the present day standards of core interpretation. The proposed routine in this project first segments the core on a centimeter scale parallel to bedding, which is performed by a correlation scheme. The segments are subsequently subjected to an image analysis algorithm. Image analysis was based on RGBD color data and its auto-covariance properties, to enable the mapping of color and texture of the core. The results of this image analysis are used to classify the core based on lithology and grain size and produce a permeability model of the core. To enhance separation between facies in terms of the RGBD color data and Auto-Covariance properties, the data undergoes a Centered Log Ratio Transformation resulting in a continuous data space. The data subsequently undergoes a Principal Component Analysis to detect the properties that are potentially informative about the facies and permeability.

Initially classification between sandstone and other lithologies was performed on the log-transformed RGBD color data, by means of a quadratic decision boundary. Subsequently analysis of the Auto-Covariance properties was performed to extract a permeability model of sandstone, which was calibrated with plug data.

The resulting classification of lithology showed to be accurate for 84 % of the segments, where the largest misinterpretation occurred between very fine sandstone, siltstone and mudstone. All but the finest sandstones grain size classes showed an accuracy of classification above 95 %.

Grain size was classified into the correct class or a similar class in terms of permeability for 55 % of the fine to medium grained sandstone. For mudstone, siltstone and coarse sandstone this percentage ranged between 93 % and 100%.

The root mean squared error of the permeability model was an order of magnitude. This error is 30 % larger than the root mean squared error of the null model, which is a model that averages permeability over the facies as interpreted by the geologist.

These results imply that image analysis could potentially be a good source of information and especially when combined with other reliable methods. The areas where image analysis is prone to

misclassification could be classified by other reliable methods; Misclassification between mudstone and sandstone could easily be extracted with a gamma ray log, for example.

The resulting map of grain size, lithology and permeability could aid the geologist during his core analysis. The initial estimation of the core's characteristics is digitalized by the image analysis routine, reducing the job of the geologist to verifying the results and adjusting them where necessary.

Declaration of variables

Variable	Name	Unit
ΔL	Correlation step size	cm
ΔV_1	Nozzle volume wrt to standard	cc
b	Klinkenberg gas slippage factor	psi
G_D	Dimensionless Geometric Factor	-
k_∞	Slip-Corrected Permeability	mD
K_a	Permeability of method A	mD
K_b	Permeability of method B	mD
$K_{fabricated\ plug}$	Permeability indicated on fabricated plug	mD
k_g	Gas permeability	mD
$K_{measured}$	Measured permeability	mD
K_{null}	Permeability of the null model	mD
K_{PDPK}	Permeability measured by the Pressure Decay Profile Permeameter	mD
K_{plug}	Hassler sleeve plug permeability	mD
L_c	Correlation length	cm
L_y	Distance from center of the core	cm
n	Degrees of freedom	-
P_1	Gauge Pressure in the probe	psig
Pa	Ambient Atmospheric Pressure	psig
P_{init}	Initial Pressure	psi
q_1	Volumetric gas flow rate at a pressure of p_1	cm^3/s
r_i	Inner probe tip radius	cm
r_o	Outer probe tip radius	cm
r_p	Pearson Coefficient	-
t	Correlation thickness	mm
T_a	Ambient temperature	K
y_n	Flow rate function of nitrogen	cm^3/s
α	Bedding direction	degrees
β	Coefficient of interital resistance	ft^{-1}
σxy	Variance	mD^2
μ_g	Gas viscosity	cp
X^2_{bias}	Chi Squared of bias	-
$X^2_{scatter}$	Chi Squared of scatter	-
X^2_{tot}	Total Chi Squared	-

Declaration of Figures

Declaration of Tables

Table of Contents

1. Introduction

In this chapter a general introduction to core drilling is given, where some of the typical present day standards are mentioned. Next the current workflow for core analysis is discussed. To get an idea how the results of core analysis are used, the implications of the core analysis on the subsurface are mentioned. At the end of this chapter the goal of this research is given.

1.1. General

Over 150 years ago the diamond core drill debuted in the oil industry, granting the possibility to obtain a significant physical representation of the hydrocarbon reservoir and cap rock at the surface. The core drill is in its simplest form a drill bit without a center (Figure 1); this way the center (core) of the bore hole is (sometimes partially) conserved and can be taken to the surface for further investigation. This core is one of the most substantial physical samples from the subsurface that provides a great deal of information; other information obtained from the subsurface includes borehole logging data, seismic data and drill cuttings.

At the present time it is common practice to insert the core directly after being drilled into a sleeve to protect it against the borehole environment and subsequent transport hazards, and to facilitate the overall surfacing of the core.

Figure 1: a PDC core drill bit. Source: www.globalsources.com

A typical diameter of a core is 75 mm and can reach lengths up to 100 meter, depending on rock type and tools used. The drill core gives a great insight into the properties of the subsurface; these properties include but are not limited to lithology, permeability, porosity, wettability, saturation, pore structure, age, weathering and metamorphism. A large deal of these properties can only be measured on a physical representation of the subsurface, either in the form of a percussion sidewall core or a drill core. The lithological and petrographical information that is obtained from cores is thus invaluable in the creation of a subsurface model by a reservoir geologist.

The advantage of a drill core over other physical samples of the subsurface is large. For example drill cuttings do not preserve the pore structure nor give insight in the saturation or wettability of the rock. Sidewall percussion plugs do give insight in pore structure and wettability, but they do not grant a continuous representation of the subsurface, which drill cores do. Thus a drill core is the only physical sample that is both continuous and structurally intact.

It should come as no surprise that oil companies go to great lengths to obtain core samples of their (potential) reservoirs; the price of obtaining a drill core can range up to tens of millions US dollar for the coring of a single well (large depth, offshore).

1.2. Conventional core analysis workflow

When a core has been drilled and extracted from a well, it is conventionally taken to a core laboratory in meter long sections. At the core laboratory the core segments are taken out of their sleeve and are subjected to Spectral Gamma Ray Surface Logging. The Gamma Ray Surface Log is compared to the Gamma Ray Well Log to double check the correct depth and orientation of the core segments and make adjustments where needed.

Next, core sections are chosen to be preserved, the preservation process keeps the sample as close to the natural state as possible. Different preservation techniques are used, depending on subsequent measurements (Special Core Analysis) that are planned for the samples. The following techniques are typically used:

- Preservation in simulated formation brine (water zone) or kerosene (oil zone). Either stored deoxygenated and pressured or under ambient conditions.
- Wax coating of sample.
- Wrapping the sample in cling film and frozen solid in CO_2 (typical for unconsolidated samples).

All core segments that are not chosen to be preserved undergo a further analysis: core plugs are drilled at (relatively) homogenous intervals, either parallel (horizontal plugs) or perpendicular (vertical plugs) to stratigraphic layers (= rock layers). A horizontal plug is typically drilled every foot if the core allows this, meaning that the core is not damaged or likely to be severely damaged by extracting the plug. Vertical plugs are drilled at interesting/important intervals, such as near possible flow boundaries in the reservoir rock or cap rock. Plugs typically have a diameter of 1 or 1.5 inch, but sometimes full core diameter ‘plugs’ are extracted when conventional plug sized samples are not representative in terms of petrophysical properties. In Figure 2 some typical core plugs are visible.

Figure 2: Conventional Core plugs. Source: www.lithicon.com

After cleaning and drying of the plugs, the plugs undergo a thorough analysis. During this analysis the petrophysical properties of the plugs are measured. One of the experiments that is typically performed is the Hassler sleeve experiment to obtain the permeability of the plugs. This experiment is performed using nitrogen gas, which measures the gas permeability of the rock.

When the core plugs have been drilled, the remainder of the core is slabbed (i.e. cut into 3 segments longitudinally). The middle section of this slabbed core is set into meter long trays, correctly labeled and finally resin is poured into the tray to keep the core from moving. An example of this slabbing process can be found in Figure 3.

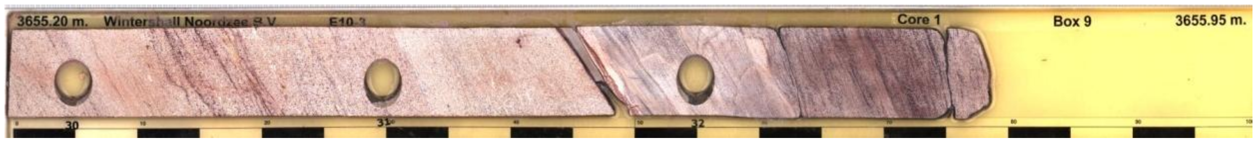

Figure 3: Example of a slabbed core, cast into yellow resin. A Depth marker, labels and a scale are visible. The three holes in the slabbed core are locations where core plugs have been taken out for porosity and permeability analysis.

A geological interpretation of the slabbed core is created by a geologist and together with the results of log and plug measurements a full core description is created. A geologist typically interprets the core in terms of facies, grain size and paleo-environment. The detail with which the geologist interprets the core is based around the company standards and the specific project. This interpretation could reach a sub centimeter resolution if deemed necessary and cost efficient, though a resolution of 5 cm is more common. To create the permeability model of the core, the geologist uses the results of plug analysis. Permeability, obtained from the plug analysis is analyzed for each interpreted facies. This results in a permeability distribution for each facies.

1.3. Implications of core analysis on the reservoir model

Reservoir engineers create a reservoir model that gives the best representation of the subsurface by using all available data and combining this into a model which could predict the static and dynamic behavior of the reservoir. This reservoir model acts as the basis of further exploration and production of a reservoir as it gives insight into the response of the reservoir on potential future wells and production patterns. The choice of producing a reservoir or not is thus based around the results obtained by this reservoir model. The reservoir models should be as accurate as possible to find the most cost efficient production method.

A reservoir model is built from seismic data, well log data, the data obtained by core analysis and at a later stage well test- and production data. The structure of the reservoir is extracted from seismic data, which typically has a vertical resolution in the order of meters, whereas the horizontal resolution of seismic data is in the order of tens of meters (*Branets et al, 2009*). Due to this resolution difference and the assumption that within stratigraphic layers the petrophysical properties remain relatively constant the grid blocks in the reservoir model are typically 10 to 100 times larger in horizontal direction compared to the vertical direction.

To capture the very low scale heterogeneities in complicated reservoirs, the (fine-scale geo-cellular) reservoir models typically consist of $10^6 - 10^8$ grid blocks. Geostatistical methods are often used to populate the model with piecewise constant properties that honor known or inferred statistics. Such a fine-scaled model can typically capture geological variations in the order of a foot vertically and a few hundred feet horizontally. Heterogeneities at a smaller scale can have a significant impact on the reservoir performance *(Coll et al. 2001* and *Honarpour et al. 1994*) and thus accurate up-scaling of the petrophysical properties to grid block resolution is necessary.

The petrophysical properties obtained from plug analysis are used during the up-scaling process, though the properties of plugs are controlled by mm- to cm-heterogeneities. To ignore these small scale heterogeneities, a model for each facies is made separately. Each facies model predicts the petrophysical properties and their variation of a facies based on the plug and log data.

This technique is rather crude, because the assumption is made that the variation of the petrophysical properties is only caused by (sub-) plug scale heterogeneities and not by variation between stratigraphic layers with similar facies. Reservoir engineers are used to the idea that each facies can be represented by a set of petrophysical properties and their variation which simplifies the up-scaling process, but does not necessarily increase the accuracy of the overall model.

1.4. Possible improvements

Wouldn't it be nice if petrophysical properties could be estimated at a higher resolution than the plug interval? This could enable the reservoir engineer to estimate the petrophysical properties and their variation at the resolution of stratigraphic layers, instead of estimating the properties per facies. This would make the subsequent up-scaling process to grid block resolution more accurate, because the grid block size could be changed for each stratigraphic layer separately depending on the internal variation of the petrophysical properties, resulting in a variable grid block size that decreases internal variation within a grid block.

Obtaining the petrophysical properties at a very high resolution could also benefit future reservoir models, where the trend of increasing computational power of computers results in reservoir models with constantly decreasing grid block sizes.

The effect of increasing computational power has been described by Moore's Law (*Moore, 1965*); this 'law' is based on historical data that indicates that on average the chip performance doubles every two years. Experts (*Kanellos, 2005*) believe that in the future computational performance would double every three years or so (disregarding the upcoming nano-computers). In the time it takes to explore, develop, produce and decommission a hydrocarbon field (>30 years) the computational power of computers could increase by a factor 1000. Grid block size could thus be decreased by such an extent that the resolution of present day core data is not adequate.

The idea that the data from core analysis should not have the highest resolution possible is primarily an artifact of past reservoir modeling standards, where obtaining data at a grid block scale is deemed adequate. Though low resolution core data can never be converted to high resolution data, whereas high resolution data can be converted to a lower resolution; thus obtaining a high resolution interpretation of a core in terms of its petrophysical properties can only be beneficial to (present and future) reservoir models.

Another problem that the oil industry faces is that different companies maintain different standards when it comes to the classification of rocks. For example, there are multiple grain size classification standards (e.g. International and US standards). When hydrocarbon fields are sold to companies that use different standards, the process of adapting the interpretation is cumbersome and errors can easily occur. It would be much better if this would either be standardized worldwide or if the initial properties are measured with such a high accuracy that it is possible to classify them at a later stage. For grain size classification this second method implies that the grain size is measured accurately and assigned a classification at a later stage instead of directly classifying the grain size into a group.

This research will investigate the possibility of extracting lithology, grain size and permeability on a high resolution using image analysis. This could aid standardization of the grain size classes and the higher resolution will be helpful for (future) reservoir models.

1.5. Research Goal

To drill a core from the subsurface is an expensive and time-consuming process; any additional data that can be obtained from the core could possibly improve the interpretation. The goal of this research is to evaluate the potential of image analysis on core images in terms of its capability to interpret the core on a sub-plug scale resolution.

Presently core images are already taken and stored, though merely for administrative purposes where a camera and light source of poor quality are used. The extra effort it takes to increase the quality of these images is small and the benefits could be substantial.

The advantages of image analysis on core analysis are obvious, as image analysis is a non-destructive method of cheap, high resolution data acquisition, which does not need any human intervention except for initial calibration. The results of image analysis could aid the geologist in his interpretation and simplify digitalization of the core analysis results.

This research will focus on the interpretation of some of the most important properties of a core that are presently assigned by a geologist. The properties that are evaluated in this research are:

- Bedding direction
- Lithology
- Grain size
- Permeability

Based on the results of the extracted properties, a new core analysis workflow will be proposed.

1.6. Approach

To be able to assess the potential of core image analysis on extracting certain characteristics from the core, a method of extracting these characteristics and analyzing the results is needed. A short overview of the method proposed in this research is given in this chapter.

First a set of images of a core need to be acquired. Subsequently these images undergo an image analysis routine to extract the bedding direction, lithology, grain size and permeability.

1.6.1. Bedding direction

To extract the direction of bedding, a routine that correlates sets of two parallel lines in the downcore direction is proposed. The results of this correlation will be analyzed by statistical tools to obtain the intervals at which the bedding direction can be determined. Further interpolation of the extracted bedding directions will result in a continuous record of the bedding direction over the full core.

The assignment of a bedding direction is reviewed visually, because no reliable description of this bedding direction is available for this core. The focus during the evaluation of the bedding direction will lie on the detection of discontinuities, the overall detection of boundaries between stratigraphic layers and the errors caused by interpolation.

1.6.2. Lithology

The lithology is extracted at a centimeter interval, to obtain a high resolution model of the core. The choice of a centimeter interval is arbitrary, where the assumption is made that within a centimeter interval the characteristics of the rock sample are relatively constant. The determination of lithology will be based around the average RGBD color and Auto-Covariance properties. The classification will be performed by a model that is calibrated on (a part of) the core interpretation of the geologist.

The classification of lithology will be compared to the geologist's interpretation of the core. The interpretation of the model is evaluated for each facies (or grain size group) observed by the geologist. The result of this comparison is a percentage of correctly classified lithologies per facies. It is chosen to evaluate per facies instead of per lithology, because this will give more insight into the misclassification of the routine.

1.6.3. Grain size

The grain size class is extracted at a centimeter interval as well. The grain size class is extracted by evaluating the texture of the core image; this texture is extracted by an Auto-Covariance function. Emphasis will be on determining the grain size class of sandstone, as this will influence the subsequent permeability analysis of the core the most.

The classification of grain size is compared in a similar manner as the lithology; it is compared against the geological interpretation for each grain size group. Because some grain size groups are relatively similar in terms of permeability, a misclassification between two similar classes can be seen as less severe; to be able to assess the similarity in terms of permeability between the different grain size groups a ranked sum test will be performed. The results of this ranked sum test will be used to compare the classification of the model against the geologist's interpretation of facies. This will lead to a percentage of grain sizes that is correctly classified, less ‘severely’ misclassified and ‘severely’ misclassified.

1.6.4. Permeability

Permeability is extracted using two different techniques. The first method (A) will act in a similar way as a geologist. For each facies identified, an average value for permeability is extracted from the plug data. Subsequently this average permeability is assigned to each segment interpreted as the respective facies.

The second method (B) will be based around the fact that grain size and permeability show a strong relationship. A relationship between a proxy for grain size (namely: an Auto-Covariance function) and permeability will be extracted from the plug data and subsequently this relationship will be applied to the whole core. This second method has a continuous relationship between the grain size proxy and permeability, instead of the first method which will assign each facies with a similar value for permeability.

To assess the accuracy of the permeability estimation across the core, the permeability estimations of the models will be compared to the Hassler sleeve plug permeability and the permeability obtained with the Pressure Decay Profile Permeameter (PDPK). The PDPK measurements were performed to obtain an independent means of validating the results, because all models are dependent on plug data due to calibration on the plug data.

The permeability estimation will be analyzed per facies, where for each facies a Root Mean Squared Error (RMSE) will be calculated; a RMSE has the advantage that it represents the error in the same unit as the input data. This RMSE will be compared to the RMSE of a null model. This null model assigns a facies’ average permeability to each facies across the core as interpreted by the geologist, which is similar to the facies models that are used in reservoir models.

The second method to analyze the permeability estimation is by means of a chi-squared variation test. This test will be performed on the facies interpreted by the geologist. The chi-squared variation test will provide a means of comparing the total error, the error caused by bias and the error caused by scatter to the error caused by the null model (which is unbiased by definition). More detail about the chi-squared variation test can be found in Appendix F.

2. Literature / Theoretical Framework

This chapter will discuss the present day operations of core handling. This includes the classification of a core and the extraction of petro-physical properties. After this a summary of previous studies on similar subjects will be given.

2.1. Conventional core analysis

Core analysis is a tool to obtain an understanding of the subsurface and this forms the base of conventional core analysis. The main purpose of core analysis is obtaining an understanding about the subsurface in terms of the rock type and its geological characteristics. These are obtained by analyzing the core and log data. Some of the important characteristics that are extracted from the core by a geologist are: lithology, grain size and shape, cementation, fossils, sedimentary structure, paleo-environment and diagenesis (*Tucker, 2001*).

Most of these characteristics are extracted by a visual interpretation by the geologist, though grain size is typically extracted by other techniques. Grain size extraction techniques that are commonly used are microscope analysis of thin sections or a scanning electron microscope (*Tucker, 2001*). The choice between these techniques depends on rock type and necessary accuracy. After the geological characteristics have been extracted, different facies can be assigned to each section.

A facies is a body or packet of sedimentary rock with features (for example: grain size, texture, lithology, fossils and color) that distinguishes it from other facies. A facies is the product of deposition, and it may be characteristic of a particular depositional environment or a particular depositional process. For each facies the petrophysical properties are extracted by means of plug or log analysis; the most important petrophysical properties being: porosity, (relative) permeability and wettability.

The results of the core analysis is a core description, which describes the full core in terms of lithology, grain size, facies, permeability, porosity, wettability and other properties that are deemed important for the particular core.

The facies model of the geologist gives information about the depositional environment and possible structures of the facies, which is used to create and populate the reservoir model. By using seismic data, a rough shape of the reservoir is available; this data is calibrated with the core data in terms of depth (where strong seismic signals can be linked to change in lithology). The reservoir model is subsequently filled with facies and their respective petrophysical properties by means of geo-statistics to obtain a full reservoir model.

2.2. Sedimentary rock characteristics

A core is a very small portion of the overall subsurface, for this reason the properties that are extracted from a core are highly influenced by local heterogeneities. For example, a large pebble in the core could give a wrong facies interpretation in terms of porosity, permeability and grain size. The effects are typically mitigated by averaging per facies across the core to obtain a distribution for each of the petrophysical properties (*e.g. Fanchi, 1997*). Heterogeneities appear in different scales and types; from a very small scale (grain size scale) to a very large scale (reservoir scale), however heterogeneities are most common on a small scale. Examples of heterogeneities are: thin layers with different properties, anisotropy, local cementation, diagenesis of sediment, coarsening of grain size, bioturbation and fossils. Heterogeneities are visually characterized by grain size, texture and color.

Studies have been performed to extract these visual characteristics from sediment images and/or classify a core automatically by using (amongst others) these characteristics. The next section gives some insight in the studies performed in this area.

2.3. Previous Studies

2.3.1. Classification based on image analysis

A previous study that classifies a core based on analysis of core images tries to extract the color and texture from the images (*Thomas et al, 2011*). These properties are subsequently used to classify the core based on a training set of data. The training set of data is extracted from the geologist interpretation.

This study then segments the image in an object-based image analysis methodology, where adjacent similar pixels are grouped based on color; groups are subjected to a similarity analysis to add similar groups. When the similarity reaches a threshold, the grouping is halted and a training set is prepared. A classification of the textural and color properties of the image is made and subsequently the full core is classified based on the training set; the classification comprises of shale, sandstone and limestone. This method was able to extract small layers and based on a core that was analyzed with this technique, this method was able to classify 95 % of the intervals correctly into one of the three lithologies.

The authors emphasize that the training set should be carefully chosen, in such a manner that all the lithologies are represented in the classification. The authors also emphasizes that the set-up used to acquire the images can cause errors (i.e. shadows or fluctuating light sources) and the background color of the core slabs can cause wrong interpretation as well. In their case the background color is white, which can cause problems as it is similar to the color of limestone.

2.3.2. Obtaining grain size from images

Interpretation of sediments based on images is not only restricted to the analysis of core slabs, the extraction of grain sizes from images of loose sediment has previously been considered as well. There are basically two ways of extracting the grain size of an image; the first technique uses an object-based image analysis technique, where individual grains are extracted by tracing the edges of the grains. This technique has been evaluated by *Butler et al. (2001)* and *Baptista et al. (2012)*. The extracted grain sizes are converted into a grain size distribution by performing 2D to 3D conversion. This technique requires that each grain is imaged at a resolution of at least 10x10 pixels per grain, otherwise it is impossible to trace the edges of the grains as the images become blurry. For this reason it is complicated to extract the grain size from fine grained sediment, as the resolution of images becomes too low. Other problems that arise when using this technique are based around its grain size acquisition: grains can be overlapping, where the size of an individual grain can be underestimated as they are not fully visible and grains can have similar color characteristics, which leads to edges between grains that are impossible to detect. Both these factors lead to an overestimate of the grain size.

The second technique that can be used to extract the grain size from sediment images examines the texture of the image. With the aid of a calibration the grain size can be estimated from the texture. To obtain the texture of an image an auto-correlation function can be used, this technique has been examined by *Rubin et al. (2004)*. This study performs auto-correlation on small rectangular section of the image (‘plaquettes’). The auto-correlation function will be close to one when the offset is smaller than the grain size and will reach zero at an offset of approximately the size of the largest grain. Further on the shape of the auto-correlation function will give some insight on the shape of the grain size distribution. This technique can be used to analyze sediment with a finer grain size than the previous technique; it will require a resolution of 1 pixel for the smallest grain present in the image. A disadvantage of this technique is that it requires calibration on a training set that represents the grain color, mineralogy, packing and shape of the grains.

Another technique that tries to estimate the grain size based on the texture of an image has been proposed by *Buscombe (2013)*. This technique uses a global wavelet power spectrum to estimate the grain size of loose sediment. Buscombe claims that this technique is very efficient, because it uses both the spatial and spectral information that can be obtained from the image.

2.3.3. Automated log interpretation

Other studies that consist of automated interpretation of a core are mainly based on analysis of the well logs. A well log is the result of measurements that are performed downhole in a well, either simultaneous with the drilling or at a later stage. Some well logs that are commonly acquired are: Gamma Ray (GR), Resistivity (RT), Spontaneous Potential (SP), Neutron Density (NPHI) and Sonic interval transit time (DT). Interpretation of the log-data has historically been performed by using empirical formulas. Due to the complexity and diversity of reservoirs this technique can be flawed as an empirical formula is not applicable to all reservoirs without the aid of a proper calibration.

Statistics show another way to interpret log data, which is commonly performed by a multiple regression. In its simplest form multiple regression estimates a relation between the log data and the petrophysical properties, the derived equations are subsequently applied to a model that interprets the log data in terms of lithology and petrophysical properties. This technique, however, needs to be calibrated in order to give satisfying results. Another technique used in log interpretation is the Artificial Neural Network (ANN) approach evaluated by *Akinyokun et al. (2009)* and *Wong et al (1999)*, this approach uses a set of formulas to interpret log data, but instead of using fixed formulas the technique adjusts the weights of each formula to obtain the ‘best fit’ solution. This means that the program is able to learn while it processes information. These neural networks are trained using fuzzy logic, which results in a likelihood for each possible interpretation per observation. For example an observation could belong for 20% to sandstone and 50% to mudstone, making it possible to ‘soft classify’ the data.

Another proposed technique for automated log interpretation by *Delfiner et al. (1987)* is classification based around the Bayesian decision rule combined with an artificial intelligent method. Classification is performed on the basis of a large database of ‘known’ classifications, where levels of log responses are assigned to a specific lithology.

3. Proposed Method

This chapter introduces the proposed method to extract properties by means of image analysis which are subsequently used to classify the core. This chapter will first focus on the drawback of the current workflow; next the physical requirements of the proposed method are discussed. At the end of this chapter a workflow of the proposed method and a means of evaluating the results of the proposed method are given.

3.1. Drawback of current workflow

The current workflow assumes that the differences of the permeability measurements within a facies are all caused by local heterogeneities or measurement errors. These differences, however, can also be caused by reservoir sized heterogeneities either in vertical or horizontal direction. The permeability and porosity can show a trend across depth, which is neglected when using a single distribution per facies. The data that are available can, however, give information about these trends. In the current workflow, a permeability measurement is performed every 30 cm across the whole core, which makes the extraction of these trends quite cumbersome (especially when local heterogeneities play a large role).

If the permeability could be mapped at a centimeter interval, the local heterogeneities become much more apparent. Using a permeability map with such a high detail leads to a better representation of the facies with regard to the permeability distribution and could potentially lead to the extraction of permeability trends within a facies.

3.2. Requirements of new workflow

To be able to obtain a permeability map with high resolution, a workflow is proposed that includes taking high resolution core images and performing image analysis on them. The main difference with the current workflow is that the core images taken conventionally during the core description phase need a higher resolution and should be taken under a controlled light source. This would result in core images on which quantitative analysis could be performed, instead of having core images for the sole purpose of administration. If the resolution of these images is high, the images could hold the same information as the core slabs themselves hold (except for smell and feel), making the core itself obsolete in terms of geological interpretation. A secondary advantage of this method is that the images could be send to any place on earth in a very short amount of time. Further on, storage of the images would be very safe and effective and (digital) images do not degrade over time.

The high quality core images could undergo an image analysis to extract the color and texture of the core. The classification of the core based on the extracted properties can be automated when a calibration set for each of the facies present in the core is available. These calibration datasets can either be a core description from a neighboring well or a plug analysis (including lithology and grain size) of the core itself.

3.3. Image analysis and classification workflow

The problem of interpreting the core images in terms of lithology, grain size and permeability is tackled stepwise. The results of each step will be the basis of the next step. To be able to visualize this process in a structured manner, this section introduces a workflow. This workflow will act as handles in subsequent chapters.

3.3.1. General

A workflow diagram of the image analysis and classification process is shown Figure 4. The workflow is split up into five segments: Input data (0. white), preparation of core images (1. green), interpretation method A (2. gray), interpretation method B (3. blue) and results (4. red). The following sections give a short description of the function of each of these segments.

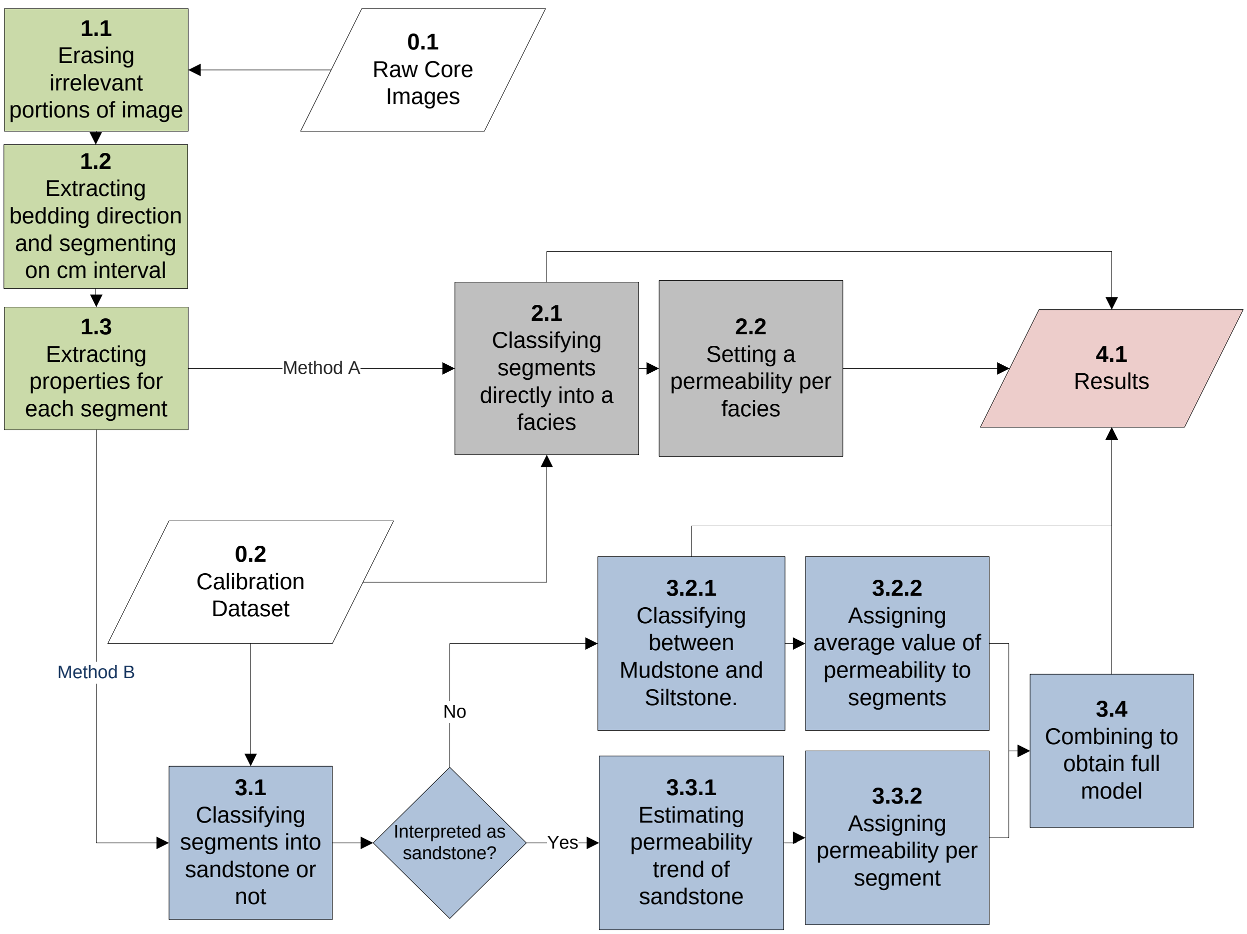

Figure 4: Workflow diagram of the project.

3.3.2. Input

The automated geologist requires input data in the form of core images (0.1) to be able to interpret the core accordingly. Besides the core images, a dataset to calibrate the program is needed (0.2). For method B this dataset is built from plug data, which is used to calibrate the properties that are obtained through image analysis on permeability, grain size and lithology. For method A the calibration dataset used is the full interpretation of the core made by the geologist.

3.3.3. Preparation of core images

The permeability, grain size and lithology will be predicted at a high resolution, for this reason it has been chosen to split the core up into centimeter scale intervals that are parallel to bedding. The image preparation process starts by discarding all the portions of the core images that do not contribute to the interpretation. This results in an image that solely contains rock samples, meaning that the background of the image should be discarded. This is performed by process 1.1 in Figure 4. Secondly the actual segmentation is performed by process 1.2 in Figure 4. When the core is divided into segments, the properties of each segment needs to be extracted. Process 1.3 in Figure 4 will extract the relevant properties from each centimeter thick segment individually.

3.3.4. Interpretation method A

The first method that is chosen to interpret the core is inspired by the conventional method which geologists use to interpret a core; the facies of each segment in the core is determined and the average permeability for each facies is calculated from plug data and assigned to the relevant segments. The main difference from a geologist's interpretation is that the automated geologist considers each centimeter thick segment separately and not as a continuum as a geologist would be able to do. Assigning facies to the centimeter thick segments and assigning a value for permeability to each facies takes place in process 2.1 and 2.2 in Figure 4 respectively.

3.3.5. Interpretation method B

The second method is centered on the relation between grain size and permeability in sandstone. This relationship between grain size and permeability is less apparent in other lithologies (A plot of permeability against grain size is shown in Appendix A). This is the reason to classify the data into sandstone and 'other lithologies' initially (process 3.1). This second group consists of mudstone, siltstone and coal and is classified subsequently (process 3.2.1). Mudstone, siltstone and coal are assigned a permeability based on the average permeability obtained from the plug data (process 3.2.2).

Because the grain size of sandstone shows a strong relationship with permeability, the decision was made to extract a proxy for the grain size and calibrate this with the plug data, resulting in a continuous permeability-'grain size proxy' relation (process 3.3.1). The proxy used for the grain size is derived from an Auto-Covariance function, which extracts the texture of the images. A linear fit model is used to represent the relationship between the permeability and the texture of the image. Calibration of this model is performed by using plug data. The model is subsequently used to estimate the permeability of each centimeter segment (process 3.3.2). To conclude this method all the properties are combined to give a full prediction of permeability, grain size and lithology of the core.

3.3.6. Results

The output of this research is a description of the core in terms of lithology, grain size and permeability for each of the two methods. The results are evaluated as proposed in section 1.6; the lithology and grain size prediction will be compared to the geologist's interpretation of the core. The permeability estimation will be compared to a null model, this null model calculates the average permeability obtained from the plug data per facies and assigns it to the whole core.

4. Materials & Methods

This chapter gives insight in the materials and methods used in this research, first the materials used are discussed and after that a short summary of the methods will be given.

4.1. Materials

This section will give insight in the materials used during this project, which comprises of the geological core E10-3 that is analyzed, a Linescanner to obtain images, a Pressure Decay Profile Permeameter (PDPK-400^{TM}) to obtain independent validation measurements and a computing environment (MATLAB) used to built the image analysis tool and subsequently classify the data.

4.1.1. Core E10-3

The core that is analyzed in this research is core E10-3 owned by Wintershall Netherlands BV. The core has been drilled offshore near the Dutch coast (Figure 5). Core E10-3 has been subjected to a study with regard to the sedimentology, petrography and reservoir quality. This study is referred to as a core description and has been performed by Panterra BV Netherlands. The results of the study were reported by *Boels (2003).*

Core E10-3 was characterized as reflecting a deltaic system of braided rivers with varying marine influence. In this core Panterra recognized a couple of different lithofacies associations: poorly drained floodplain, floodplain, swamp, crevasse splays, interdistributary bay and braided channel deposits. Additionally they recognized a number of grain size classes, ranging from mudstone, found in the floodplains to very coarse sandstones, found in the braided river beds. An overview of the observed grain size classes is given in Table 1. A detailed description of the lithofacies associations present in the core can be found in Appendix C.

Core E10-3 consists of two cores; core 1 consists of 42 core boxes and core 2 consists of 43 core boxes. The core slabs had an average thickness of one centimeter, an average width of 75 mm and ranged in length from 30 to 90 cm.

A total of 290 horizontal plugs have been drilled from the core and 146 of these plugs have undergone a Hassler Sleeve analysis to obtain the permeability of the plugs. The plugs have a length of 2 inches and a diameter of 1 inch. The results of the plug analysis can be found in Appendix D. Multiple vertical plugs have been extracted from the core as well, but were not analyzed.

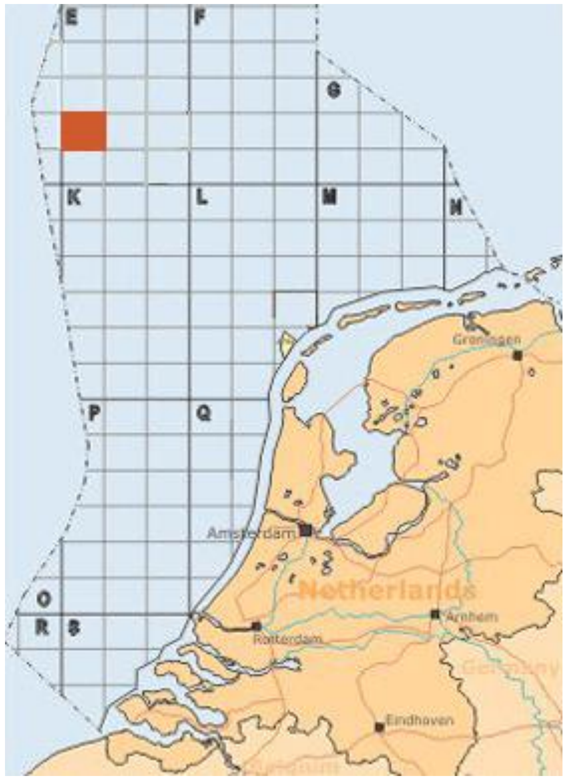

Figure 5; Location of block E-10, indicated by the red square. Source: www.tullowoil.com

Table 1: Grain size classes recognized in core E10-3

Class	**Textural Classification**	**Mean Grain Size [µm]**	**Sorting**
M	Mudstone	6	(1.6)
J	Siltstone	31	1.1
S1l	Very fine lower sandstone	74	1.5
S1u	Very fine upper sandstone	105	1.7
S2l	Fine lower sandstone	149	1.7
S2u	Fine upper sandstone	210	1.7
S3l	Medium lower sandstone	297	1.9
S3u	Medium upper sandstone	420	1.7
S4l	Coarse lower sandstone	595	2.0
S4u	Coarse upper sandstone	841	2.2
S5l	Very Coarse lower sandstone	1189	2.4

4.1.2. Linescanner

The core scanner used in this experiment, the Avaatech XRF-Core Scanner, is manufactured by Avaatech in a joint venture with Core Laboraties and is located at the NIOZ on Texel. This core scanner consists of an X-ray Fluorescence (XRF) Core Scanner and a Linescanner. Only the results of the Linescanner were used in this research.

The Linescanner is an imaging device that sweeps across a single core box at a time and takes images every few centimeters. It does so under controlled conditions; a bright mercury light bulb that produces a very constant beam of light is attached near the camera. This light beam covers an area just large enough for the camera to take an image. Each individual image is taken with a resolution of 2048x2048 pixels and with a spatial resolution of is 0.07x0.07 mm per pixel. The individual images are joined to obtain one large image per core section (typically 16400x2048 pixels) an example of an image taken by the Linescanner can be seen in Figure 6.

Figure 6: An example of a core image taken by the Linescanner.

4.1.3. Pressure Decay Profile Permeameter

A Pressure Decay Profile Permeameter (PDPK) is a device that measures gas permeability at a sub-centimeter scale. The PDPK used in this experiment is the PDPK-400^{TM} (see Figure 7), manufactured by Core Laboratories and located at Panterra Geo-consultants in Leiderdorp.

Figure 7: CoreLab's Pressure Decay Profile Permeameter. PDPK-400^{TM}. Source: www.corelab.com

The PDPK operates by placing a probe tip on the sample; the probe tip is connected by a valve to a gas storage tank. The probe tip dimensions can be adapted to fulfill specific needs; the tip can be replaced by a tip with a different inner radius. Tip radiuses r_i vary between 0.262 and 0.315 cm, and are chosen depending on the dimensions of the rock sample. In this case the smallest tip (r_i=0.262 cm) is used, because the measurements are performed on (small) core plugs and (thin) core slabs. Measurements performed with the smaller tip result in a smaller radius of influence, thus limiting the effects of the plug edges and epoxy in the slabs. The radius of influence has been estimated by *Manrique et al. (1994)* , *Dussan and Sharma (1992)* and *Goggin et al. (1988)* and were estimated at 2, 3 and 4 times the inner probe tip radius r_i respectively. A detailed discussion of the workflow and underlying theory of the PDPK can be found in Appendix E.

The PDPK can measure gas permeabilities reliably from 0.001 mD to 30 D. It is able to do so, because the pressure reservoir is automatically set to one out of three different volumes (one small gas tank, one large gas tank and the two combined), the smallest reservoir volume is used for very tight lithologies, whereas the largest reservoir volume is used for the high permeable lithologies. The main reason to use different gas tank volumes is to speed up data acquisition without losing accuracy over a wide range of permeabilities.

To be able to perform reliable measurements, the properties of the ambient air should be provided to the device; the ambient temperature T_a should be accurate to 3 degrees Kelvin and the ambient pressure P_a should be accurate to 3.5 mBar.

The placement of the nozzle on the samples can be performed either manually or automatically. The samples are placed on a translation table, which can move in Y-direction and the nozzle itself is located on a rail, which that can move in the X-direction, making it possible to perform a grid measurement on a slab without much manual intervention.

4.1.4. MATLAB R2012b

To be able to implement all the previously discussed methods into an automated geologist, a programming language is needed. Because of the size of the datasets, MATLAB is used. MATLAB, an abbreviation for Matrix Laboratories, is a numerical computing environment developed by MathWorks. It is written in C, a programming language which dates back to 1972. MATLAB allows the user to, amongst others, perform matrix manipulations, implement algorithms and plot functions/data.

4.2. Methods

The following sections will highlight all methods that are used to analyze the data. The methods will be discussed in the order they appear in the workflow of this research. The methods themselves are shown in bold and each method is discussed in more detail in Appendix F.

4.2.1. Detection of irrelevant sections in core images

To detect and delete the irrelevant sections in the core images (the yellow reflective background of the core box) a **region growing** tool was used, followed by the **morphological opening** of the selected area.

4.2.2. Extraction of sedimentary structure

To get a better separation between stratigraphic layers, the RGB data is converted to **RGBD data**. The D component in this data represents the darkness of the color.

To extract the sedimentary structure (or: bedding) in the core, each core image underwent a **centered log ratio (CLR) transformation** *(Aitchison, 1986)* followed by a **Principal Component Analysis (PCA)**. The CLR transformation enhances the separation in the high and low intensity (white and black) areas of the RGBD space and converts the RGBD-space to a continuous data space. The CLR transformed data is easier to handle when it undergoes calculations and can be converted back to its original state.

The PCA is applied to each core image separately; this is done to amplify the color difference between stratigraphic layers. The first Principal Component that is extracted from each component subsequently undergoes a routine to extract the bedding. This routine **correlates** parallel lines to extract possible bedding directions. The results of the correlation undergo a statistical analysis and to be able to extract groups of possible bedding directions it uses **k-means clustering.**

4.2.3. The extraction of texture

To extract the texture of a core image, an **Auto-Covariance** function is used. The texture of the image is considered to be a proxy for the grain size.

4.2.4. Classification

To classify the core based on the extracted features obtained from image analysis three different routines are used. The first routine is **Multivariate Gaussian Classification model** of the extracted features, which uses a **Minimum Covariance Determinant** *(Rousseeuw, 1999)* to find the Multivariate Gaussian distribution for each class (i.e. facies). The second routine is a **Quadratic Decision Boundary**, which is similar to the Multivariate Gaussian Classification, except it uses a quadratic covariance matrix. The third routine is based on the linear regression of the Auto-Covariance properties, which is used to estimate grain size and permeability. To evaluate the results of this permeability prediction, a **chi-squared variance test** is performed on the data.

5. Data acquisition

This chapter will focus on the acquisition of all the necessary data in this project. First some detail about the core images is given, after this the acquisition of permeability with the Pressure Decay Profile Permeameter is discussed. At the end of this chapter a short overview of the data of core E10-3 is shown.

5.1. Core images

Each of the core boxes has been imaged with the Linescanner, comprising a total of 85 core images. The core boxes were clamped on the rail of the Linescanner to assure a similar distance to the camera and light source. The properties of the core images can be seen in Table 2.

Table 2: Overview of the properties of the core images

Property	Value	Unit
Resolution	16400x2048	pixel
Spatial Resolution	0.07x0.07	mm/pixel
Average disk space	3.7	MB
Format	JPEG	-

5.2. Pressure Decay Profile Permeameter

The Pressure Decay Profile Permeameter (PDPK) can obtain measurements at high interval, resulting in a high resolution permeability map of the sample. The data acquisition with the Pressure Decay Profile Permeameter has been set up based on two main criteria. The first criterion is obtaining a measure of the accuracy of the device and the second is to obtain validation measurements for the introduced permeability model.

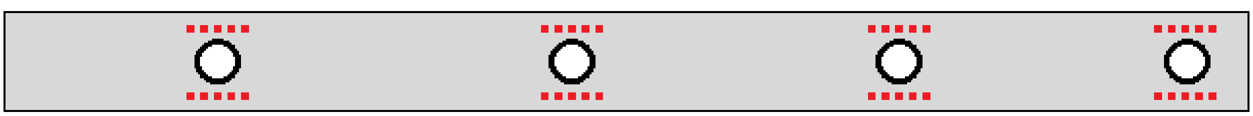

Figure 8: Schematical representation of a core slab showing the locations at which Pressure Decay Profile Permeameter measurements were performed for comparison with plug data.

5.2.1. Obtaining the accuracy of the Profile Permeameter

A set of fabricated (plastic) plugs was available to assess the accuracy and repeatability of the Pressure Decay Profile Permeameter (PDPK). This set consisted of 5 plugs, ranging from 1.27 mD to 1460 mD.

To evaluate the accuracy and reliability of the PDPK on actual rock samples, two sets of plugs were analyzed; plugs that are taken from homogeneous intervals and plugs taken from more heterogeneous intervals. This enables us to compare these measurements with the Hassler Sleeve permeability of the plugs. Permeability was measured on both flat sides of 38 plugs. The selected plugs are shown in Table 3 and more visually in Figure 9. The plugs were selected to represent a large range of permeability. An overview of all the plugs of core E10-3 can be found in Appendix D.

To assess the accuracy of the PDPK on core slabs, measurements were performed near the plug holes of the 22 plugs taken from relatively homogeneous intervals throughout the core. At each plug location a set of 10 permeability measurements was acquired to enable comparison with the Hassler sleeve plug permeability; a schematic illustration of the measurement locations can be seen in Figure 8.

Table 3: Selection of the plugs measured with the Pressure Decay Profile Permeameter and their respective Hassler sleeve plug permeability.

Homogeneous plug Nr.	**Hassler Sleeve permeability of homogeneous plug [mD]**	**Heterogeneous plug Nr.**	**Hassler Sleeve permeability of heterogeneous plug [mD]**
2	331.19	9	3.57
16	2.27	10	3.60
20	1.63	11	5.06
43	0.07	62	0.01
63	0.13	64	0.01
84	1.82	65	0.02
86	0.44	85	0.25
100	2.89	87	0.18
104	7.59	121	6.78
106	8.81	132	0.01
118	86.98	133	0.04
122	74.38	134	0.15
123	50.29	179	7.70
142	0.36	181	7.35
144	0.56	182	9.93
155	260.47	199	7.70
167	319.40	-	-
180	2.18	-	-
194	4.35	-	-
195	5.70	-	-
207	0.06	-	-
212	1.48	-	-

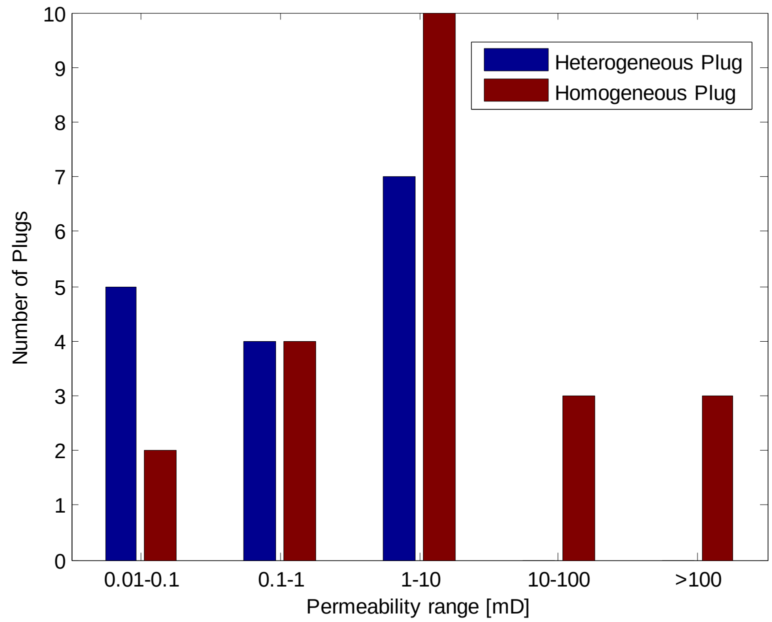

Figure 9: A bar chart illustrating the permeability range of the plugs measured with the PDPK. Permeability shown is the Hassler sleeve plug permeability.

5.2.2. Measurements to validate the model

To validate the permeability models proposed in this research, high resolution permeability measurements on the core slabs are needed. A selection of the core slabs was made to be fully analyzed with the PDPK. The decision was made to focus primarily on the core slabs that contain sandstone, because they are the most important sections when it comes to creating a reservoir model.

The core consists of three channel units; the decision was made to analyze at least one core slab per channel unit with the PDPK. Besides the channel units, sandstone was also present in the crevasse splays and poorly drained floodplains, to be able to measure this sandstone two core slabs were selected from these sections.

During the selection of representative core slabs the limitations of the PDPK need to be kept in mind; the PDPK cannot perform measurements near or on fractures, thus making it nearly impossible to obtain reliable measurements of coal (which contains many fractures). For the same reason core slabs with a large amount of fractures were unsuitable for measurements. Another limitation of the Pressure Decay Profile Permeameter is that measurements performed on low permeable samples (<0.1 mD) take much more time. Because of these constraints, it was decided to measure neither siltstone nor coal.

Seven core slabs were eventually chosen to undergo a permeability analysis with the PDPK, these core slabs are shown in Table 4 along with the facies present and the permeability range of the plugs that were taken from the slabs.

To obtain a reliable permeability map of the selected core slabs, the decision was made to measure each slab on both sides of the core plugs (illustrated in Figure 10). This analysis was performed on a centimeter scale, which lead to approximately 180 measurements per core slab.

Table 4: Facies present in the core slabs that were analyzed with the Pressure Decay Profile Permeameter. Sandstone classes range from 1 to 5 representing their grain size, where 1 is the finest grain size and 5 is the coarsest.

Core	Box	Mud-stone	Sand-stone 1	Sand-stone 2	Sand-stone 3	Sand-stone 4	Sand-stone 5	Permeability Range from Plug Data (mD)
1	3			x	x			3.5 - 5
1	18	x	x					<0.01 - 0.12
1	25		x	x				0.18 - 1.8
1	36			x	x	x		6.8 - 74
1	39		x	x				<0.01 - 0.15
2	11			x	x	x	x	2.2 - 7.9
2	23		x	x				<0.01 - 0.04

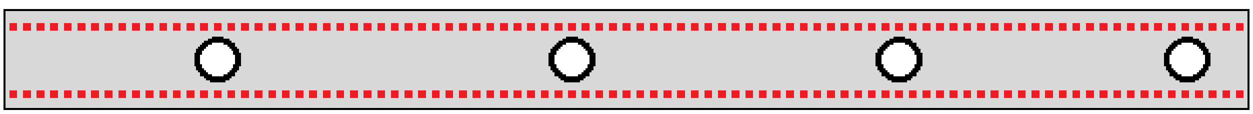

Figure 10: Schematic representation of the locations at which Pressure Decay Profile Permeameter measurements were performed for full slab measurements. These measurements are used to validate the final model of this project.

5.3. Plug Data and full core description

Calibration and validation of the models proposed in this research were performed by using the plug data and core description. A total of 290 horizontal plugs were taken from the core, but only 146 underwent permeability analysis and could be used in this research. The facies (consisting of grain size and lithology) and permeability description of these 146 horizontal plugs were used in this research. A table with all the plugs used and their respective permeability and grain size can be found in Appendix D. The part of the core description *(Boels, 2003)* that is used to calibrate and validate the models is the geological interpretation of the lithology and grain size.

6. Implementation

This chapter gives insight in the implementation of the methods. This chapter will discuss the implementation based on the workflow introduced in previous chapters (Figure 11). First the preparation of core images is discussed, after which the functionality of method A and B are discussed.

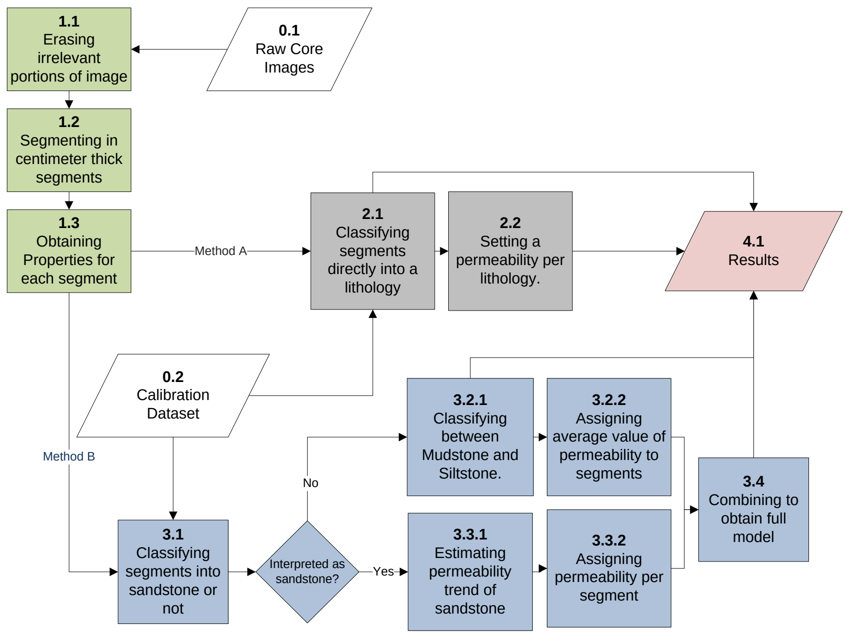

Figure 11: Workflow diagram of the project

6.1. Preparation of Core Images

6.1.1. Calibration of depth

The core images initially had to be calibrated on depth, due to the fact that the indicated depth in the core boxes did line up to the depth indicated in the geological record of the core made by the geologist. Discrepancies between the two ranges between 0 and 3 centimeter and were adjusted manually based on clear boundaries between facies.

6.1.2. Erasing irrelevant portions of the image

The core images consist of core sample, yellow colored reflective resin, a depth marker and text. Apart from the core sample itself, these portions of the image need to be extracted and discarded. The text and depth markers were selected manually; the yellow colored reflective was extracted by using a region growing technique and subsequently using a morphological opening routine on the selection. Seed points of the region growing tool are the centers of the core plugs and any other visible yellow colored reflective near the edges of the image. The final selection of irrelevant portions was visually checked and adjusted where needed. A result of this method is visible in Figure 12, where the initial core image is shown, together with a binary file and the final result. Figure 13 shows a schematic workflow of the routine that erases irrelevant portions of the image, this figure represent process 1.1 in Figure 11.

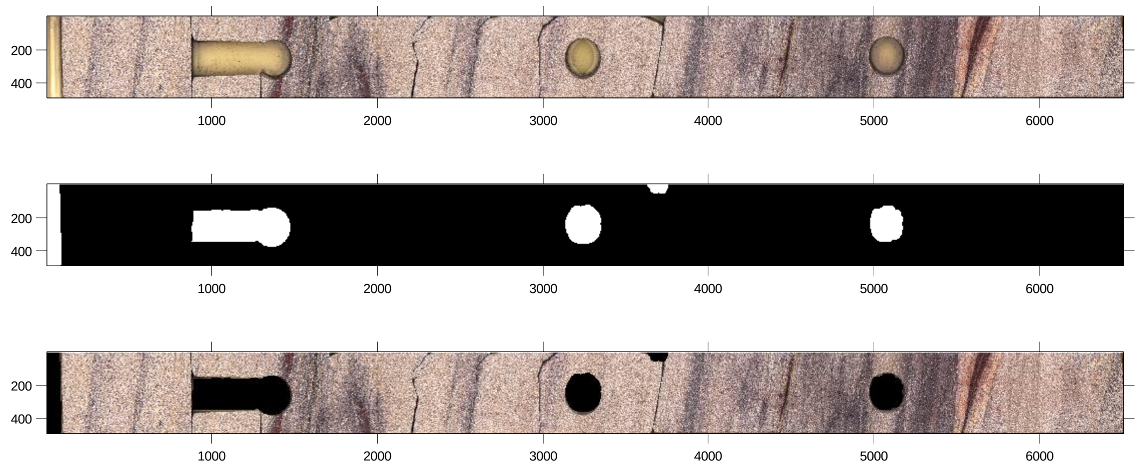

Figure 12: (top): The core image before discarding any irrelevant portions. (middle): The mask obtained after selection of irrelevant portions. (bottom): The final result after discarding the irrelevant portions.

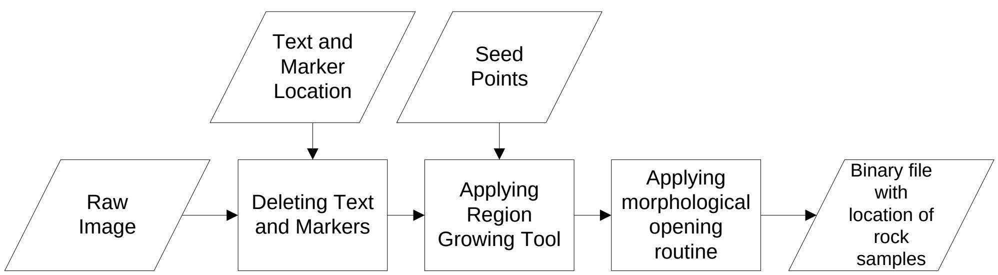

Figure 13: Detailed workflow diagram of process 1.1: Erasing irrelevant portions of the image.

6.1.3. Segmenting in centimeter thick layers

A detailed explanation of the extraction of bedding direction and subsequent segmentation of the core into centimeter thick segments can be found in Appendix G. This section will provide a summary of this technique.

The choice was made to segment the core into centimeter thick layers parallel to the bedding. This segmentation has been executed by performing a number of correlations on two lines parallel to depth across the core. Subsequently a statistical analysis was performed on the correlation results. The result of this analysis was a set of reliable bedding directions at locations where this bedding direction is obvious (for example: stratigraphic boundaries). An example of the results can be seen in Figure 14, where the extracted 'reliable' bedding directions are indicated on one of the core slabs.

At location where no reliable bedding direction could be extracted, the bedding direction was either interpolated or a second routine was used to extract the bedding direction. Interpolation has been performed when the difference between two subsequent reliable bedding directions is less than 2 degrees or when two subsequent reliable bedding directions were located in different core images.

When the difference between two subsequent reliable bedding directions is more than 2 degrees, the assumption was made that a discontinuity could be present. In these areas a routine was used that extracted the direction of least deviation in color. The results of this routine were fitted on a set of possible scenarios and the best fit was ultimately chosen. These scenarios consist of a discontinuity or a gradual change in bedding direction. The workflow of the extraction of bedding direction is schematically represented in Figure 15.

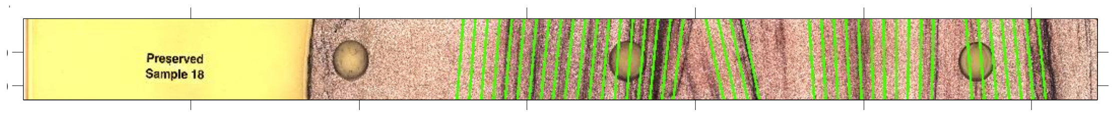

Figure 14: Results of the statistical analysis of correlation data, the lines represent the dip angles obtained from the correlation that were seen as reliable by the analysis.

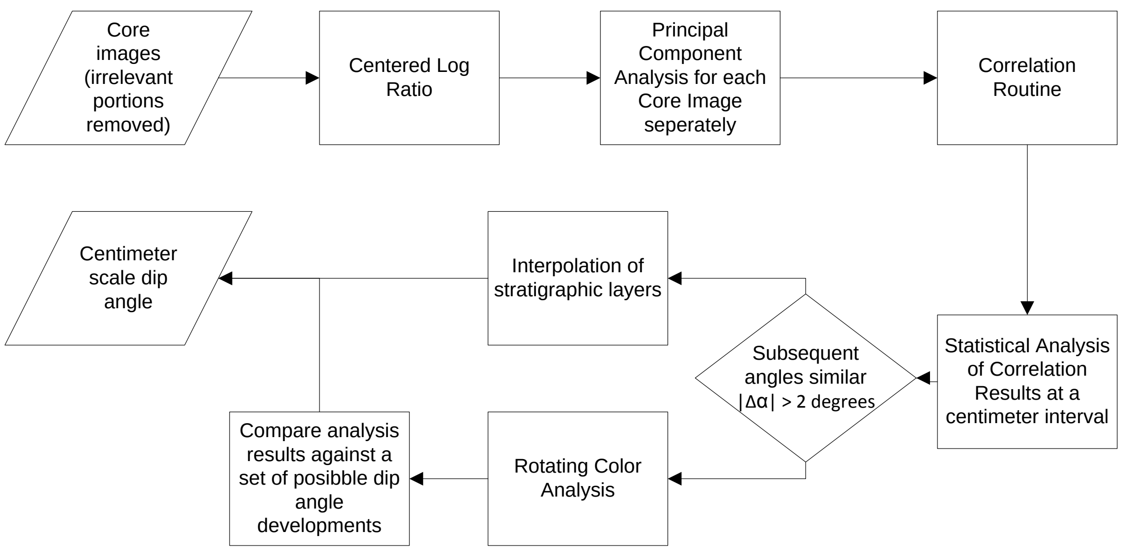

Figure 15: Detailed workflow diagram of process 1.2: Segmenting in centimeter thick layers

6.1.4. Obtaining Properties from Segments

For each centimeter thick segment, properties have to be extracted that make it possible to estimate the permeability and classify segments into lithology and grain size. It has been chosen to extract color and a measure of the texture.

To extract the color, it is first needed to extract a fourth 'color' from the color data, namely: darkness. The darkness is the opposite of intensity of an image and is extracted from the RGB data. This darkness is extracted, because it shows a good separation between some of the facies. Especially mudstone and coal are very dark compared to the other facies.

Next a Centered Log Ratio (CLR) transformation is applied to the core images. This CLR transformation is followed by standardization of the data (i.e. set mean to zero and standard deviation to 1) and subsequently applying a Principal Component Analysis (PCA) on the full set of images, to extract the most informative signal of the color data with low signal to noise. Because the full set of images is too large to perform a PCA analysis, a representative subset is chosen. This subset is an image composed of a small section of each core image. This composed image undergoes a PCA and the coefficients obtained from this analysis are applied to the full set of core images. Next an average value for the first two principal components of (CLR transformed) color is extracted for each centimeter segment.

Secondly the texture needs to be extracted, which is a proxy for grain size. It has been chosen to extract the texture instead of identifying individual grains, because the resolution of the images is not adequate to perform this for the fine grained facies. The texture is extracted by an Auto-Covariance function. For each centimeter thick segment three lines parallel to the previously obtained bedding direction undergo an Auto-Covariance analysis. The analysis is performed on the first principal component of the CLR transformed color data. Three characteristics of the Auto-Covariance are extracted for each of the three lines and the results are (median-weighted) averaged. The three characteristics are the variance, the Zero-Crossing and the 1/3 variance-crossing (see Figure 16). Each of these three characteristics is standardized for the full core (setting the standard deviation to 1 and mean to 0).

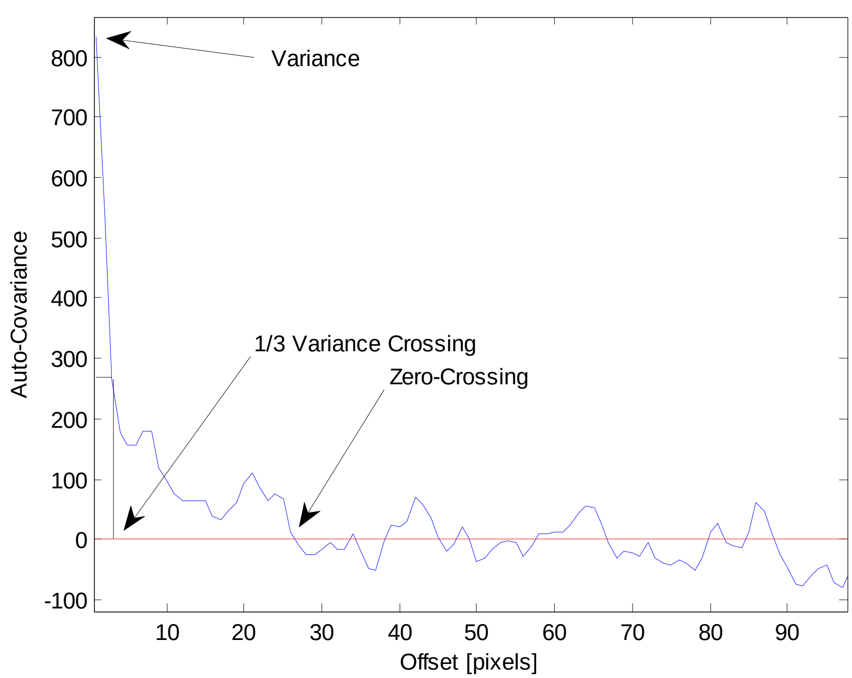

Figure 16; Typical Auto-Covariance function, the three characteristics that are extracted from this function are the variance, Zero-Crossing and the offset of the function at 1/3-variance.

6.2. Method A

Interpretation method A will try to estimate the permeability and porosity based on conventional methods. Method A will first try to distinguish between different facies (defined by grain size and lithology), after this it will assign an average permeability obtained from plug analysis to each interpreted facies.

6.2.1. Classification of facies

Each centimeter thick segment extracted previously has been assigned with a set of properties obtained with the image analysis routine (average color and texture). Next the grain size and lithology need to be extracted; this will be performed in one step by classifying the core into facies.

Classification of facies will be performed on a subset of the extracted properties. This subset will be chosen based on the descriptive ability of each property in terms of facies. This subset of properties subsequently undergoes a Principal Component Analysis (PCA), to obtain the first two principal components of the properties. PCA will enhance the signal to noise ratio of the data, thus making the classification of the data more reliable. Next a model is proposed to classify the data; the model that is chosen is a multivariate Gaussian classification model. This model assumes that each facies can be expressed by a mean and standard deviation of the properties obtained by image analysis and that the properties within a facies are normally distributed around the mean.

The model is calibrated with the geologist's interpretation of the full core. First an initial multivariate Gaussian classification model is fitted on the first two principal components of the chosen set of properties for each facies and each data point is classified based on this initial model leading to an initial classification of facies. To obtain a more independent model, a multivariate Gaussian model is fitted on the results of the initial classification of facies. This 'secondary' multivariate Gaussian model is the basis of method A; the final classification of facies is based on this model.

6.2.2. Assigning permeability to each facies

Each centimeter thick segment has now been assigned a facies and based on this facies a permeability is assigned. Permeability for each facies has been extracted from the plug data by averaging over plugs that consists of the same facies. The obtained average permeabilities are displayed in Table 5.

Table 5: Average Permeability per facies, obtained from plug data.

Facies	Average Permeability K_{avg} [mD]	Facies	Average Permeability K_{avg} [mD]
Sandstone S1l	0.036	Sandstone S4l	34.16
Sandstone S1u	0.021	Sandstone S4u	32.12
Sandstone S2l	0.20	Sandstone S5l	114.7
Sandstone S2u	1.54	Mudstone	0.05
Sandstone S3l	3.44	Siltstone	0.025
Sandstone S3u	41.41	Coal	*

* No plug data was available for coal.

6.3. Method B

Interpretation method B has a more hierarchical structure and does not directly classify each facies. Instead this method will first try to distinguish between sandstone and other lithologies and subsequently tries to estimate the permeability and grain size of the segments classified as sandstone. The other lithologies (mudstone, siltstone and coal) are classified separately and are assigned an average grain size and permeability based on their lithology.

6.3.1. Classifying between sandstone and other lithologies

The classification between sandstone and other lithologies will be performed on the average RGBD color data for each centimeter thick segment. Extraction of the lithology is solely based on the RGBD color data, because the largest separation between the sandstone and the other lithologies should manifest itself in the color data. Coal, mudstone and siltstone are assumed to be darker throughout the core. For mudstone and coal this assumption is relatively straightforward, though the difference in color between siltstone and very fine sandstone can be very small. Nevertheless a difference in color should be present.

The main confusion in terms of color would thus be between siltstone and very fine sandstone. Because the Auto-Covariance properties are relatively similar between the siltstone and very fine sandstone, it was not chosen to use the Auto-Covariance properties to classify the lithology.

Two different models are proposed to separate between the sandstone and other lithologies; the input for these models are the first two principal components of the average RGBD color data per centimeter thick segment. The first model is a multivariate Gaussian classification and the second model is a quadratic decision boundary. Both models are calibrated with the plug data; i.e. the lithology assigned by the geologist at the plughole position. These two models will be evaluated on accuracy and the model that shows the best results will be chosen.

6.3.2. Classification of siltstone, mudstone and coal

The previous model distinguished between sandstone and other lithologies. These other lithologies consist of siltstone, mudstone and coal. To be able to classify these lithologies, a quadratic decision boundary is used. This quadratic decision boundary will be applied on the first two principal components of the extracted properties (color and texture) that show the largest separation between siltstone, mudstone and coal. This model is calibrated on the (by the geologist) assigned lithology at the plughole locations.

6.3.3. Estimating permeability and grain size

The method to estimate the permeability and grain size is based on the lithology assigned in the previous steps. For mudstone, siltstone and coal an average permeability obtained from the plug data is assigned to the centimeter thick segments. Each of these lithologies consists of only one grain size group, thus this grain size is directly assigned for mudstone, siltstone and coal.

The permeability of sandstone, however, shows a strong relationship with the grain size and another method is used to estimate the permeability for sandstone. The Auto-Covariance function extracts the texture of the images and this texture is dependent on the grain size. This makes the Auto-Covariance properties a proxy for the grain size. A model is proposed that uses a linear fit model between the Auto-Covariance properties and the permeability. This model is calibrated on the Hassler sleeve plug permeability of sandstone plugs. Based on this model both the grain size and permeability is estimated. The grain size is subsequently classified into a grain size group to be able to compare the results to the geologist's interpretation of grain size.

7. Results

In this chapter the results of the research are shown. First the results of the accuracy analysis of the Pressure Decay Profile Permeameter (PDPK) are given, followed by the results of extraction of bedding direction from the core images. Next the intermediate results are shown, which indicate the relationship between the extracted properties and facies/permeability. The intermediate results show a visual representation of the models as well. Next the results of both models proposed in this research are given. The results of the models classification of lithology and grain size is compared to the geologist's interpretation. At the end of this chapter the results of the permeability estimation of both models is compared to the null model.

7.1. Pressure Decay Profile Permeameter accuracy

To assess the accuracy of the PDPK, a set of fabricated plugs with known permeability was analyzed. The results of this analysis can be seen in Figure 17. This plot shows a small underestimation (±26 %) of the PDPK across the permeability range compared to the indicated permeability of the fabricated plugs, besides the indicated permeability no other data was available for these fabricated (plastic) plugs.

Another analysis with the PDPK has been performed on plugs taken from the core itself. 38 plugs were selected that cover a representative permeability range of the full core. The permeability measured with the PDPK is compared to the Hassler Sleeve Plug Permeability (see Figure 18). From the plot it becomes clear that the difference in permeability between the PDPK and the Hassler Sleeve becomes smaller at a permeability value larger than 1 mD. No clear bias between the Hassler Sleeve plug permeability and the permeability measured with the PDPK is present in the data.

22 of the 38 plugs measured with the PDPK were taken from relatively homogeneous intervals in the core. For these 22 plugs the permeability of the slab was measured next to the plug hole; these slab measurements were compared to the Hassler sleeve plug permeability (Figure 19). This plot shows that the PDPK tends to overestimate the permeability for half of the measurements, the other half of the measurements are similar to the Hassler sleeve plug permeability.

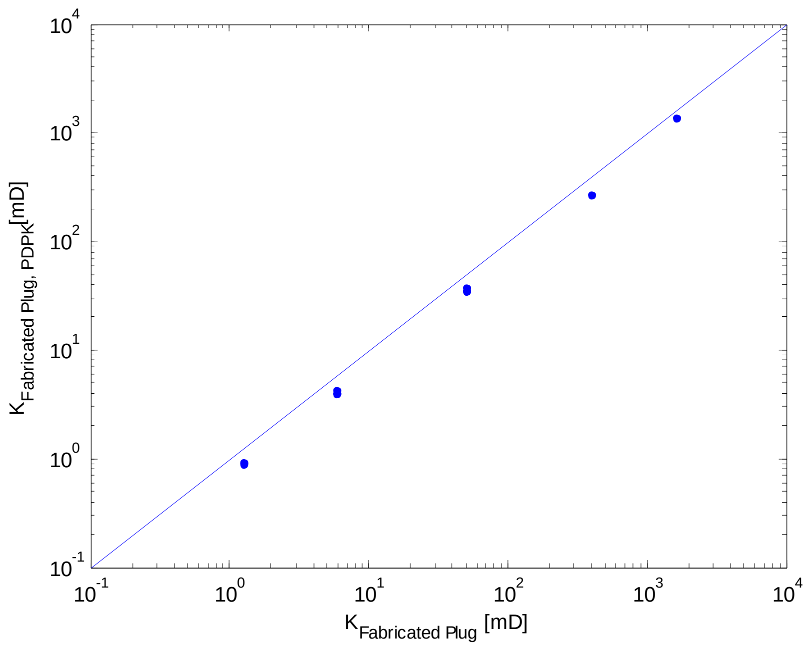

Figure 17: Permeability measured with the PDPK of 5 fabricated plugs compared to the indicated permeability of these fabricated plugs. Three measurements were performed per plug.

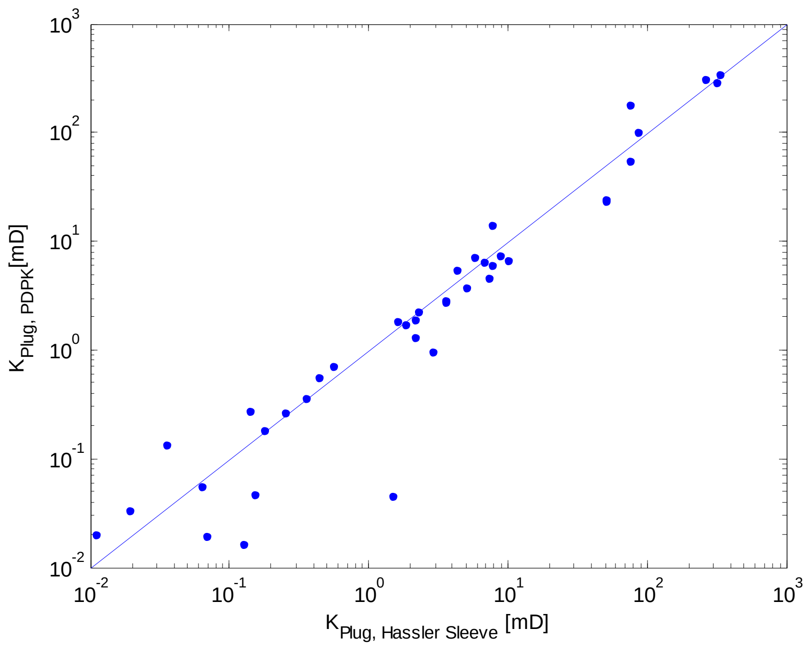

Figure 18: Permeability measured with the PDPK on 38 plugs from core E10-3 compared to the Hassler sleeve plug permeability.

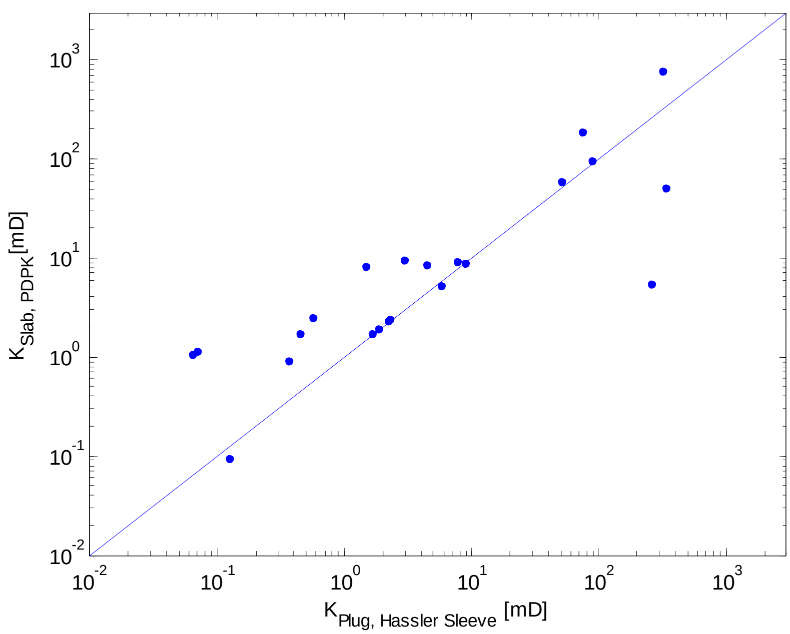

Figure 19: Permeability measured with the PDPK on the core slabs compared to the Hassler sleeve plug permeability. Slab measurements are performed next to the respective plug holes.

7.2. Extraction of bedding direction

The results of the extraction of bedding direction can be seen in Figure 20 for 4 representative core images, the results for the full core can be found in Appendix B. Besides the bedding direction, the method of extraction is indicated in Figure 20. In this figure green lines indicate reliable bedding direction obtained from the correlation routine. Black and red lines indicate an interpolation of the bedding direction and blue lines indicate the bedding direction obtained from the scenario fitting tool.

From the top images it becomes obvious that the direct interpolation method is not always accurate, the layer at 2000 pixels is not extracted by the correlation routine because it does not extend over the full thickness of the core. The brown layer at 5500 pixels is not extracted either, due to its irregular shape. The second image shows a core slab where the layers are more obvious and extraction of these layers is fairly accurate. The third core image shows that the bedding direction is extracted from the fractures in the core. The bottom core image shows a discontinuity that is extracted by the (scenario fitting) routine relatively accurate.

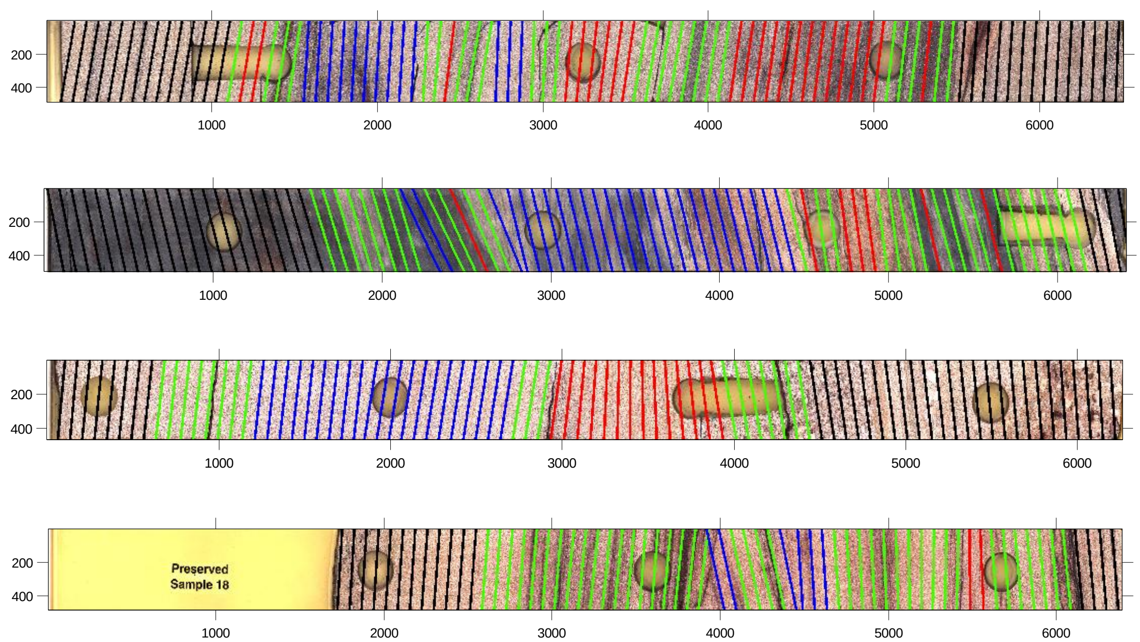

Figure 20: The extracted bedding direction, the axes represent pixels; Green lines are directly extracted from the correlation results, red lines are an interpolation between the green lines, black lines are an interpolation between different core images and blue lines indicate that the scenario fitting routine was used.

7.3. Intermediate results

During the selection of properties obtained by image analysis, an analysis of the extracted properties was performed in terms of their ability to describe lithology, grain size and permeability. The results of this analysis are given in this section. After this a visualization of intermediate results of method A and method B are shown. All the results in this chapter were used to select appropriate (descriptive) properties and classification methods.

7.3.1. Descriptive ability of the extracted properties

To be able to assess the descriptive ability of the extracted average color per centimeter segment, the first two principal components of the average color are plotted against the geologist's interpretation of facies (see Figure 21). In this figure three vectors are visible; these vectors represent the main direction of variance of the respective properties and are also known as a biplot. The direction of the vector concurs to an increase of the variable they represent (i.e. the Dark component is largest towards the left in Figure 21). From Figure 21 it becomes apparent that Red and Green increase towards the sandstone. Darkness seems to increase towards the siltstone, mudstone and coal. The Blue component of the RGBD color data is nearly perpendicular to the major trend in the data.

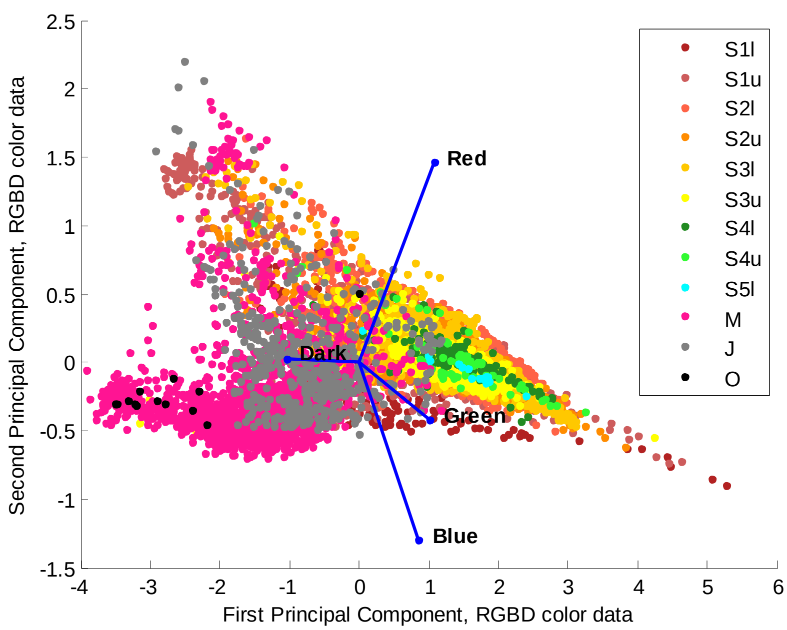

Figure 21; Geologists interpretation of facies projected on the first two principal components of RGBD color data.

A similar analysis is performed on the Auto-Covariance properties extracted for each centimeter thick segment. The first two principal components of the Auto-Covariance properties are plotted against the geologist's interpretation of facies (see Figure 22). From this figure it becomes apparent that the 1/3 variance-crossing is perpendicular to the major trend in the data. The variance increases towards the left bottom, which is roughly the trend of increasing grain size. The Zero-Crossing seems to be opposite of the variance; it increases towards the right top in the direction of decreasing grain size. To get a better understanding how the Zero-Crossing and grain size are related, a plot of the median of the Zero-

Crossing per facies combined with a plot of the mean grain size per facies is shown in Figure 23. In this figure Zero-Crossing and grain size seems to be negatively related for fine grain sizes, whereas the relation starts becoming positive for grain sizes larger than 5 pixels (grain size group S3u).

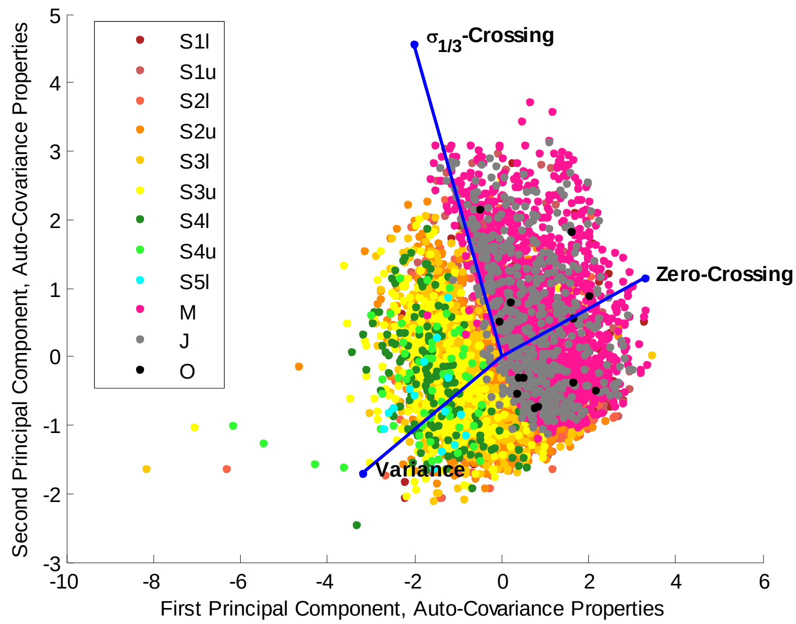

Figure 22: Geologists interpretation of facies projected on the first two principal components of auto-covariance.

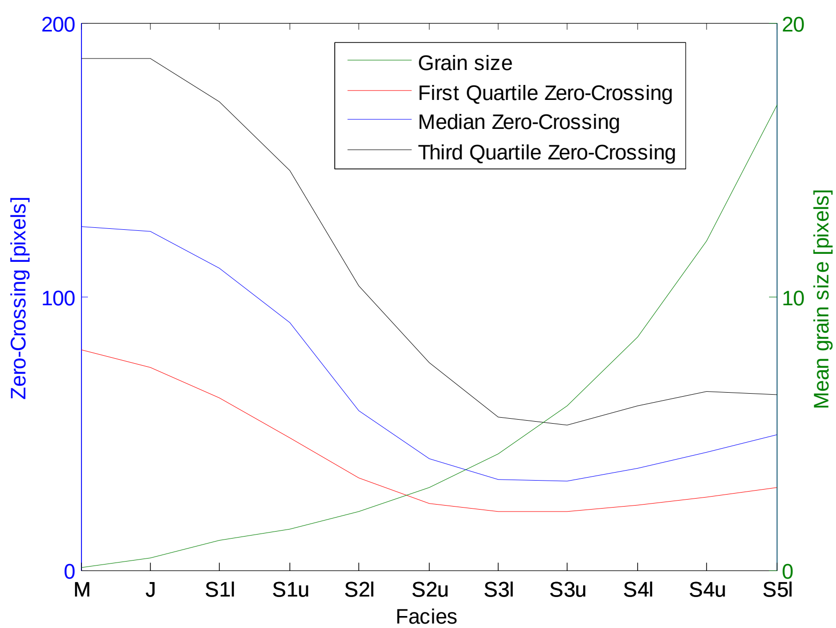

Figure 23: The effectiveness of the Zero-Crossing of the Auto-Covariance function to estimate the grain size. Zero-Crossing is shown on the left y-axis and grain size is shown on the right y-axis.

7.3.2. Method A

For method A it was decided to classify the data based on Zero-Crossing, Variance, Red, Green and Dark. The first two principal components of these properties are plotted against the geologist's interpretation of facies (see Figure 24). From this figure it becomes apparent that the darkness increases towards the siltstone and mudstone, whereas Red, Green and variance increase towards the sandstone. The Zero-Crossing seems to increase towards the finer sandstone.

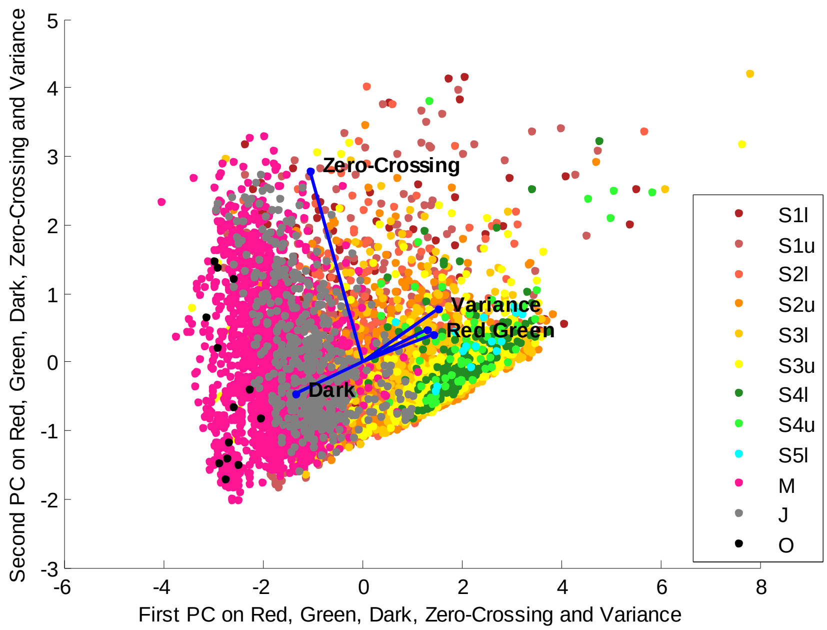

Figure 24: Geologists interpretation of facies projected on the first two principal components of Red, Green, Dark, Zero-Crossing and Variance.

Method A uses a multivariate Gaussian classification calibrated on the geologists interpretation of the full core; the resulting multivariate Gaussian model can be seen in Figure 25. The results of classification with this model are visible in Figure 26. In these two figures it becomes apparent that class S1l covers a large area of the data space and so does class S4u. S5l and Coal are not to be found in these images. Coal was grouped together with mudstone, due to very similar characteristics of both groups in terms of color and texture. Class S5l was overlapped by class S4u and consequently no data points were classified as S5l.

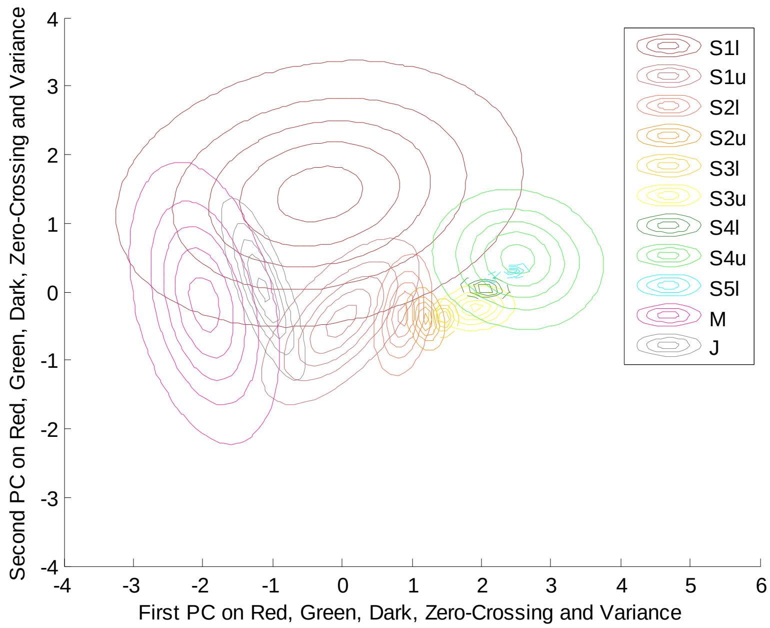

Figure 25; Bivariate Gaussian model used by method A. Iso-density lines are plotted at a probability density of 10 %, 30 %, 50 %, 70 % and 90 %.

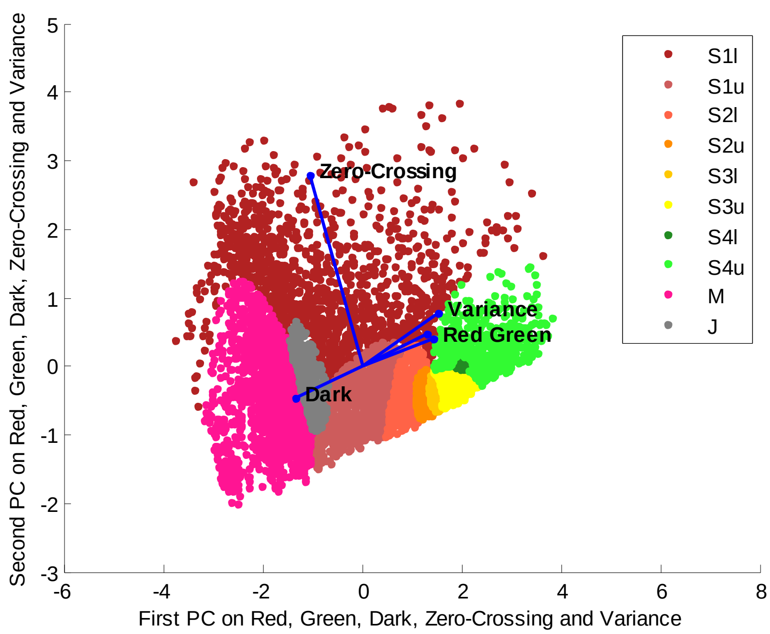

Figure 26: Classification of facies by method A.

7.3.3. Method B

Method B initially classifies between sandstone and other lithologies. Two methods were proposed to perform this classification: a quadratic decision boundary and a multivariate Gaussian classification. Both classification models were calibrated on the facies interpretation of the plugs (Figure 27). The classification of the quadratic decision boundary is shown in Figure 28 and the results can be seen in Figure 29. The multivariate Gaussian classification is shown in Figure 30 and the results are shown in Figure 31. Both models seem to classify sandstone with the same accuracy; however the quadratic decision boundary shows better accuracy in classifying the other lithologies.

The classification of mudstone, siltstone and coal is performed on the first two principal components of Red, Dark, Variance and Zero-Crossing. These first two principal components are plotted against the geologist's interpretation of mudstone, siltstone and coal to be able to assess the separation (Figure 32). From this figure it becomes apparent that coal and mudstone are indistinguishable and that the separation between mudstone and siltstone also shows a large amount of overlap.

The results of classifying mudstone and siltstone by means of a quadratic decision boundary can be seen in Figure 33.

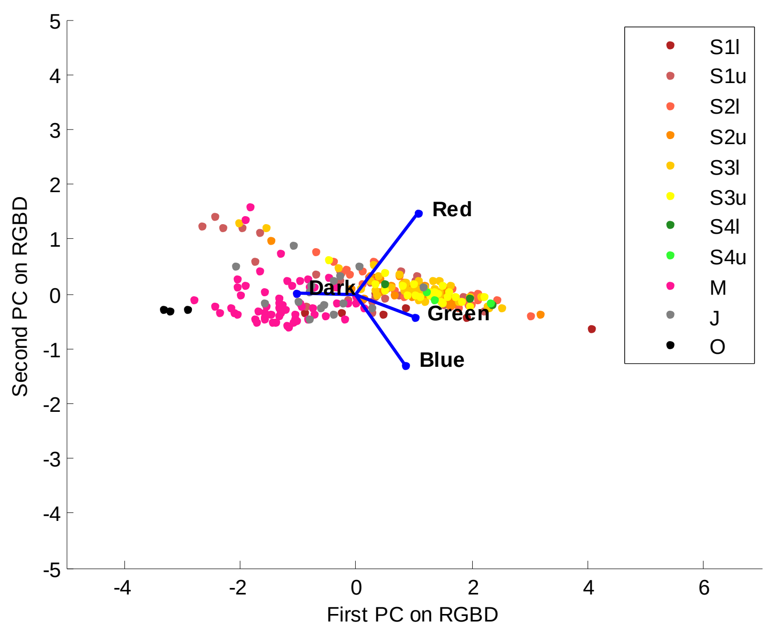

Figure 27: The training set used to calibrate the bivariate Gaussian and decision boundary model of method B.

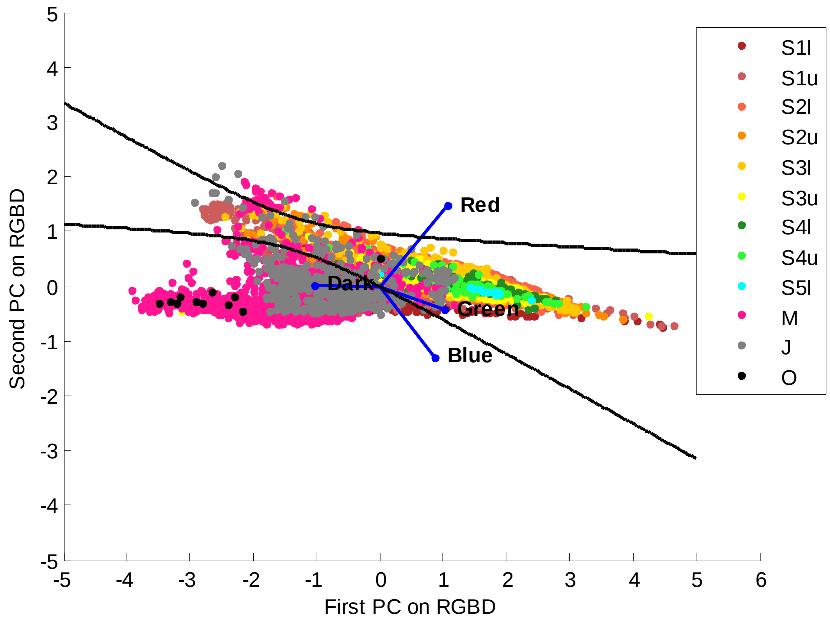

Figure 28: The Quadratic Decision Boundary calibrated on the plug data. This model classifies the data into sandstone and other lithologies. The data points resemble the geologist's interpretation of the core.

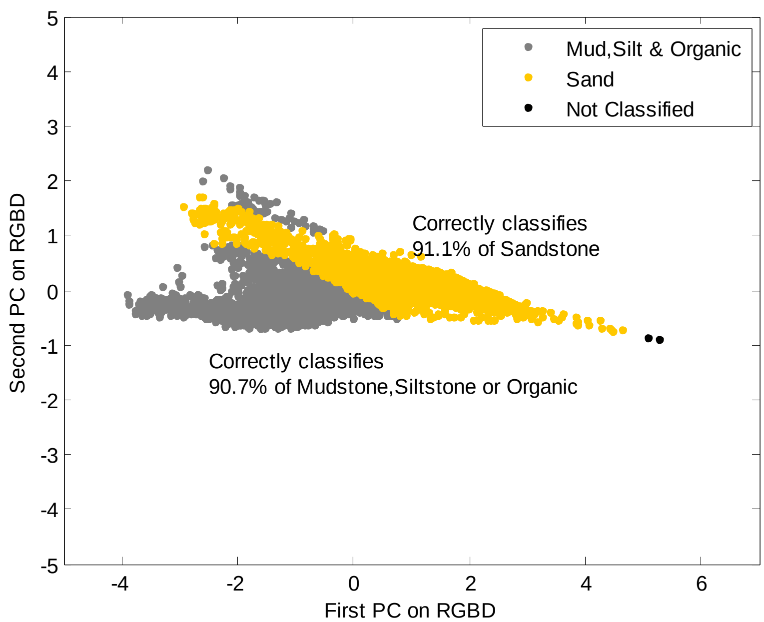

Figure 29: Results of classification with a Quadratic Decision Boundary.

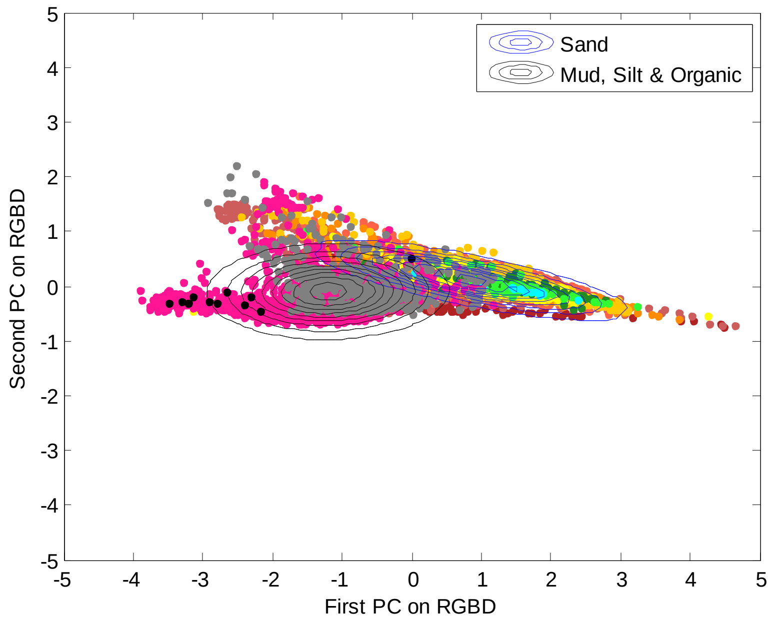

Figure 30: Bivariate Gaussian classification model calibrated on plug data. This model classifies the data into sandstone and other lithologies. Iso-density lines are plotted between 10 % and 90 % in steps of 10%. The data points resemble the geologist's interpretation of the core.

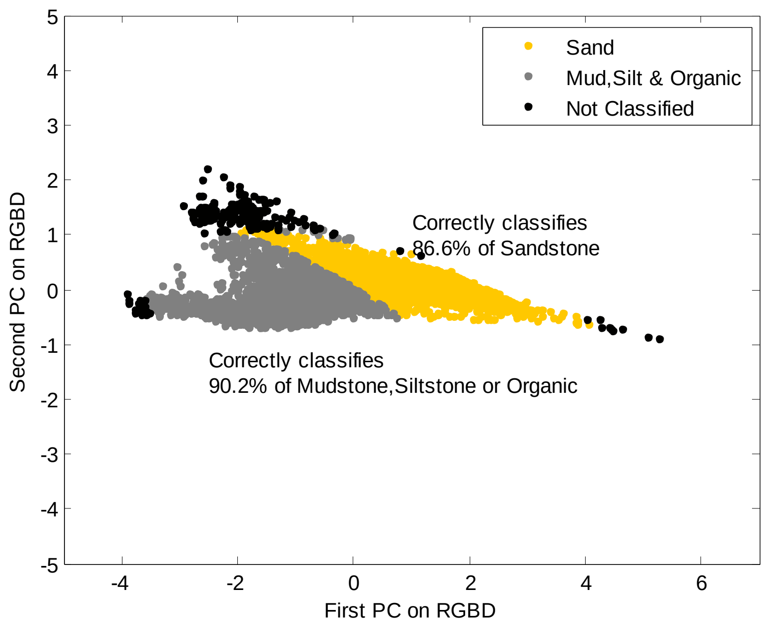

Figure 31: Results of classification based on the bivariate Gaussian model.

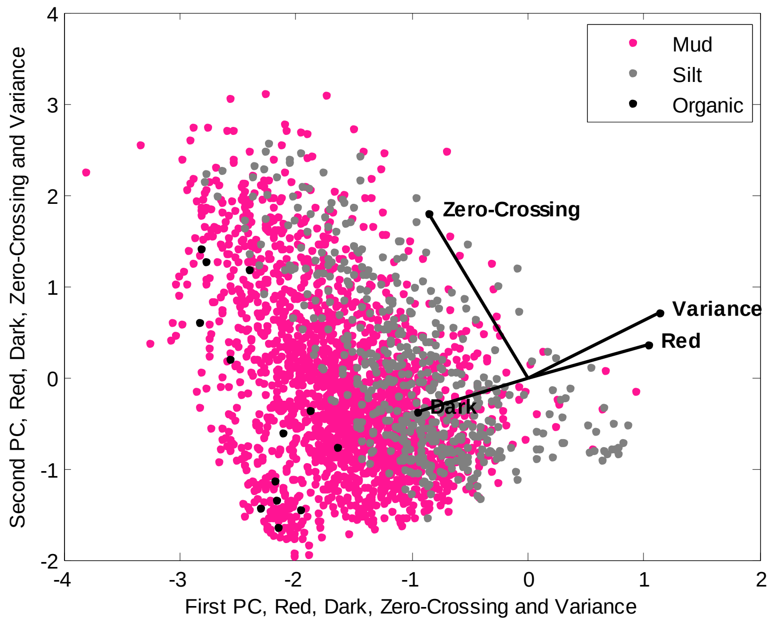

Figure 32: Geologists interpretation of mudstone, siltstone and coal projected on first two principal components of Red, Dark, Zero-Crossing and Variance.

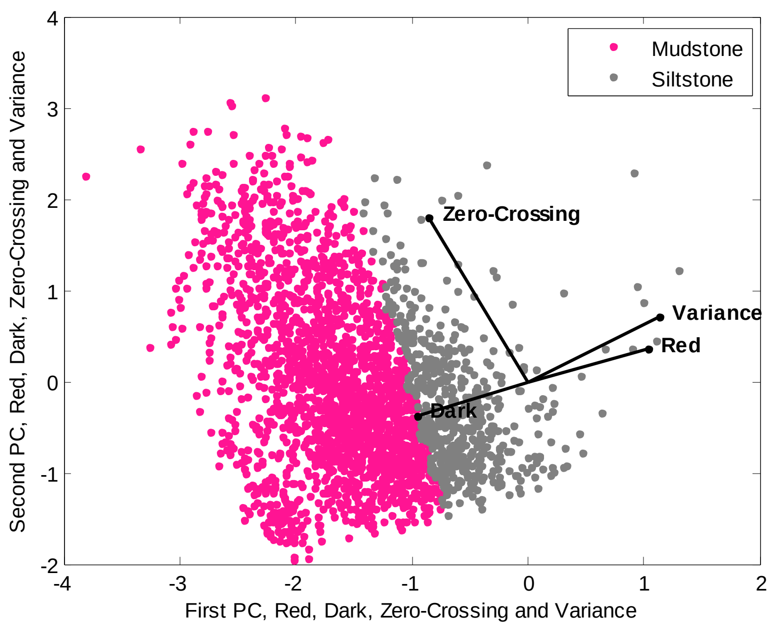

Figure 33; Results of classification between mudstone and siltstone by a linear decision boundary projected on first two principal components of Red, Dark, Zero-Crossing and Variance.

The permeability estimation of method B was based on the Auto-Covariance properties, where the Hassler sleeve plug permeability is used to calibrate a linear fit model. To assess the descriptive ability of the Auto-Covariance properties in terms of permeability, the Hassler sleeve plug permeability is plotted against the first two principal components of the Auto-Covariance properties (Figure 34). To assess the descriptive ability of the Auto-Covariance properties in terms of grain size, the facies interpreted by the geologist are plotted against the first two principal components of the Auto-Covariance properties (Figure 35). The results of the linear fit model in terms of permeability are shown in Figure 36. From Figure 34 and Figure 35 it becomes apparent that the variance shows a relation with the permeability and grain size. A clear trend of increasing permeability/grain size towards the left bottom is visible in both figures.

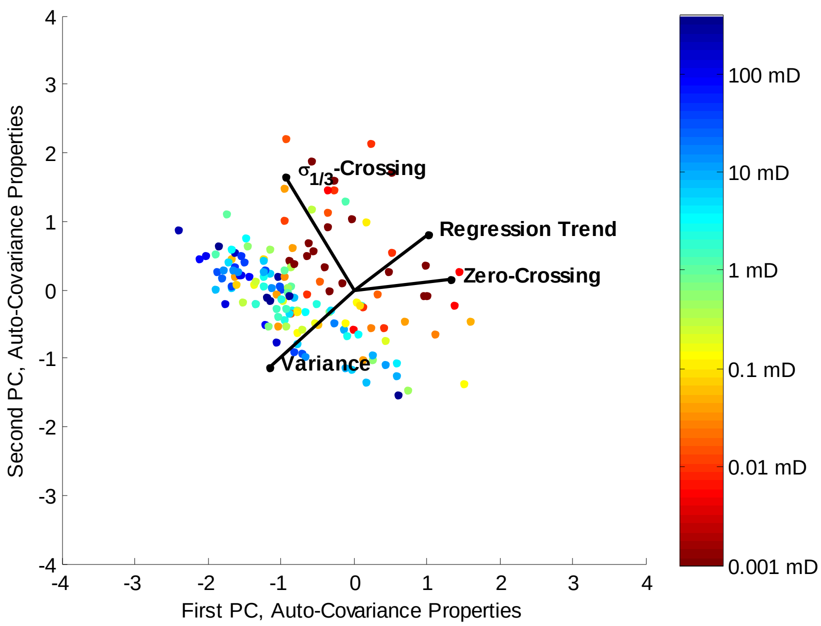

Figure 34: Permeability of plugs, projected on the first two principal components of the Auto-Covariance properties

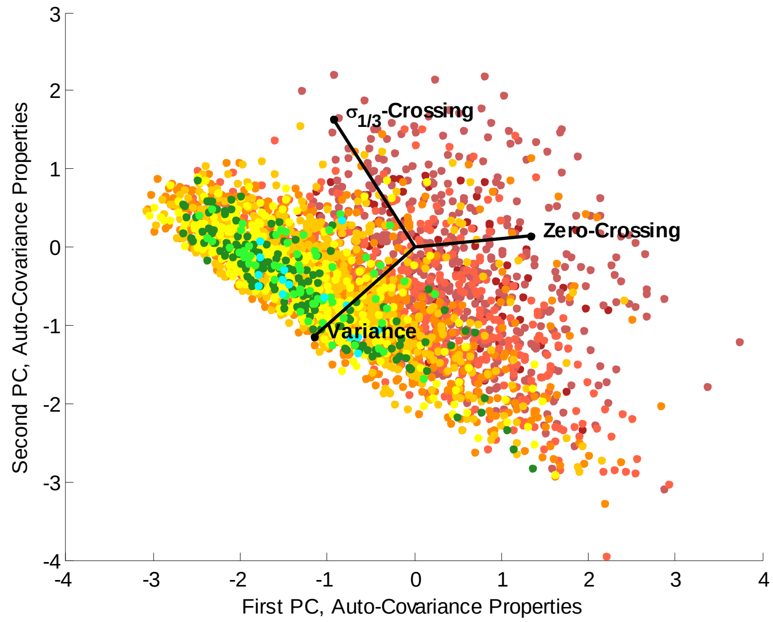

Figure 35; Geologists interpretation of grain size, projected against the first two principal components of the Auto-Covariance properties

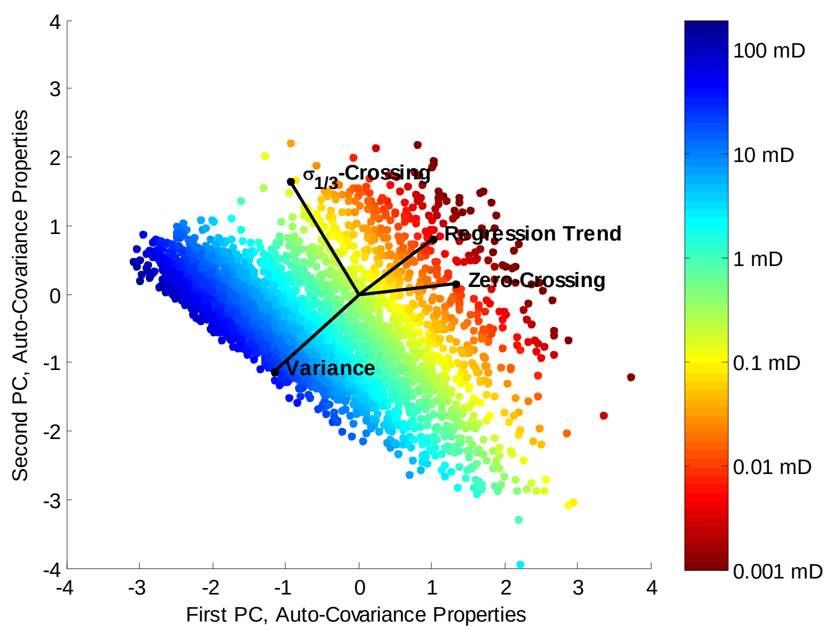

Figure 36; Permeability distribution estimated with a linear regression model that was calibrated on plug data.

7.4. Classification of lithology

The classification of the lithology by the two proposed methods (A and B) is compared to the facies assigned by the geologist. The results of this comparison are visible in Figure 37 and Figure 38 for method A and B respectively. A large part of the very fine sandstone (S1l and S1u) is classified as siltstone or mudstone by method B, whereas method A classifies a larger portion of the very fine sandstone correctly. Method A, however classifies a relatively large portion of siltstone, mudstone and coal as sandstone. Both methods only interpret a small portion of the siltstone correctly, where method A classifies it mainly as sandstone and method B classifies it as mudstone.

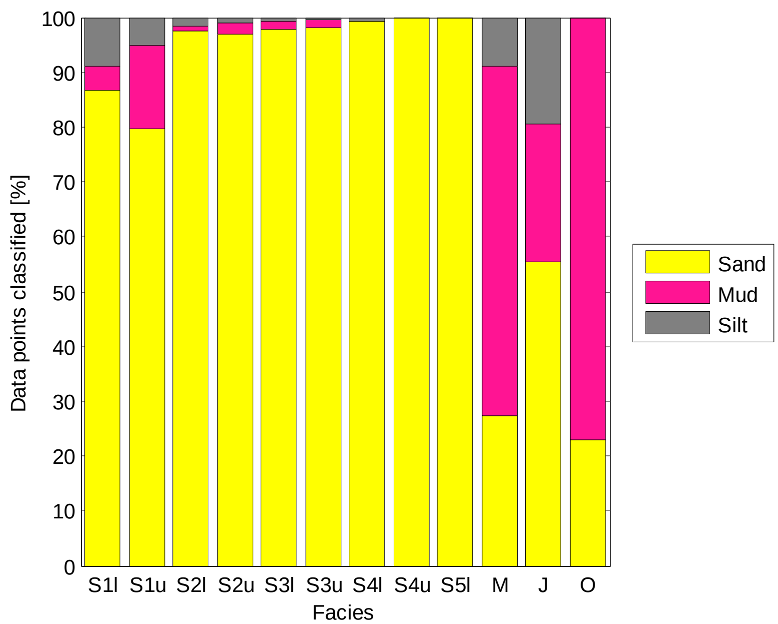

Figure 37: Classification of lithology of method A compared to the geologists classification of facies for the full core. S1l to S5l represent very fine to coarse sandstone. M, J and O represent mudstone, siltstone and coal respectively.

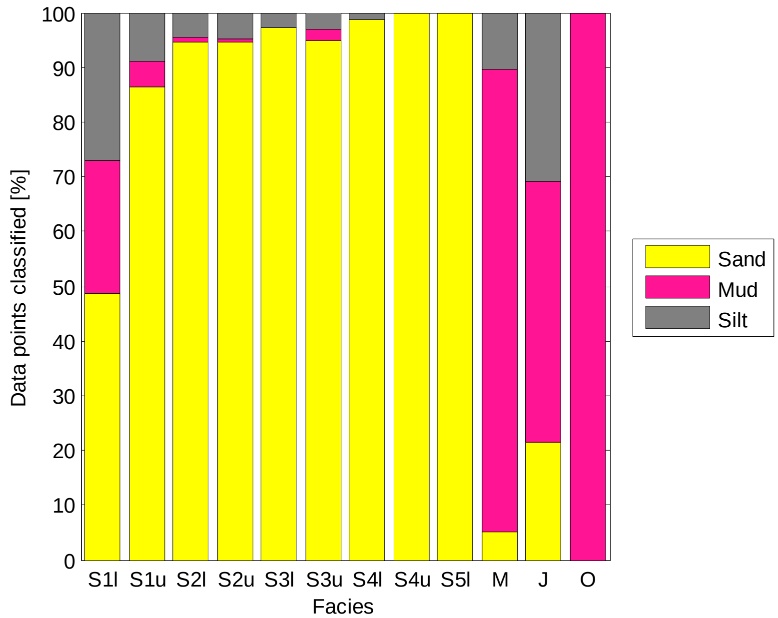

Figure 38: Classification of lithology of method B compared to the geologists classification of facies for the full core. S1l to S5l represent very fine to coarse sandstone. M, J and O represent mudstone, siltstone and coal respectively.

7.5. Classification of grain size

The grain size has been classified by both method A and B based on the grain size classes used by the geologist in the core description. The results of this classification are compared to the geologist's classification and can be found in Figure 39 and Figure 40 for method A and B respectively. A ranked sum test was performed on the different grain size classes in terms of permeability, to find grain size classes that have similar permeability characteristics. A misclassification in a grain size class with similar permeability characteristics is seen as less severe; for example misclassification of very fine sandstone as fine sandstone is considered a better result than misclassification of medium sandstone as siltstone.

The results of this ranked sum test can be found in Table 6. From this table it becomes apparent that facies that have a low number of data points (especially the coarsest sandstone class S5l) are not significantly different from other grain size classes in terms of permeability.

The misclassification of grain size by method A and B are evaluated in terms of similar permeability (obtained from the ranked sum test) against the geologist's classification of grain size. The results can be seen in Figure 41 and Figure 42 for method A and B respectively and are shown quantitative in Table 7 and Table 8. From these figures and tables it becomes apparent that the most misclassification occurs in the fine to medium sized sandstone.

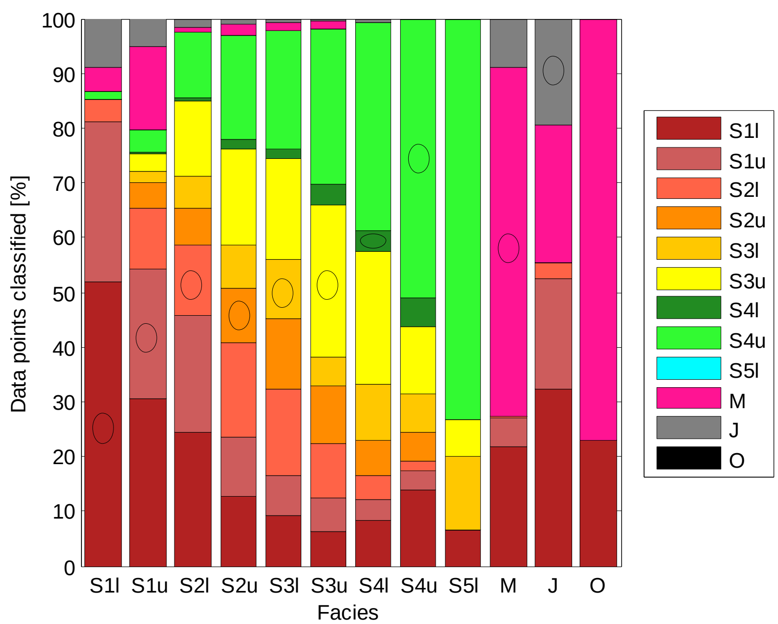

Figure 39: Classification of grain size of method A compared to the geologists classification of facies for the full core. The correct classification of grain size is indicated with a circle.

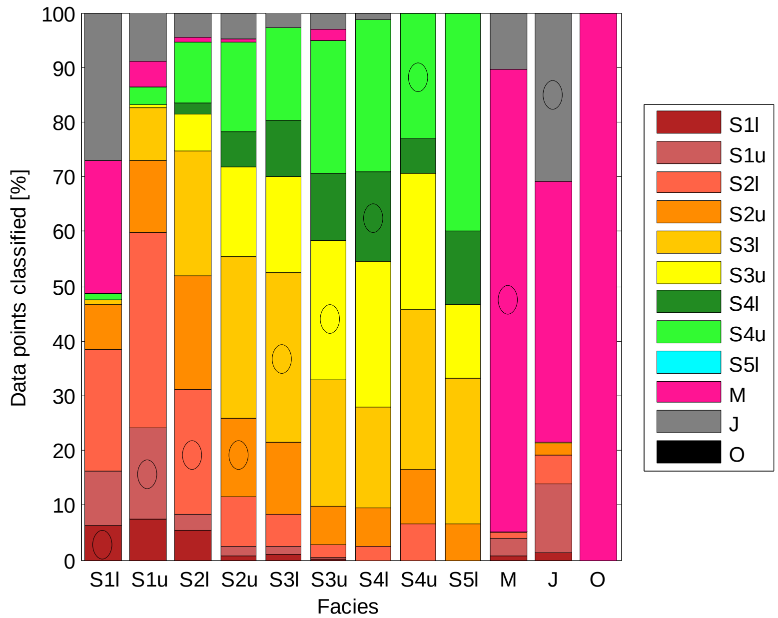

Figure 40: Classification of grain size of method B compared to the geologists classification of facies for the full core. The correct classification of grain size is indicated with a circle.

Table 6: Ranked Sum Test Results obtained by comparing the permeability distribution of grain size classes. Classes S1l to S5l represent fine to coarse sandstone, M represent mudstone and J represents siltstone. A P-value that is higher than 0.05 (bold faced) indicate that there is no significant difference between the permeability distributions.

	Nr. of data points	**S1l**	**S1u**	**S2l**	**S2u**	**S3l**	**S3u**	**S4l**	**S4u**	**S5l**	**M**	**J**
S1l	7	**1**	**0.27**	0.03	<0.01	<0.01	<0.01	0.02	**0.06**	**0.25**	**0.19**	**0.27**
S1u	12		**1**	<0.01	0	0	0	0.01	0.025	**0.17**	0.02	**0.17**
S2l	27			**1**	<0.01	<0.01	0	0.01	0.04	**0.11**	**0.36**	**0.50**
S2u	34				**1**	**0.48**	0	**0.06**	**0.16**	**0.12**	0	0.01
S3l	36					**1**	<0.01	**0.11**	**0.34**	**0.15**	0	<0.01
S3u	23						**1**	**0.65**	**0.50**	**0.71**	0	<0.01
S4l	3							**1**	**0.80**	**1**	0.01	0.04
S4u	2								**1**	**0.67**	0.02	**0.10**
S5l	1									**1**	**0.10**	**0.33**
M	30										**1**	**0.76**
J	6											**1**

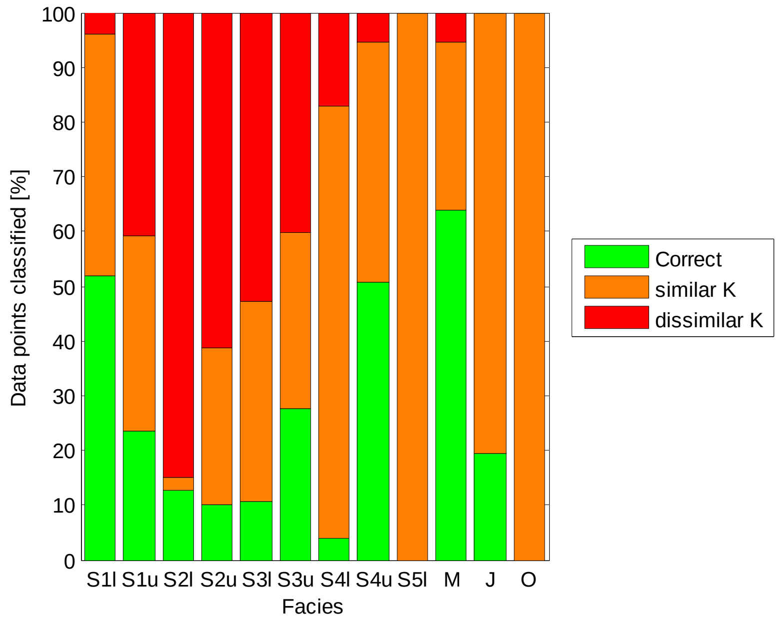

Figure 41: Classification of grain size of method A compared to the geologists classification of grain size for the full core. A misclassification into a class with similar or dissimilar permeability characteristics (obtained from a ranked sum test) is indicated in this figure. No permeability data was present for coal, though an estimation of <1mD was assumed to be similar.

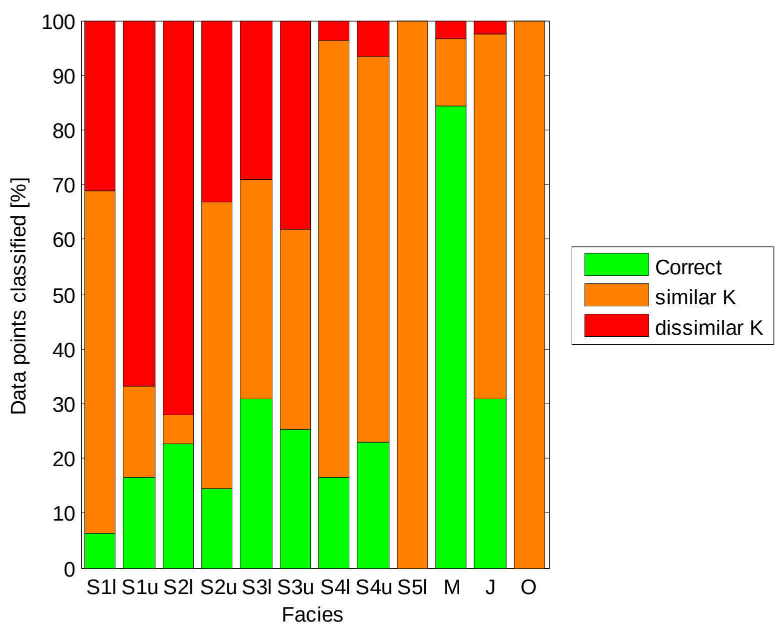

Figure 42; Classification of grain size of method B compared to the geologists classification of facies for the full core. A misclassification into a class with similar or dissimilar permeability characteristics (obtained from a ranked sum test) is indicated in this figure. No permeability data was present for coal, though an estimation of <1mD was assumed to be similar.

Table 7: Classification of grain size of method A compared to the geologists classification of grain size for the full core. A misclassification into a class with similar or dissimilar permeability characteristics (obtained from a ranked sum test) is indicated.

Facies Abbreviated	Facies	Number of data points	Correctly classified [%]	Misclassification with similar permeability [%]	Correct + similar permeability [%]	Misclassification with dissimilar permeability [%]
S1l	Very fine lower sandstone	208	52	44	**96**	4
S1u	Very fine upper sandstone	678	24	36	**59**	41
S2l	Fine lower sandstone	674	13	3	**15**	85
S2u	Fine upper sandstone	893	10	29	**39**	61
S3l	Medium lower sandstone	762	11	36	**47**	53
S3u	Medium upper sandstone	455	28	32	**60**	40
S4l	Coarse lower sandstone	158	4	79	**83**	17
S4u	Coarse upper sandstone	61	51	44	**95**	5
S5l	Very coarse lower sandstone	15	0	100	**100**	0
M	Mudstone	1963	64	31	**95**	5
J	Siltstone	491	20	80	**100**	0
O	Organic/Coal	13	0	100*	**100**	0

* No permeability data was present for coal, a permeability estimation of <1mD was assumed similar.

Table 8: Classification of grain size of method B compared to the geologists classification of grain size for the full core. A misclassification into a class with similar or dissimilar permeability characteristics (obtained from a ranked sum test) is indicated.

Facies Abbreviated	Facies	Number of data points	Correctly classified [%]	Misclassification with similar permeability [%]	Correct + similar permeability [%]	Misclassification with dissimilar permeability [%]
S1l	Very fine lower sandstone	208	6	63	**69**	31
S1u	Very fine upper sandstone	678	17	17	**33**	67
S2l	Fine lower sandstone	674	23	5	**28**	72
S2u	Fine upper sandstone	893	14	52	**67**	33
S3l	Medium lower sandstone	762	31	40	**71**	29
S3u	Medium upper sandstone	455	25	37	**62**	38
S4l	Coarse lower sandstone	158	16	80	**96**	4
S4u	Coarse upper sandstone	61	23	70	**93**	7
S5l	Very coarse lower sandstone	15	0	100	**100**	0
M	Mudstone	1963	84	12	**97**	3
J	Siltstone	491	31	67	**98**	2
O	Organic/Coal	13	0	100*	**100**	0

* No permeability data was present for coal, a permeability estimation of <1mD was assumed similar.

7.6. Estimation of permeability

The estimation of permeability of method A, method B and the null model is compared against the Hassler sleeve plug permeability and the permeability obtained with the Pressure Decay Profile Permeability (PDPK).

Figure 43 shows the permeability estimation of the null model (= average of Hassler Sleeve plug permeability) compared to the mean and standard deviation Hassler sleeve plug permeability for each facies. In this figure the standard deviation of permeability per facies is indicated. Figure 44 and Figure 45 show the average Hassler sleeve plug permeability compared to the average and standard deviation of the permeability estimation of method A and B respectively. In these figures the (quadratic) Best Fit model is shown which is used to divide the total error of the permeability estimation into bias and scatter.

A similar permeability analysis has been performed on the PDPK measurements. The average and standard deviation of the PDPK permeability are compared to the null model per facies and shown in Figure 46. In Figure 47 and Figure 48 the average and standard deviation of the estimation by methods A and B are shown respectively.

The root mean squared error (RMSE) has been calculated for each facies; the RMSE between the permeability estimation of the three methods (A, B and null model) and the Hassler sleeve plug permeability can be seen in Figure 49. The RMSE between the methods' estimation and the PDPK measurements is shown in Figure 50.

For each facies the total error, the bias and the scatter of the permeability estimation of method A and B has been compared to the total error of the null model. This has been performed by means of a chi-squared test and results can be seen in Table 9 and Table 10 for the Hassler sleeve plug permeability and the PDPK permeability respectively. For each chi-squared value, a P-value has been calculated; a chi-squared with a P-value above 95% (= significantly larger error compared to the null model) is shown in red and a P-value below 5% (=significantly smaller error compared to the null model) is shown in green.

The permeability estimation of the full core of method A, method B and the null model can be seen in Figure 51. This permeability estimation is shown in more detail (per core box) in Appendix B.

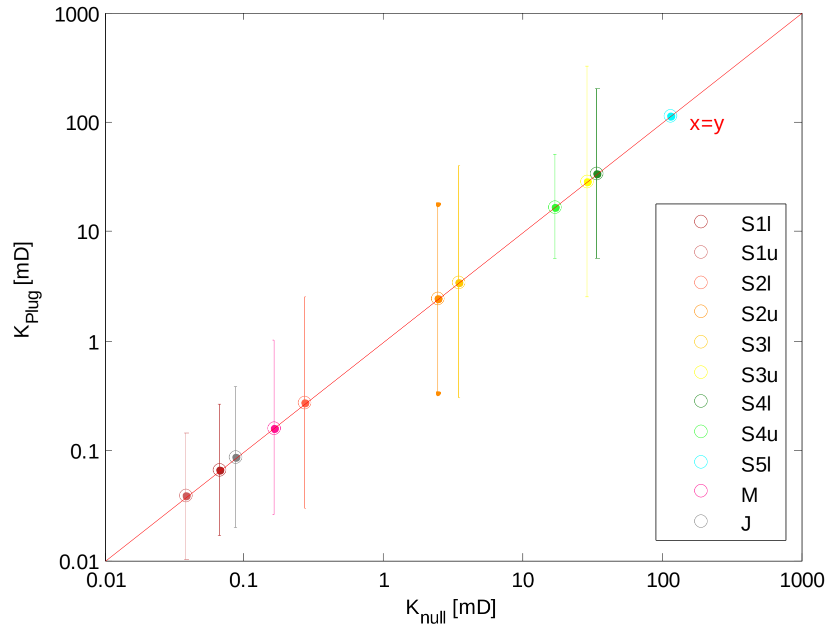

Figure 43: Mean and standard deviation per facies for the Hassler sleeve plug permeability compared to permeability estimation of the null model.

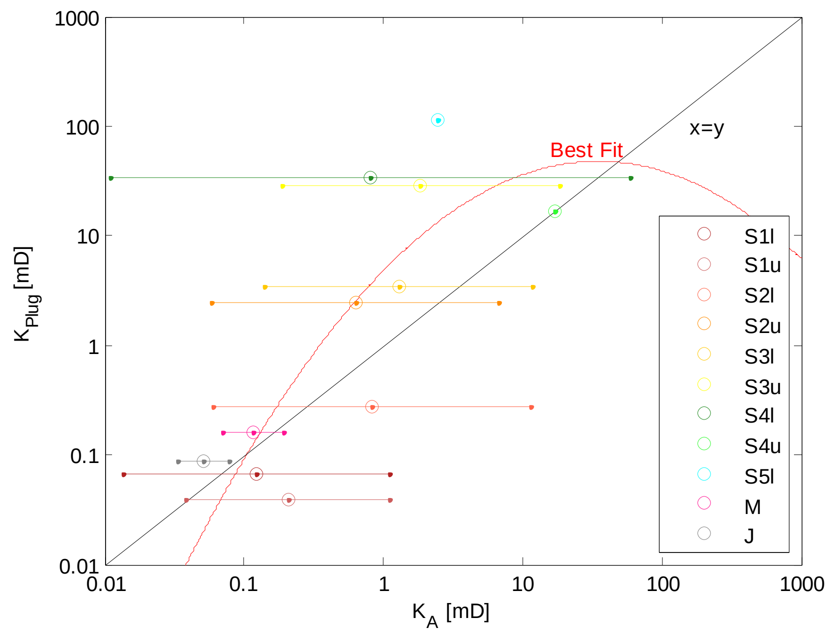

Figure 44: Mean and standard deviation per facies of the permeability estimation of method A compared to the average Hassler sleeve plug permeability. The quadratic best fit line is used to separate the error of the model into bias and scatter.

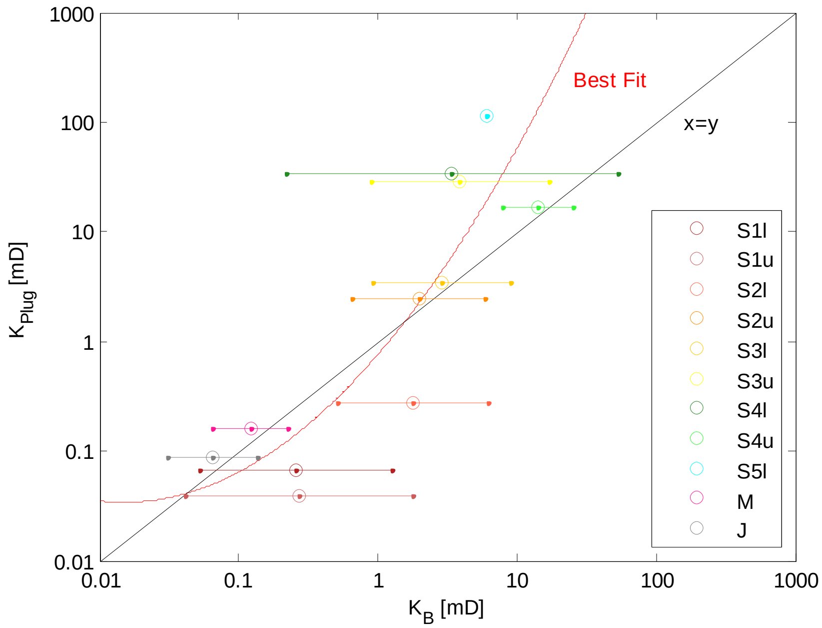

Figure 45: Mean and standard deviation per facies of the permeability estimation of method B compared to the average Hassler sleeve plug permeability. The quadratic best fit line is used to separate the error of the model into bias and scatter.

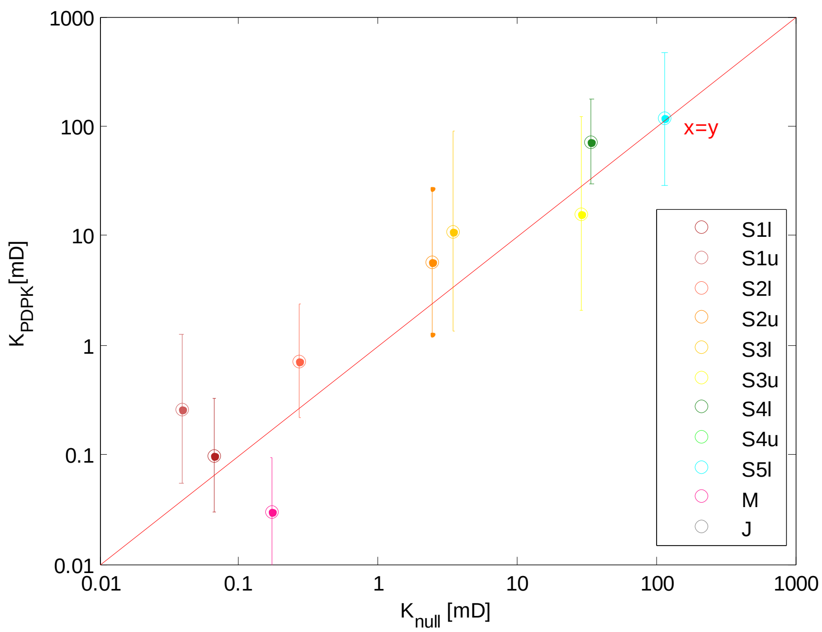

Figure 46: Mean and standard deviation per facies for the Pressure Decay Profile Permeameter measurements compared to permeability estimation of the null model.

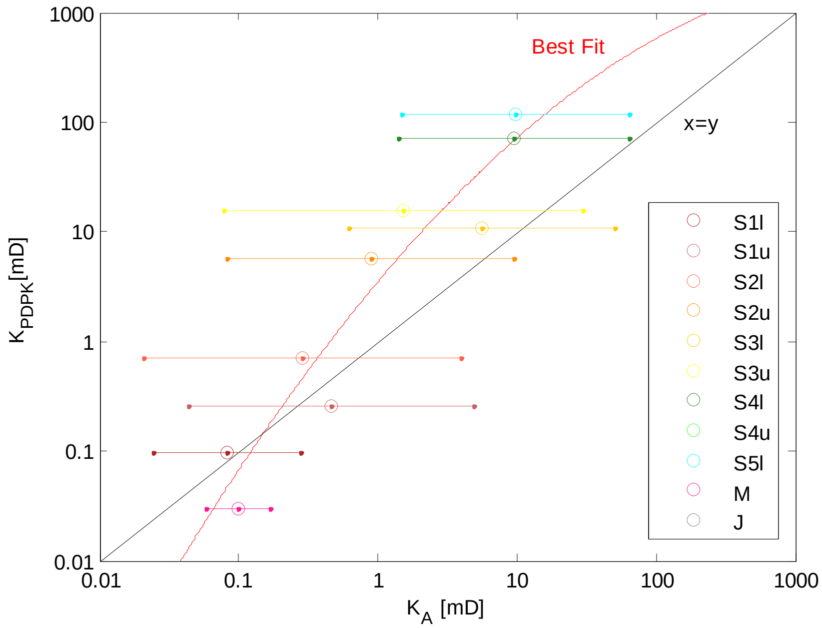

Figure 47: Mean and standard deviation per facies of the permeability estimation of method A compared to the average permeability of the PDPK measurements. The quadratic best fit line is used to separate the error of the model into bias and scatter.

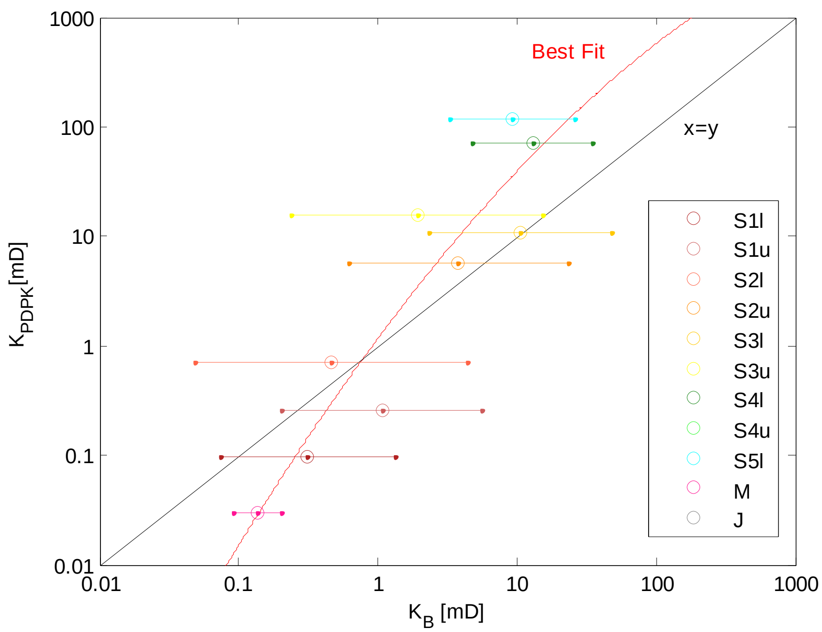

Figure 48: Mean and standard deviation per facies of the permeability estimation of method B compared to the average permeability of the PDPK measurements. The quadratic best fit line is used to separate the error of the model into bias and scatter.

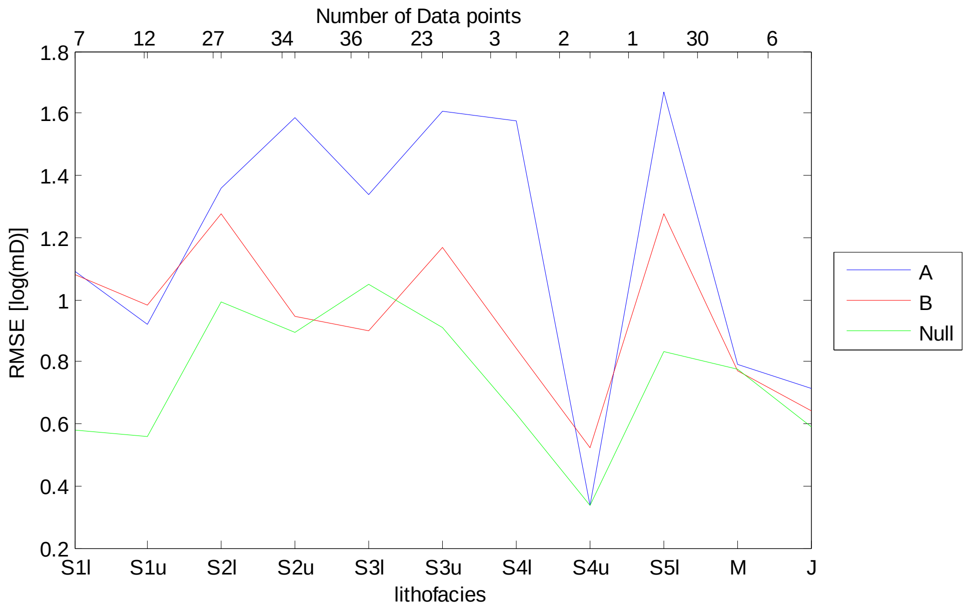

Figure 49: Root Mean Squared Error of the permeability estimatation of method A, method B and the null method compared to the Hassler sleeve plug permeability.

Figure 50: Root mean squared error of the permeability estimates of method A, method B and the null method compared to the measurements performed with the PDPK.

Table 9: Chi-squared variance test results; the error of method A and B to estimate the Hassler sleeve plug permeability is compared to the error of the null model. Red values indicate a significantly larger error of the permeability estimate compared to the null model (P-value of 5%), whereas green values indicate a significantly smaller error of the permeability estimate compared to the null model (P-value of 5%).

	$X^2_{A,total}$	$X^2_{A,scatter}$	$X^2_{A,bias}$	$X^2_{B,total}$	$X^2_{B,scatter}$	$X^2_{B,bias}$
S1l	**23.4**	**15.5**	7.9	**22.9**	9.4	**13.5**
S1u	**29.9**	**20.2**	9.7	**34.1**	**24.1**	10.0
S2l	**38.4**	**34.6**	**3.8**	33.8	**5.8**	28.0
S2u	**77.2**	**42.2**	35.0	27.3	**6.9**	20.4
S3l	39.5	30.5	**9.0**	**17.7**	**5.9**	**11.8**
S3u	**44.2**	25.3	18.8	23.4	**8.2**	15.2
S4l	**4.2**	3.6	0.5	1.2	1.3	-0.1*
S4u	1.0	1.5	-0.5*	2.4	**8.3**	-5.9*
S5l						
M	20.6	**1.5**	19.1	19.6	3.9	15.7
J	7.4	2.8	4.5	6.0	1.4	4.6

* negative X^2 are a result of the error between the estimation and the facies average being smaller than the error between the estimation and the best fit. The P-test was performed on the absolute X^2.

Table 10: Chi-squared variance test results; the error of method A and B to estimate the PDPK permeability is compared to the error of the null model. Red values indicate a significantly larger error of the permeability estimate compared to the null model (P-value of 5%), whereas green values indicate a significantly smaller error of the permeability estimate compared to the null model (P-value of 5%).

	$X^2_{A,total}$	$X^2_{A,scatter}$	$X^2_{A,bias}$	$X^2_{B,total}$	$X^2_{B,scatter}$	$X^2_{B,bias}$
S1l	**66.6**	53.9	**12.7**	135.6	**90.2**	45.4
S1u	181.5	155.2	**26.3**	**154.3**	**71.3**	**83.0**
S2l	**204.2**	**179.0**	**25.3**	**127.5**	**132.1**	**-4.7***
S2u	**384.4**	**283.5**	100.9	**191.6**	**171.3**	**20.3**
S3l	**186.4**	**121.4**	64.9	124.1	**61.7**	**62.4**
S3u	**26.7**	**319**	**-5.2***	15.0	14.5	**0.4**
S4l	**195.2**	**208.0**	**-12.8***	**105.2**	**86.3**	**18.9**
S4u						
S5l	**61.4**	**31.9**	**29.5**	**50.5**	12.6	**37.9**
M	44.1	**5.9**	**38.2**	52.0	**34.7**	**17.4**
J						

* negative X^2 are a result of the error between the estimation and the facies average being smaller than the error between the estimation and the best fit. The P-test was performed on the absolute X^2.

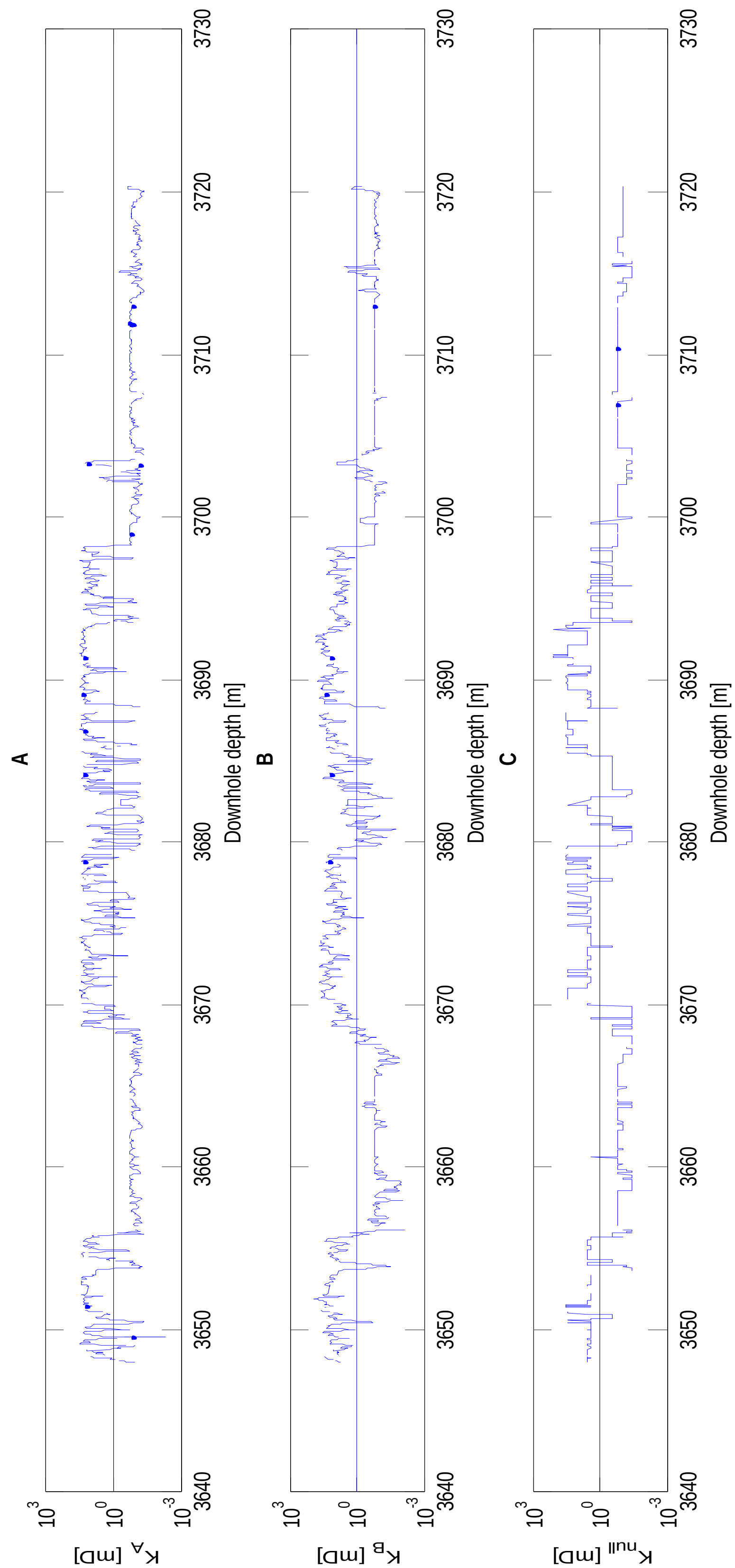

Figure 51: Permeability estimation over the full length of the core

A: permeability estimation of method A.

B: permeability estimation of method B.

C: permeability estimation of the null model

8. Analysis of Results

8.1. Accuracy of the Pressure Decay Profile Permeameter

The accuracy of the Pressure Decay Profile Permeameter (PDPK) has been compared to a set of fabricated plugs with known permeability. Three different measurements were performed on the fabricated plugs and they all showed the same results (error <3%), thus the repeatability of the measurements with the PDPK is high. However the PDPK tends to underestimate the permeability of the fabricated plugs by about 26 %. This could either be caused by a wrong calibration of the PDPK or the permeability of the fabricated plugs is actually different. The fabricated plugs were set into a sleeve and showed signs of compression due to usage, which might cause the actual permeability of the plugs to be different from the indicated one.

The permeability results with the PDPK of 38 plugs from core E10-3 showed a very good fit with the Hassler sleeve plug permeability for a permeability higher than 1 mD. Below 1 mD, the permeability results were more scattered. This could be caused by the accuracy of the Hassler sleeve plug analysis in this low permeability range or it can be caused by a lack of accuracy of the PDPK in the low permeability range. The PDPK did not have any means of calibrating the device below 1.27 mD (the fabricated plug with lowest permeability), except for a leak test (solid plug with a permeability of 0 mD). This lack of calibration could well be the reason for the difference between the PDPK permeability and the Hassler sleeve plug permeability. The possible reasons for the difference in measurements between the PDPK and the Hassler sleeve as seen by the author are as follows:

- The core plugs themselves might have changed during storage
- The estimates of the Hassler Sleeve could retain errors (because emphasize is regularly on high permeability intervals)
- The seal of the PDPK could be leaking
- The PDPK could have measured crack permeability where the cracks do not range over the full length of the plug
- The difference between vertical and horizontal permeability of the plugs can be large. (Hassler sleeve only measures horizontal, whereas the PDPK measures the ‘hemispherical’ permeability)
- The difference in gas permeability with regard to oil permeability might not be estimated correctly by the Klinkenberg correction in the lower permeability region
- The calibration of the PDPK is not correctly performed for low permeabilities

The three reasons that seem most likely for the error in the low permeability range are the wrong calibration of the PDPK, an error in the Hassler sleeve plug permeability and a large difference in horizontal and vertical permeability.

To be able to assess the accuracy of the PDPK on the core slab itself, measurements with the PDPK were performed on the core slab next to the plug holes. These measurements were compared to the Hassler sleeve plug permeability. The plugs that were selected for this analysis were all taken from homogeneous looking sections of the core, to assure that the actual permeability of the core slab and plug were similar.

The results show an overestimate for half of the slab measurements with the PDPK compared to the Hassler sleeve plug permeability. The overestimate is about half an order of magnitude for these measurements. When considering that the permeability estimation of the PDPK is fairly accurate for a permeability higher than 1 mD, the overestimate of the slab measurement is mainly caused by the geometry of the slab compared to the plug, as this is the only difference between the plug and slab measurements.

The main differences between the geometry of the plug and the core slab are:

- The smaller thickness of the core slab
- The flow boundary caused by the settling fluid (epoxy/resin) in the core box
- The small width of the core slab next to the plug holes

The smaller thickness of the core slab together with the flow boundary would induce a lower measured permeability, because the flow boundary is within the area of effect of the PDPK. The settling fluid could have been pushed into the core slab by capillary forces during the settling, which could indicate an even smaller effective thickness of the core slab. This capillary effect is largest in fine grained sediment, as pore throats are smaller and the fluid is pushed further into the slab.

The small width of the core slab next to the plug holes would induce a larger measured permeability, because nitrogen could dissipate through the edges of the sample. As the nitrogen reaches the edges of the sample, the flow resistance caused by the rock sample is gone and the pressure decays faster than it should (considering the permeability) in the sample. The available size of the core slab next to the plug holes is between 1 and 2 cm.

Because an overestimate was measured, the effect of the small width of the core slabs next to the plug holes is the most prominent cause of the difference between the plug and slab permeability measured by the PDPK.

This overestimate is most likely larger near the plug holes, because in this area the nitrogen can dissipate towards the edge of the slab and towards the plug hole. However it is impossible to compare a slab measurement that is further away from a plug hole, because there is no reliable permeability data available for these sections. Thus the over- or underestimate of the slab measurements away from the plug holes remains unknown.

8.2. Estimation of bedding direction

The extracted bedding direction of 4 representative core images out of the total 85 core images were shown in the results. From these core images it became apparent that the direct interpolation does not always result into a correct identification of the bedding direction, due to layers that are not continuous over the thickness of the core or have a more complicated shape. Otherwise the direct interpolation seems to give relatively accurate results. In some cases the bedding direction was extracted from fractures in the core, even though this is not always correct, fractures predominantly occur parallel to bedding. Apart from the extraction of bedding direction from fractures, the extraction of 'reliable' bedding directions with the correlation routine is an accurate representation of the bedding direction.

The scenario fitting routine, used to extract discontinuities shows good results; discontinuities were represented correctly by this routine.

8.3. Intermediate results

8.3.1. The Descriptive ability of the extracted properties

In terms of RGBD color, the separation between mudstone and sandstone showed to be relatively high. This separation expressed itself mainly in the darkness, red and green component of the color data. The mudstone is predominantly darker than the sandstone, which explains the separation in the darkness component of the RGBD color. Sandstone mostly consists of yellow colored sediment. Because yellow is a mixture of red and green, this explains the separation of the red and green component of the RGBD color.

The blue component of the RGBD color does not show a good separation between sandstone and mudstone; the trend of the blue component is nearly parallel to the boundary between sandstone and mudstone, resulting in a poor separation between the two.

The medium to coarse grained sandstone seems to have a similar color as they strongly overlap in the RGBD color space, the very fine to fine grained sandstone is more scattered across the RGBD color space and shows some overlap with the mudstone and siltstone. This indicates that the very fine to fine grained sandstone expresses itself in a large range of colors, where some fine grained sandstone resembles the color of mudstone and other fine grained sandstone resembles the coarser sandstone in terms of color. This can be caused due to the fact that the finer sandstone consists of a mixture of particles from mudstone, siltstone and sandstone.

The siltstone is located near and on the boundary between mudstone and sandstone. The siltstone ranges from color close to mudstone (black/dark) to a similar color of the sandstone (yellow), resulting in a poor separation between siltstone and the other rock types in terms of RGBD color.

In terms of Auto-Covariance properties, the Variance and Zero-Crossing are parallel to the trend in the data. Variance seems to be positively related to the grain size, whereas the Zero-Crossing seems to be negatively related to the grain size. The 1/3 Variance-Crossing is perpendicular to the trend in data and does not seem to give any separation between the data. This 1/3 Variance-Crossing is a measure of the shape of the Auto-Covariance function which could grant information about the shape of the grain size distribution, though it does not seem to be representative of the facies. The negative relation of the Zero-Crossing with grain size was evaluated further and this negative relation seemed to hold for all classes with an average grain size less than 5 pixels (0.35 mm). At larger average grain sizes this relation becomes positive. These results were not as expected, because the Zero-Crossing was assumed to be directly dependent on the grain size. The reason for this is most likely a too low resolution of the images, where at least 5 pixels for the average grain size are needed to be able to obtain a representative value for the Zero-Crossing in terms of grain size. Another reason that can cause this error is the format of the core images, which is JPEG. JPEG discards some of the color information to limit disk space, this information could be the information needed to obtain an Auto-Covariance function that has a stronger relation with the grain size. The characteristics of the very fine to fine sandstone could also be one of the reasons for the misfit between Zero-Crossing and grain size, where the sandstone could have a more homogeneous color in this grain size range.

The positive relation of variance with grain size was expected for mudstone and siltstone, as these facies have a relatively uniform color. However, the relation was not expected to be positive in sandstone as the variance in color was expected to be the same throughout the grain size range of sandstone. The underlying reasons for the low variance in the very fine to fine grained sandstone are the same as discussed above for the Zero-Crossing.

8.3.2. Method A

From the above analysis, the decision was made to discard two properties in the further model, namely: the blue component of the RGBD color and the 1/3 Variance-Crossing of the Auto-Covariance function. These two properties were discarded as they showed poor separation between facies. The resulting multivariate Gaussian classification model on which method A is based showed a very large area covered by the finest sandstone class. This is due to the fact that this finest sandstone class expresses itself in a large set of color and texture, as some of its components consist of mixtures between sandstone, siltstone and mudstone.

8.3.3. Method B

Two different methods were proposed to separate between sandstone and other lithologies. The first was a quadratic decision boundary and the second a multivariate Gaussian classification model. The quadratic decision boundary showed a slightly better accuracy, as it accurately represented the shape of the boundary between sandstone and other lithologies. The overall accuracy of the quadratic decision boundary was about 91 %, compared to about 88 % for the multivariate Gaussian classification model. For this reason the decision was made to use the results of the quadratic decision boundary for further interpretation.

Method B tried to distinguish between siltstone, mudstone and coal next. However the separation between mudstone and coal was very low and for this reason coal was grouped with mudstone. The separation between siltstone and mudstone was performed on the first two principal components of the Red, Dark, Zero-Crossing and Variance. These components showed the best separation between mudstone and siltstone; however a large overlap was still present. A linear decision boundary was fit through the data, as the boundary between mudstone and siltstone was relatively straight.

Next method B proposed a linear fit model on the Auto-Covariance data to estimate the permeability. An assessment was made on the ability of the Auto-Covariance properties to estimate grain size; a trend was visible in the data, however grain sizes larger than S3l seemed to group together (due to the poor relation of Zero-Crossing with grain size). The 1/3 Variance-Crossing is exactly perpendicular to the regression trend of the data, strengthening the previous statement that the 1/3 Variance-Crossing shows at best a very poor relation with the grain size.

8.4. Classification of lithology

Four different lithologies were identified by the geologist; namely sandstone, siltstone, mudstone and coal. Because coal and mudstone were impossible to distinguish based on the available data it was decided to classify the coal as mudstone as well. The reason for this is that coal and (part of the) mudstone are black and do not show a separation in terms of their Auto-Covariance characteristics.

Table 11: Classification of lithologies by method A, compared to the facies identified by the geologist. Classes S1l to S5l indicate very fine to coarse sandstone. M indicates mudstone, J indicates siltstone and O indicates coal.

	S1l	S1u	S2l	S2u	S3l	S3u	S4l	S4u	S5l	M	J	O
Sandstone	87	80	97	97	98	98	99	100	100	27	55	23
Mudstone+Coal	4	15	1	2	1	2	0	0	0	64	25	77
Siltstone	9	5	2	1	1	0	1	0	0	9	20	0

Table 12: Classification of lithologies by method B, compared to the facies identified by the geologist. Classes S1l to S5l indicate very fine to coarse sandstone. M indicates mudstone, J indicates siltstone and O indicates coal.

	S1l	S1u	S2l	S2u	S3l	S3u	S4l	S4u	S5l	M	J	O
Sandstone	49	86	95	95	97	95	99	100	100	5	22	0
Mudstone+Coal	25	5	1	1	0	2	0	0	0	84	48	100
Siltstone	27	9	5	5	3	3	1	0	0	10	31	0

A summary of the results of classification of lithologies for method A and B can be seen in Table 11 and Table 12 respectively. The classification of the medium to coarse grained sandstone is relatively accurate, classification of method A and B show similar results in these areas. Less than 5 % of this sandstone was misclassified, mostly as siltstone. Because siltstone has similar color characteristics to sandstone, this error is understandable especially for method B (which classifies between sandstone and others based solely on RGBD color data). Both methods seem to have more trouble to classify the fine sandstone as sandstone, where method A misclassifies about 13 % of the finest sandstone (S1l) and method B misclassifies about 52 % of the finest class.

The color characteristics of the fine grained sandstone are fairly similar to siltstone and mudstone, which explains the misclassification of method B. Method A seems to interpret the fine grained sandstone more accurately, which indicates that including the texture of the image in the classification of fine sandstone gives better results.

However method A interprets a large section of the mudstone (27%) and siltstone (55%) as sandstone, whereas method B does much better in these areas (5 % and 22 % respectively). Method A interprets 64 % of the mudstone correctly and 20 % of the siltstone, whereas method B interprets 84 % of the mudstone correctly and 31 % of the siltstone. The reason that a large portion of the mudstone is interpreted as siltstone and vice versa is caused by the high similarity of both facies in terms of color and texture. Even though mudstone is on average darker than siltstone, this does not seem to apply to the full core. Thus the separation between mudstone, siltstone and very fine sandstone is not always clear.

8.5. Classification of grain size

The sandstone that has been identified by the methods can be further split up into grain size classes; it was decided to classify the grain size into similar grain size groups as the geologist to aid comparison. Method A directly classifies the grain size based on color and Auto-Covariance properties, whereas method B gives an estimation of the grain size based solely on Auto-Covariance properties and these estimations are subsequently discretized. Both methods show a clear trend in classification, where misclassification occurs mostly in adjacent grain size groups.

A summary of the results of the classification into the correct class or a class with similar permeability characteristics (based on a ranked sum test performed on the plug data) can be found in Table 13 and Table 14 for method A and B respectively. The misclassification into a grain size group with significantly different permeability characteristics will be referred to as a 'severe' misclassification. From these results it becomes clear that both methods classify the siltstone and mudstone into a grain size class with similar permeability characteristics for 95 % of the data points or more. The errors mainly occur in the fine to medium grained sandstone; method A seems to have trouble identifying the sandstone classes ranging from S1u (very fine grained sandstone) to S3u (medium grained sandstone), in this grain size range the average 'severe' misclassification is 47%.

Method B shows similar results; 'severe' misclassification is on average less than method A. Method B also has trouble with the grain size classes ranging from S1l (very fine grained sandstone) to S3u (medium grained sandstone). The average 'severe' misclassification in this grain size range is 45 %.

This misclassification occurs because the Auto-Covariance function does not seem to be representative of the grain size below grain size group S3u. This could be caused by either a too low resolution of the image or the fine grained sandstone has more constant color characteristics compared to the coarser grained sandstone. Siltstone and mudstone do not have a representative Auto-Covariance function in terms of grain size, however they were identified based on their different color.

Table 13: Grain size classification results of method A compared to the facies identified by the geologist; a differentiation between misclassification into a grain size with similar or dissimilar permeability characteristics is made.

	S1l	**S1u**	**S2l**	**S2u**	**S3l**	**S3u**	**S4l**	**S4u**	**S5l**	**M**	**J**	**O**
Correct	52	24	13	10	11	28	4	51	0	64	20	0
Similar K	44	36	3	29	36	32	79	44	100	31	80	100
Dissimilar K	4	41	85	61	53	40	17	5	0	5	0	0
Correct+similar K	*96*	*59*	*15*	*39*	*47*	*60*	*83*	*95*	*100*	*95*	*100*	*100*

Table 14: Grain size classification results of method B compared to the facies identified by the geologist; a differentiation between misclassification into a grain size with similar or dissimilar permeability characteristics is made.

	S1l	**S1u**	**S2l**	**S2u**	**S3l**	**S3u**	**S4l**	**S4u**	**S5l**	**M**	**J**	**O**
Correct	6	17	23	14	31	25	16	23	0	84	31	0
Similar K	63	17	5	52	40	37	80	70	100	12	67	100
Dissimilar K	31	67	72	33	29	38	4	7	0	3	2	0
Correct+similar K	*69*	*33*	*28*	*67*	*71*	*62*	*96*	*93*	*100*	*97*	*98*	*100*

8.6. Estimation of Permeability

For the permeability estimation, a null model was constructed that resembles the facies models presently used in core analysis. This null model assigned the mean permeability of a facies to the whole core. This model was compared to the permeability estimation of both methods proposed in this research.

Table 15: Root Mean Squared Error (RMSE) of method A, method B and the null model compared to the Hassler sleeve plug permeability.

	S1l	S1u	S2l	S2u	S3l	S3u	S4l	S4u	S5l	M	J	avg
$RMSE_{null}$	0.58	0.56	0.99	0.90	1.05	0.91	0.63	0.34	0.83	0.78	0.59	0.74
$RMSE_{A}$	1.09	0.92	1.36	1.59	1.34	1.61	1.58	0.34	1.67	0.79	0.71	1.18
$RMSE_{A}/RMSE_{null}$	1.89	1.65	1.37	1.77	1.28	1.77	2.51	1	2.01	1.01	1.21	1.60
$RMSE_{B}$	1.08	0.98	1.28	0.94	0.90	1.17	0.84	0.52	1.28	0.77	0.64	0.95
$RMSE_{B}/RMSE_{null}$	1.87	1.76	1.29	1.05	0.86	1.28	1.34	1.55	1.54	0.99	1.09	1.28

Table 16: Root Mean Squared Error (RMSE) of method A, method B and the null model compared to the permeability obtained by the PDPK.

	S1l	S1u	S2l	S2u	S3l	S3u	S4l	S4u*	S5l	M	J *	avg
$RMSE_{null}$	0.54	1.07	0.66	0.76	1.04	0.89	0.50		0.57	0.90		0.77
$RMSE_{A}$	0.65	1.17	1.23	1.34	1.55	1.28	1.14		1.59	0.79		1.19
$RMSE_{A}/RMSE_{null}$	1.20	1.09	1.86	1.75	1.50	1.43	2.30		2.77	0.87		1.55
$RMSE_{B}$	0.87	1.06	0.97	0.94	1.26	0.92	0.84		1.44	0.86		1.02
$RMSE_{B}/RMSE_{null}$	1.61	0.99	1.47	1.23	1.22	1.03	1.69		2.5	0.95		1.32

* These facies were not present in the core slabs analyzed by the PDPK

A summary of the root mean squared error of the permeability estimates can be seen in Table 15 and Table 16 compared to the Hassler sleeve plug permeability and the PDPK permeability respectively. From this analysis it becomes apparent that the error is largest for the very coarse sandstone (S5l), the mean reason for this is that only 1 plug was available for this class, making a wrong interpretation in this section devastating to the results and making calibration of permeability more cumbersome. It can be seen that method A makes an average Root Mean Squared Error (RMSE) of 1.2 compared to both the plug and PDPK measurements, which means it makes an average error that is larger than an order of magnitude. This comes down to an average increase in error of 60% compared the null model.

Method B shows an average RMSE of about 1 for both the plug and PDPK measurements, which comes down to an average error of an order of magnitude. Compared to the null model, the error of the permeability estimation of method B is on average about 30 % larger.

The permeability estimation for method B is solely based on the Auto-Covariance function and the assumption that grain size and permeability strongly relate to each other. However the Auto-Covariance function does not accurately represent the grain size as discussed in the previous section, which is the main reason that method B struggles to estimate the permeability.

Method A estimates the permeability in a similar manner as the null model does, however it does not use the geologist's interpretation of the facies directly, but uses a model to interpret the data and classify it accordingly. This means that the RMSE of method A could at best be the same as the null model and any misclassification would induce a larger error in the permeability estimate.

To be able to assess the error compared to the inherent error in the facies (null) model, a chi-squared test has been performed. The chi-squared test tries to estimate the full error of the model, but also tries to divide the error made by method A and B into bias and scatter based on a best fit function. The idea behind this is that the results of method A and B could be calibrated to exclude the bias, but the scatter cannot be extracted. A summary of the results of this chi-squared analysis can be seen in Table 17 and Table 18 compared to the plug permeability and PDPK permeability respectively. From Table 17 it becomes apparent that Method A makes a significantly larger error than the null model for 6 of the 9 sandstone grain size classes. For the 4 finest sandstone classes the scatter of the data is larger than the error in the null model.

Method B shows a significantly larger error compared to the inherent error for the two finest sandstone classes and otherwise does not show a significantly larger error. The scatter of the error is only significantly larger in grain class s1u. Method B shows a significantly smaller error for grain class s3l and the scatter of error of method B is significantly smaller than the inherent scatter in the null model for grain size groups S2l to S3u.

When analyzing Table 18 it becomes apparent that method A shows a significantly larger error compared to the null model for 7 of the 11 grain size classes. The scatter in the data is larger than the error in the null model for 6 of the 11 grain size classes.

Method B shows a significantly larger error of grain classes S1u, S2l, S2u, S4l and S5l. The scatter in the estimation of method B is significantly larger compared to the null model for grain classes S1l, S2l, S2u and S4l. However the scatter in the estimation of method B is significantly smaller than error in the null model for grain classes S1u, S3l and M.

Table 17: Summary of the Chi-Squared variation test results calculated with the Hassler sleeve plug permeability. A plus sign indicates a significantly lower error compared to the null model, a minus sign indicates a significantly larger error compared to the null model.

	$X^2_{A,total}$	$X^2_{A,scatter}$	$X^2_{A,bias}$	$X^2_{B,total}$	$X^2_{B,scatter}$	$X^2_{B,bias}$
S1l	-	-		-		-
S1u	-	-		-	-	
S2l	-	-	+		+	
S2u	-	-			+	
S3l			+	+	+	+
S3u	-				+	
S4l	-					
S4u					-	
S5l						
M		+				
J						

Table 18: Summary of the Chi-Squared variation test results calculated with permeability obtained by the PDPK. A plus sign indicates a significantly lower error compared to the null model, a minus sign indicates a significantly larger error compared to the null model.

	$X^2_{A,total}$	$X^2_{A,scatter}$	$X^2_{A,bias}$	$X^2_{B,total}$	$X^2_{B,scatter}$	$X^2_{B,bias}$
S1l	-		+		-	
S1u			+	-	+	+
S2l	-	-	+	-	-	+
S2u	-	-		-	-	+
S3l	-	-			+	+
S3u	-	-	+			+
S4l	-	-	+	-	-	+
S4u						
S5l	-	-	-	-		-
M		+	+		+	+
J						

9. Discussion

In this chapter the analysis of the results is summarized and compared to existing researches on similar subjects. This chapter emphasizes on the extraction of bedding direction, lithology, grain size and permeability.

9.1. Bedding direction

The initial correlation routine picked up a large portion of the clear boundaries between stratigraphic layers and by means of a statistical analysis discarded the correlation results that were insignificant; this resulted in a map of confident extracted bedding directions irregularly spaced over the full core.

However this routine also interpreted the direction of fractures in the core as bedding direction. In the core used in this research this was not a problem, as nearly all fractures were parallel to the bedding direction, however this could be a problem when this technique is used on other cores which have fractures that do not line up to the bedding direction.

The decision was made to segment the core into centimeter thick layers to aid further analysis; this meant that the confident bedding directions have to be interpolated in areas where no confident bedding direction could be extracted. The direct interpolation between two similar ($|\Delta\alpha| < 2$ degrees) confident bedding directions showed to be accurate for a large portion of the core, however this was not always the case. When a boundary between stratigraphic layers had an irregular shape or did not extend through the whole width of the core, the bedding direction could not be extracted. Direct interpolation in these areas led to an error (in some sections of the core an error of up to 10 degrees was made). These errors were largest when interpolation of the bedding direction between core images was performed, because the correlation routine could not be used to extract bedding directions near or on the edge of the image. Attaching the core images to each other was not an option, as they did not line up correctly.

The scenario fitting between dissimilar ($|\Delta\alpha| > 2$ degrees) confident bedding directions showed good results. On multiple occasions throughout the core this scenario fitting tool extracted a discontinuity correctly and gradual change in the bedding direction was extracted correctly as well.

The main concern of the extraction of the bedding was to obtain centimeter thick segments with relatively homogeneous rock throughout the segment. This was performed correctly for large sections of the core; however the choice of a centimeter interval resulted in stratigraphic boundaries located exactly in the middle of some segments. An irregular segmentation of the core that sets the boundary of the segments at the boundary between stratigraphic layers would be able to get better results in the subsequent classification of other properties. Another limitation is that this technique does not provide a means to differentiate between the bedding direction that is extracted from actual beds or from fractures/discolorations. This means that the routine can pick up a (incorrect) bedding direction due to discolorations caused by factors independent of the bedding direction (for example: local corrosion or diagenesis).

9.2. Classification of lithologies

Both method A and B group coal together with mudstone, because the characteristics of these lithologies are very similar (black and fairly homogeneous color).

The classification of sandstone was performed correctly by both method A and B for the medium to coarse sandstone, with a misclassification of less than 5 %. The classification of fine sandstone, siltstone and mudstone was not as accurate. The black mudstone was classified correctly; however the lighter mudstone present in the core was not always classified correctly as its color resembled that of siltstone. A summary of the results can be seen in Table 19. From this table it becomes apparent that the classification of sandstone is relatively accurate for both methods, though the classification of siltstone and mudstone is more troublesome. Especially method A seems to have trouble identifying the siltstone and mudstone.

Table 19: Summary of the classification results of lithology by method A and B against the interpretation of the geologist.

	Sandstone [%]	**Siltstone [%]**	**Mudstone [%]**	**Coal [%]**
Sandstone, A	95	55	27	23
Siltstone, A	2	20	9	0
Mudstone+ Coal, A	3	25	64	77
Sandstone, B	91	22	5	0
Siltstone, B	5	31	10	0
Mudstone+ Coal, B	4	48	84	100

Method B used color data alone to distinguish sandstone from the other lithologies. Method B showed to have similar problems to separate the fine sandstone from the other lithologies; especially the finest sandstone class, which was interpreted as mudstone (25 %) and siltstone (27%). The classification of mudstone showed a relatively high accuracy (84 % classified correctly), however the siltstone was harder to classify correctly as only 31 % was classified correctly.

Both methods clearly had a lot of trouble to distinguish between the fine grained sediment, as color characteristics were relatively similar. This effect was most visible in the classification of siltstone, because a part of the siltstone resembles the mudstone and another part resembles the very fine sandstone. To be able to distinguish between mudstone and siltstone with a higher reliabilty, other data is needed besides the color and texture of the image (for example: log data).

Method B shows a higher accuracy than method A, even though it uses a smaller set of calibration data (only plug data compared to the full geological map of the core). This raises question marks on the use of a multivariate Gaussian classification model to classify such complex data, as a simple hierarchical model based on decision boundaries shows better results.

The accuracy found by a previous study *(Thomas et al, 2011)* was not reached in this research. This previous study correctly identified 94 % of the lithologies present. This study classified the core images based on average color and standard deviation of the color and tried to distinguish shale, limestone and sandstone. The standard deviation of color used (by Thomas et al.) to describe the texture is similar to the variance used in our research. The reason that this previous study showed a higher accuracy is most likely caused by a much smaller core (8 m compared to 85 m) that makes calibration easier. Further on lithologies showed a better separation in terms of color in this previous work. In this previous research each facies had a fairly constant color, whereas in core E10-3 the color of a single facies had a much larger range (especially the very fine sandstone). Another reason that the lithology was not always classified correctly might be due to mixtures of lithologies in Core E10-3. The core was interpreted by the geologist, which did not assign a mixture to any sections. These mixtures can induce an error in the results, especially when they are used to calibrate the model.

9.3. Classification of grain size

The classification of grain size was performed differently for method A and B. Method A directly classified the grain size based on the facies it assigned with a multivariate Gaussian classification model. Method B uses a hierarchical structure to classify the data into a grain size group.

A similar error occurred for method A as was present in the classification of the lithology, namely a large misclassification between the very fine sandstone, siltstone and mudstone. To be able to say something about the severity of misclassification, the grain size groups were evaluated in terms of permeability, where a misclassification into a grain size group with similar permeability characteristics was seen as less severe. This evaluation showed that the largest 'severe' misclassification occurred in the fine to medium grained sandstone for both method A and B. The reason for this is that the Auto-Covariance function does not show a good fit with the grain size in this grain size range. Another reason for this is that the ranked sum test to evaluate the similarity of different grain size groups is somewhat flawed; grain size groups that are represented by a small amount of data points (plugs) are statistically more similar to other groups, making 'severe' misclassification nearly impossible. This was especially the case for the coarsest sandstone, which was represented by 1 plug.

The reason why the classification of the grain size of mudstone and siltstone shows better results is due to the difference in color of mudstone and siltstone compared to sandstone. Although a large misclassification between mudstone and siltstone occurred, the permeability characteristics of both classes are similar; leading to a less severe error in the model.

A previous study *(Rubin et al, 2004)* tries to estimate grain size based on an auto-correlation function (similar to the Auto-Covariance function used in our research), Rubin states that the minimum resolution of the image should be 1 pixel/grain for the smallest grain present in the image. In our research no value for the smallest grain size is present, however a value for the average grain size is. It is possible that the smallest grain size has a diameter that is 5 times less than the average grain, which could explain the misfit between the Auto-Covariance function and grain sizes under 5 pixels/grain$_{avg}$. The previous work has been performed on loose sediment and not on core slabs, which could also affect the results of the Auto-Covariance function, due to grains being cut in half by the slabbing process and a lower relief present in the rock sample. The grain size estimation of Rubin is also calibrated with measurements on sediment with similar color characteristics, whereas in our research the calibration is performed on sandstone taken from a range of different facies, which could lead to a wrong calibration.

The result that the Auto-Covariance function show in the medium to coarse sandstone, however, are relatively similar to the results obtained by Rubin as the grain size and Zero-Crossing are positively related in these facies.

9.4. Estimation of Permeability

The accuracy analysis of the Pressure Decay Profile Permeameter (PDPK) showed that the PDPK underestimated the permeability of the fabricated plugs relatively constantly with 26 %, this is either caused by an inherent flaw in the PDPK or the indicated permeability of the plugs is incorrect. The PDPK measurements on the plugs of core E10-3 showed a relative good relation with the Hassler sleeve plug permeability for high permeable plugs (K_{plug} > 1mD). For plugs with a low permeability (K_{plug} <1 mD) the relationship became worse, in this permeability range an error in the PDPK measurements and/or in the Hassler sleeve plug permeability occurs. The relationship of the Hassler sleeve plug permeability with PDPK measurements on the core slabs showed that due to the geometry of the core slab, measurement with the PDPK showed an overestimate for half of the measurements across the full permeability range. This is mainly caused by the low width of the core slabs next to the plug holes.

The estimation of permeability of methods A and B has been compared to the null model, which was based on the facies models used presently in the oil industry. Method A is based around a similar model, where the average plug permeability is assigned to a facies. Method B estimates the permeability based on the Auto-Covariance function for sandstone, as the Auto-Covariance function was seen as a proxy for the grain size which is related to the permeability.

For both methods the root mean square error (RMSE) has been calculated per facies and compared to the RMSE of the null model. This error was calculated in the logarithmic space. From this analysis it became apparent that both method A and B struggled to estimate the permeability of the very fine sandstone (S1l and S1u), where the error of estimating the plug permeability was 70 % to 90 % larger than the null model for method A and B respectively.

The permeability estimation of plugs consisting of fine to coarse grained sandstone showed better results. Method A showed an error that was 67 % higher compared to the null model. Method B showed an error that was 27 % higher compared to the null model.

Both methods showed results similar to the null model for siltstone and mudstone. Method A had the same RMSE as the null model for mudstone and a 21 % higher RMSE for the siltstone. Method B showed a similar RMSE for the mudstone and a 9 % higher RMSE for the siltstone. The overall RMSE of the plug permeability estimation of method A is 1.18 and is 60 % larger than the null model. Method B has an overall RMSE of 0.95 and is 28 % larger than the null model. This means that the error made by method B is just below an order of magnitude, which is a reasonable result.

The RMSE of the models compared to the Pressure Decay Profile Permeameter (PDPK) is relatively similar to the plug data, apart from the coarsest grain size. This grain size was not classified correctly and therefore the RMSE is 150 % larger than the null model for both method A and B. The estimation of the permeability compared to the PDPK measurements showed an RMSE of 1.19 for method A, which is 55% larger compared to the null model. For method B this RMSE was 1.02, which is 32 % larger than the null model. The results of method B are promising when considering that the resolution of the core images is not high enough to extract a proper proxy for the grain size with the Auto-Covariance function.

The errors caused by method A and B are separated into bias and scatter by means of a best fit model and are evaluated using a chi-squared test. The results of this test showed that the error in plug permeability estimation of method A was significantly larger than the inherent scatter in permeability data for very fine sandstone to coarse sandstone. The scatter of the error of method A was larger than the inherent scatter of the data for very fine to fine grained sandstone.

The results of the plug permeability estimation of method B showed a significantly larger error compared to the inherent scatter for the very fine sandstone (S1l and S1u) and the scatter of S1u and S4u are significantly larger than the inherent scatter. However, the scatter in grain size classes S2l to S3u show a significantly lower compared to the inherent scatter in the data. This means that method B could estimate these permeabilities more reliable than the null model if the bias of method B would be extracted from the results.

The chi-squared test has also been performed on the comparison between the models and the null model for the PDPK measurements. The results for method A were relatively similar to results from the plug data; errors were made throughout the grain size classes. The scatter of the estimation of method A is significantly larger than the scatter of the null model for all sandstone grain sizes except the very fine sandstone. Method A thus performs worse than the null model in most grain classes and at best shows a similar error to the null model. This was expected as the basis of the null model and method A are similar, where any misclassification of method A could lead to a larger error in permeability estimation.

Method B shows a scatter that is significantly larger compared to the null models scatter for 4 grain size groups, whereas it shows a significantly smaller scatter compared to the null model for 3 of the grain size groups. These results are promising, as this means that method B could perform better in some areas compared to the null model when calibrated.

10. Conclusion & Recommendations

10.1. Conclusion

10.1.1. Bedding direction

The bedding direction is extracted by performing correlations on two lines on the core images that are parallel to depth; correlation is performed on the first principal component of log-transformed RGBD color data. The results of this correlation undergo a statistical analysis. In sections where no reliable bedding direction could be extracted, the bedding direction was either interpolated or a second routine that extracts the direction of least standard deviation in color is used. The result of this is a segmentation of the core in centimeter thick layers parallel to (extracted) bedding direction.

The bedding direction is extracted correctly for a large portion of the core; however the bedding direction is sometimes extracted from fractures, which could induce errors. The direct interpolation of the bedding direction extracted from the statistical analysis showed some flaws, especially in areas where stratigraphic layers had an irregular shape or when interpolating between core images. The extraction of discontinuities by means of the scenario fitting tool showed to be accurate as it traced the discontinuities correctly. The choice of segmenting the core on a centimeter interval induced some minor errors; some of the segments were located on the boundary of facies, resulting in the presence of two facies in a single centimeter thick segment.

10.1.2. Lithology

The core is classified based on the centimeter segments, where each segment is assigned a lithology (sandstone, siltstone or mudstone). Both method A and B were unable to differentiate between mudstone and coal, due to similar characteristics.

Method A uses a multivariate Gaussian classification model based on the color and texture of the image to classify directly into facies. Method A classifies 64 % of the mudstone correctly and 20 % of the siltstone. The very fine sandstone is classified correctly for 84 % of the centimeter thick segments. Fine to coarse sandstone was classified correctly with an error less than 5%. The reason for the high misclassification of siltstone, mudstone and very fine sandstone is due to the similar characteristics of these lithologies. The boundary between the lithologies was unclear and the multivariate Gaussian classification model did not seem to be able to classify the complex shape of the data correctly.

Method B uses a hierarchical model that first classifies the sandstone and subsequently tries to distinguish between siltstone, mudstone and coal. To differentiate between the sandstone and other lithologies method B uses a quadratic decision boundary on the color data. Siltstone, mudstone and coal were subsequently classified by a linear decision boundary on the color and textural data. Due to the similar color characteristics of the finest sandstone Method B shows a misinterpretation of 51 % of this finest sandstone class. The fine to coarse sandstone class showed a misclassification less than 5 %. Mudstone was classified correctly for 84 % of the centimeter segments and siltstone was correctly classified for 31 % of the segments.

Overall the results obtained with method B showed to be more reliable, even though a smaller calibration set was used. The hierarchical structure of method B seems to capture the complex shape of the data better than method A.

10.1.3. Classification of grain size

Method A assigns the grain size directly based on the facies classification. Method B fits a linear model on the Auto-Covariance properties calibrated on the plug data to estimate the grain size.

The results of the grain size classification are evaluated with regards to the permeability; misclassification into a grain size class with dissimilar permeability characteristics is considered severe. When evaluating the results of method A and B, both methods show the largest severe misclassification in the very fine to medium grained sandstone.

For method A the average severe misclassification of very fine to medium grained sandstone was 47 %. For method B this misclassification is 45 %. The other grain size classes were represented much more accurately by method A and B showing a severe misclassification of less than 5 % in the coarse sandstone, mudstone and siltstone.

The large misclassification of sandstone occurred due to the misfit of the Auto-Covariance function and grain size. The most likely reasons that the Auto-Covariance function did not represent the grain size are a too low resolution of the core images and a wrong format of the core images that discards some of the color information (JPEG). Other reason that can cause the misfit are a more constant color of the grains in the fine grained sediment and the principal component analysis might have discarded useful information instead of noise.

10.1.4. Permeability estimation

The estimation of permeability has been compared to the null model; this null model assigns an average permeability extracted from plug data to each facies. Method A acts in a similar manner as the null model, where the only difference between the model is the initial classification of the facies (the null model uses the geologist's interpretation, whereas method A uses the techniques mentioned above). Method B estimates the permeability based on the Auto-Covariance function for sandstone, as the Auto-Covariance function was seen as a proxy for the grain size which is related to the permeability.

The permeability estimation performed by method A shows a root mean squared error that is 60 % higher compared to the null model (in the log space). This error is caused by misclassification of facies by method A. The chi-squared test showed similar results, where the scatter of the permeability estimation was significantly larger for most of the grain size classes (especially the very fine to fine sandstone).

The permeability estimation performed by method B shows a root mean squared error that is 30 % higher compared to the null model (in the log space). The average error that method B makes is an order of magnitude. The chi-squared test showed that the scatter of the permeability estimation of method B is significantly larger for 4 grain classes and significantly smaller for 3 grain classes compared to the null model. Method B thus shows relatively accurate results, especially when considering that the Auto-Covariance function did not show the expected strong relationship with grain size.

10.1.5. Overall

Method A does not seem to be able to identify the core adequately in terms of grain size and permeability. This was expected as method A is based around the same idea as the null model and any misclassification of method A would induce an error. Only if the facies could be extracted 100 % accurate, the method would show permeability estimation with a similar accuracy as the null model.

Method B, on the other hand, seems to identify a large portion of the core correctly and shows a permeability estimation that has an average error of an order of magnitude compared to the measurements. This error is comparable to the error made by the null model, which has an average error that is 30 % lower than method B. Thus a hierarchical program that first differentiates between sandstone and other lithologies and subsequently tries to estimate the permeability and grain size of the sandstone based on an Auto-Covariance function could describe the core relatively accurate. However, a stronger relationship of the Auto-Covariance function and grain size would be beneficial to the performance of the method.

If a method similar to method B could be incorporated into the core analysis it could hold advantages, especially when the program is fed other data to aid the classification in areas where this method alone gives ambiguous results (for example; gamma ray log to separate mudstone and siltstone). Other data should be present, as image analysis alone cannot distinguish between all facies (e.g. coal and mudstone). This would certainly be the case if cores with more complex characteristics than core E10-3 are examined.

To obtain high resolution core images on which image analysis can be performed, the core slabs could imaged right after the slabbing process. This way the image analysis results would be available to the geologist during its interpretation of the core. This initial guess of the program could aid the geologist in its interpretation of the core, as the program digitalizes an initial core description and the geologist would only need to check and adjust the programs interpretation.

10.2. Recommendations

This section introduces some recommendations which could be used by future studies on similar subjects.

Physical sample

- To be able to fully automate the image analysis process, the resin color that is used in the core boxes should be changed. The yellow color resembles the color of the sandstone, making it nearly impossible to accurately distinguish between the two. An unnatural color should be used (e.g. purple or pink).
- Another method that could be used to overcome this problem is by using a depth meter that locates all structures above the resin layer, i.e. the rock samples. Another advantage of a depth meter might be to extract a measure of the spatial texture of the core slab; this spatial texture could be used to extract the grain size.

Grain size extraction

- A higher image resolution than used in this research is preferable. The image resolution that was used for the Auto-Covariance extraction was 0.07x0.07 mm per pixel. At this resolution the Auto-Covariance function started to show a positive relation for medium grained sandstone. The finest sandstone in this research had an average grain size 6 times smaller than the medium grained sandstone. Thus the resolution should be at least 6 times higher; 0.012x0.012 mm per pixel. If the grain size of siltstone needs to be extracted, an even higher resolution is needed.
- Images should be saved in a different format. In this research JPEG images are used, though JPEG images discard a portion of the information to facilitate storage. The information that is discarded through the use of JPEG could be valuable. Storage in BMP or PNG format would exclude these errors.
- Another technique can be used for the extraction of grain size. For example, the technique proposed by *Buscombe (2013)* is said to be more accurate.
- The linear model used between the results of the Auto-Covariance function and permeability might not be the optimal method. Using a quadratic model could lead to better results.

Bedding direction

- In this research bedding direction was extracted from fractures in the core, identifying the fractures at an early stage would give a better result, especially in cores where bedding direction and the direction of fractures do not line up. Extracting the fractures would also give better results during the classification, because the fractures affect the average color that is extracted from the images.
- The bedding direction in a core is conventionally measured by a dip angle meter. This information was not available for core E10-3 and consequently the bedding direction needed to be extracted from the images itself. When the data of the dip angle meter is added to a routine that extracts the bedding direction from the images, the results should be more reliable.
- During this project an initial technique was used to describe the full bedding direction based on the direction of least standard deviation in color. This technique measured the bedding direction with a very low accuracy. The most common error was induced by homogeneous sections in the core.

Enhancing the current model

- A large part of the misclassification of fine sandstone occurs due to similar color properties of sandstone and mudstone, though these sections show a different texture. Due to the workflow of the model proposed in this research, this texture was not used during the classification into sandstone or mudstone/siltstone. If the data that was analyzed as mudstone underwent another step, to double check (quality assurance) if it is actually mudstone, this misclassification could potentially be reduced.
- The Auto-Covariance function showed a high amount of noise, smoothing of this Auto-Covariance function could be beneficial in terms of the ability of the function to describe the grain size.
- Using an object-based segmentation of the core, instead of a fixed segmentation at centimeter interval would limit the amount of segments that contain more than one facies. This would be beneficial during the classification into facies.

Further models

- The methods proposed in this research showed to be inaccurate in differentiating between mudstone and siltstone. Combining a gamma-ray log with the method could give better results, as the gamma-ray footprints of mudstone and siltstone are different, providing a means of differentiating between the two.
- The same holds for the interpretation of coal segments, which could easily be distinguished from other lithologies based on log data. If log data would be combined with image analysis, the results would be much better. This could potentially provide a model with a much higher accuracy than the present day standards.
- The images used in this experiment are regular images where data is located in the RGBD color space. Some of the lithologies that do not show a good separation in these spectra do give a good separation in infrared or ultraviolet. If images were to be taken in these spectra, the separation between different lithologies would be larger, reducing the chance of misclassification.
- The model could be enhanced by providing a set of possible paleo-environments. If the model could fit the data onto one of these scenarios, the model would give an early estimation of the paleo-environment and it could perhaps even show directional trends.

11. References

Aitchison, J., (1986), The Statistical Analysis of Compositional Data, *Chapman and Hall, 1986, p139-177.*

Akinyokun, O.C., Enikanselu, P.A., Adeyemo, A.B. and Adesida, A., (2009), Well Log Interpretation Model for the Determination of Lithology and Fluid Contents, *The Pacific Journal of Science and Technology, Volume 10, Number 1, may 2009*

Baptista, P., Cunha, T. R., Gama, C., Bernardes, C., (2012), A new and practical method to obtain grain size measurements in sandy shores based on digital image acquisition and processing, *Sedimentary Geology, Volume 282, p294-306*

Boels, J., (2003), Sedimentology, petrography and reservoir quality of the Upper Carboniferous in well e10-3, *Technical report, Panterra Nederland BV.*

Branets, L.V., Ghai, S.S., Lyons, S.L., Wu, X.H., (2009), Challenges and Technologies in Reservoir Modeling, *Communiations in computational physics, july 2009*

Buscombe, D., (2013), Transferable wavelet method for grain-size distribution from images of sediment surfaces and thin sections, and other natural granular patterns, J*ournal of the International Association of Sedimentologists, 2013*

Butler, J., Lane, S. and Chandler, J., (2001), Automated extraction of grain-size data from gravel surfaces using digital image processing. *Journal of hydraulic research, 39(5), p519-529*

Coll, C., Muggeridge, A. H., Jing, X. D., (2001), A new method to upscale waterflooding in heterogeneous reservoirs for a range of capillary and gravity effects, *SPE 74139*

Delfiner, P., Peyret, O., Serra, O., (1987), Automatic Determination of Lithology from Well Logs, *SPE Formation Evaluation Volume 2, Number 3*

Dussan V., Sharma, Y., (1992), Analysis of the Pressure Response of a Single-Probe Formation Tester, *SPE Formation Evaluation Volume 7, Number 2*

Fanchi, J.R., (1997), Principles of Applied Reservoir Simulation, *Gulf Publishing Co*

Forchheimer, P., (1901), Wasserbewegung durch Boden, *Zeits. V. Deutsh. Ing 45, p1782-1788*

Goggin, D. J., Thrasher, R. L., Lake, L. W., (1988), A Theoretical and Experimental Analysis of Minipermeameter Response Including Gas Slippage and High Velocity Flow Effects , *In Situ Number 1 and 2, p79-116*

Honarpour, M. M., Cullick, A. S., Saad, N., (1994), Influence of small-scale rock laminations on core plug oil/water relative permeability and capillary pressure, *SPE 27968*

Jones, S.C., (1994), A New, Fast, Accurate Pressure-Decay Probe Permeameter, *SPE Formation Evaluation Volume 9, Number 3*

Kanellos, M., (2005), New Life for Moore's Law, *CNET News.com, 19 April 2005*

Klinkenberg, L. J., (1941), The permeability of porous media to liquids and gases, Drilling and Production Practice, American Petroleum Inst., p200–213

Manrique, J.F., Georgi, D.T., Kasap E.,(1994), Effect of heterogeneity and anisotropy on probe Permeameter measurements, *SPWLA 35th Annual Logging Symposium, 1994*

Moore, G.E., (1965), Cramming more components onto integrated circuits, *Electronics April 1965, p114–117*

Rousseeuw, P.J, van Driessen, K., (1999), A Fast Algorithm for the Minimum Covariance Determinant Estimator, *Technometrics, August 1999, p212-223*

Rubin, D.M., (2004), A simple autocorrelation algorithm for determining grain size from digital images of sediment: *Journal of Sedimentary Research, 74, p160-165.*

Taylor, J.R., (1982), An introduction to error analysis, *University Science Press, Mill Valley CA, p270*

Thomas, A., Rider, M., Curtis A., MacArthur, A. (2011), Automated lithology extraction from core photographs, *first break volume 29, June 2011*

Wong, K.W., Chun Che Fung, Myers, D. A, (1999), Generalised neural-fuzzy well log interpretation model with a reduced rule base, *Neural Information Processing (1999)*

Appendix A

This appendix shows the Permeability distribution of different grain size groups, based on the data obtained by Hassler Sleeve Plug analysis (Figure 52). From this figure it becomes apparent that the sandstone shows a strong relation with grain size, especially from grain size S1u to S4l.

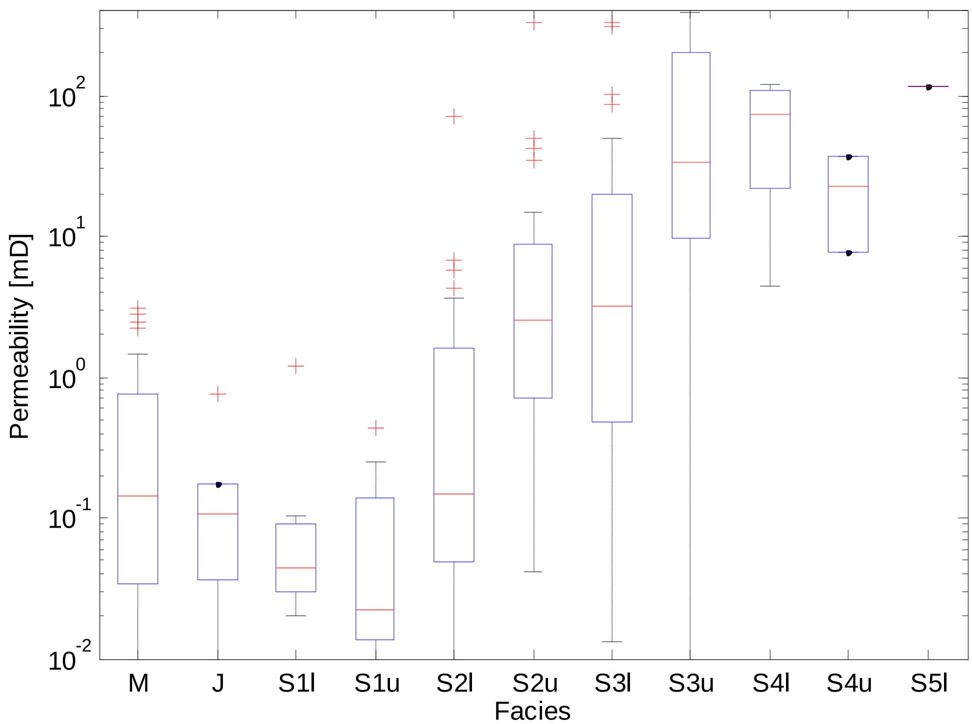

Figure 52: Box plot of permeability distribution of facies present in the core.

Appendix B

This appendix shows the full results of the research. For each core slab a plot of permeability of both methods against the geologist's interpretation of the permeability is shown.

The core image of each core slab is shown, with the full segmentation model applied on it. In this segmentation model the Green lines indicate 'reliable' angles obtained from the statistical analysis of the correlation results. Red lines indicate a direct interpolation of the dip angles between two similar 'reliable' angles. Blue lines indicate the dip angles that were analyzed by the scenario fitting routine. Black lines indicate an interpolation between 'reliable' dip angles that are located in different images.

Below each figure three colorbars are visible, these colorbars represent the grain size/facies interpretation of method A (top), method B (middle) and the geologist (bottom). The legends for all images in this appendix are shown below.

Legend for the plots

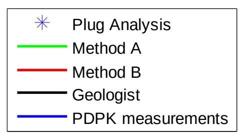

Legend for the colorbars (top to bottom: method A, method B and geologist's interpretation)

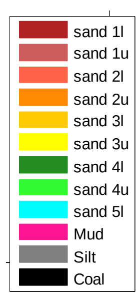

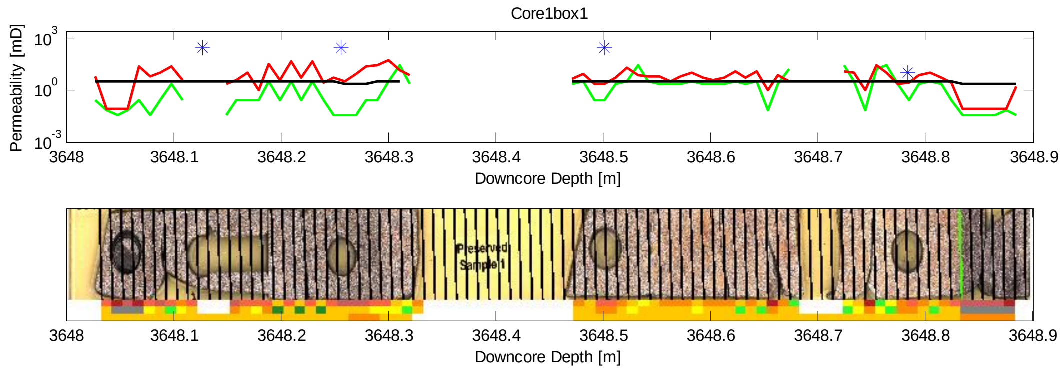
Core1box1
Permeability [mD]
10^3
10^0
10^{-3}
3648 3648.1 3648.2 3648.3 3648.4 3648.5 3648.6 3648.7 3648.8 3648.9
Downcore Depth [m]
Preserved Sample 1
3648 3648.1 3648.2 3648.3 3648.4 3648.5 3648.6 3648.7 3648.8 3648.9
Downcore Depth [m]

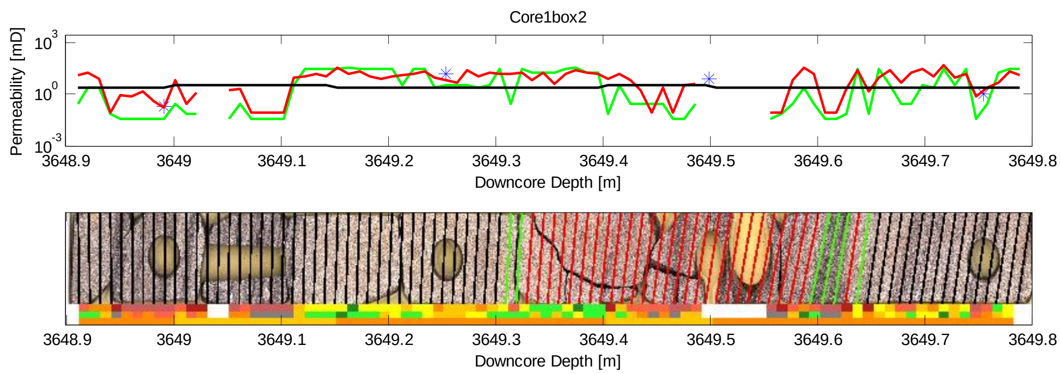
Core1box2
Permeability [mD]
10^3
10^0
10^{-3}
3648.9 3649 3649.1 3649.2 3649.3 3649.4 3649.5 3649.6 3649.7 3649.8
Downcore Depth [m]
3648.9 3649 3649.1 3649.2 3649.3 3649.4 3649.5 3649.6 3649.7 3649.8
Downcore Depth [m]

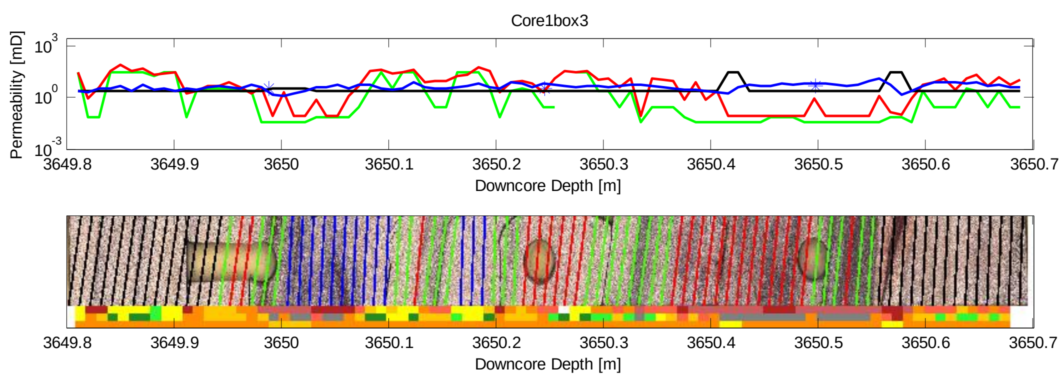
Core1box3
Permeability [mD]
10^3
10^0
10^{-3}
3649.8 3649.9 3650 3650.1 3650.2 3650.3 3650.4 3650.5 3650.6 3650.7
Downcore Depth [m]
3649.8 3649.9 3650 3650.1 3650.2 3650.3 3650.4 3650.5 3650.6 3650.7
Downcore Depth [m]

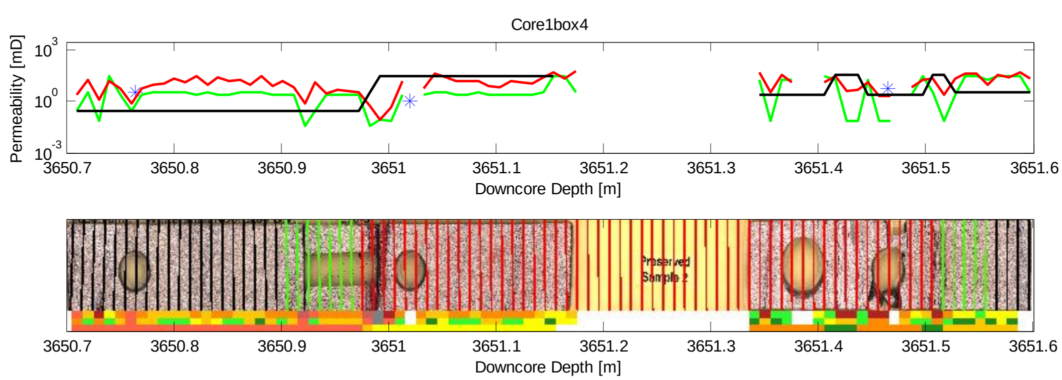
Core1box4
Permeability [mD]
10^3
10^0
10^{-3}
3650.7 3650.8 3650.9 3651 3651.1 3651.2 3651.3 3651.4 3651.5 3651.6
Downcore Depth [m]
Preserved Sample 2
3650.7 3650.8 3650.9 3651 3651.1 3651.2 3651.3 3651.4 3651.5 3651.6
Downcore Depth [m]

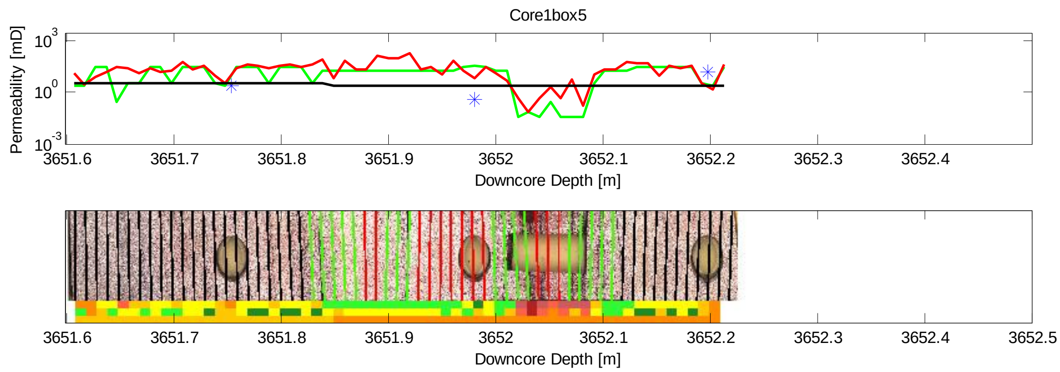
Core1box5
Permeability [mD]
10^3
10^0
10^{-3}
3651.6 3651.7 3651.8 3651.9 3652 3652.1 3652.2 3652.3 3652.4
Downcore Depth [m]
3651.6 3651.7 3651.8 3651.9 3652 3652.1 3652.2 3652.3 3652.4 3652.5
Downcore Depth [m]

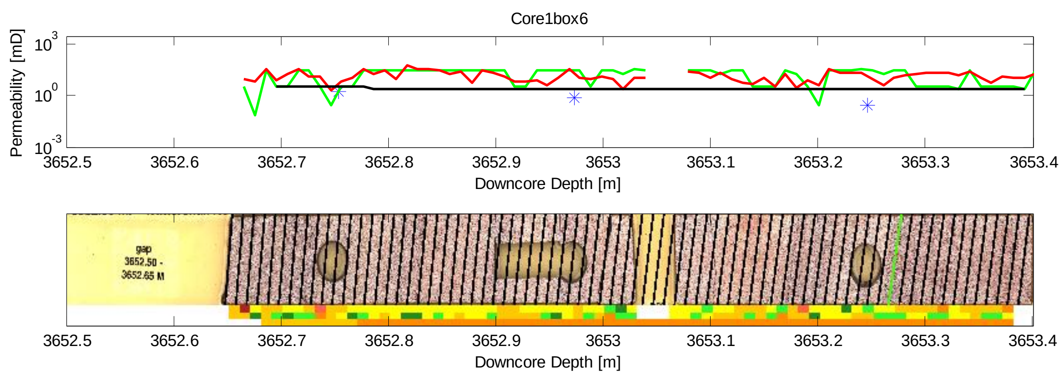
Core1box6
Permeability [mD]
10^3
10^0
10^{-3}
3652.5 3652.6 3652.7 3652.8 3652.9 3653 3653.1 3653.2 3653.3 3653.4
Downcore Depth [m]
gap
3652.50 -
3652.65 M
3652.5 3652.6 3652.7 3652.8 3652.9 3653 3653.1 3653.2 3653.3 3653.4
Downcore Depth [m]

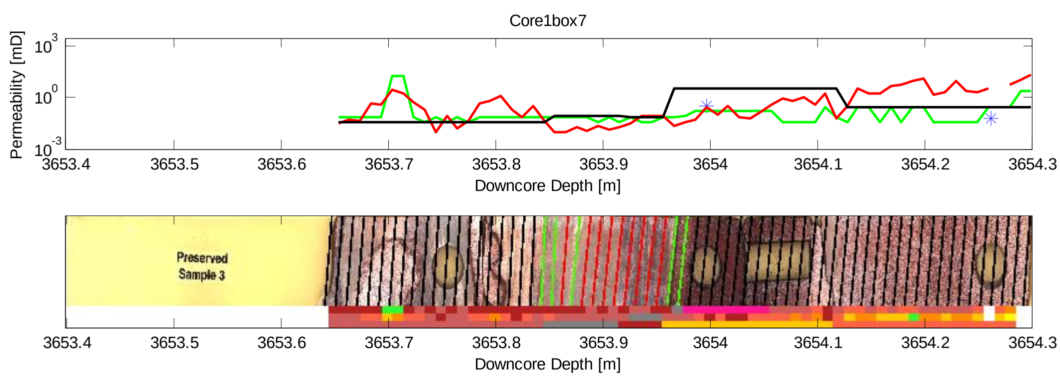
Core1box7
Permeability [mD]
10^3
10^0
10^{-3}
3653.4 3653.5 3653.6 3653.7 3653.8 3653.9 3654 3654.1 3654.2 3654.3
Downcore Depth [m]
Preserved
Sample 3
3653.4 3653.5 3653.6 3653.7 3653.8 3653.9 3654 3654.1 3654.2 3654.3
Downcore Depth [m]

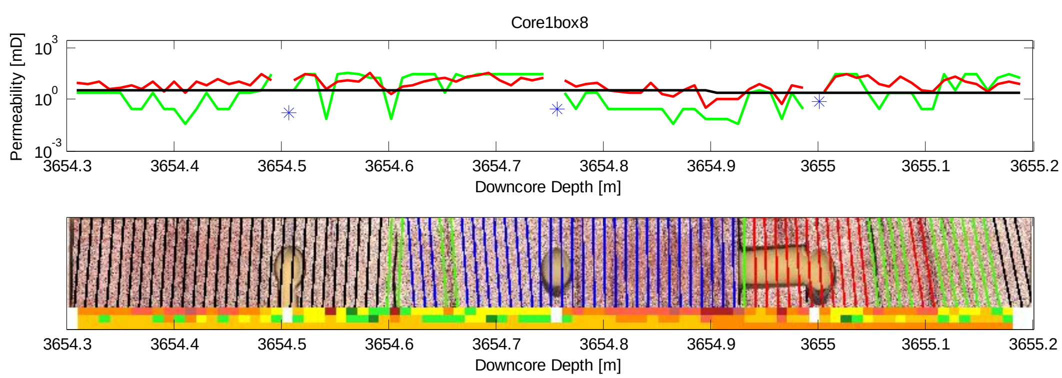
Core1box8
Permeability [mD]
10^3
10^0
10^{-3}
3654.3 3654.4 3654.5 3654.6 3654.7 3654.8 3654.9 3655 3655.1 3655.2
Downcore Depth [m]
3654.3 3654.4 3654.5 3654.6 3654.7 3654.8 3654.9 3655 3655.1 3655.2
Downcore Depth [m]

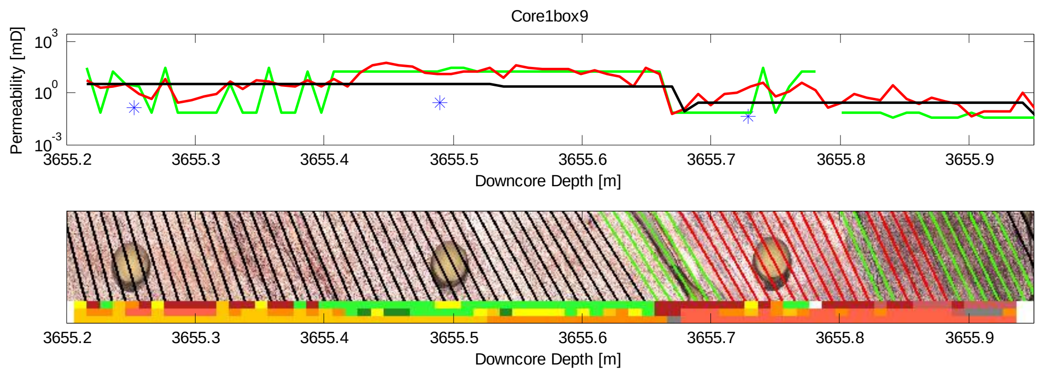
Core1box9
Permeability [mD]
10^3
10^0
10^-3
3655.2 3655.3 3655.4 3655.5 3655.6 3655.7 3655.8 3655.9
Downcore Depth [m]
3655.2 3655.3 3655.4 3655.5 3655.6 3655.7 3655.8 3655.9
Downcore Depth [m]

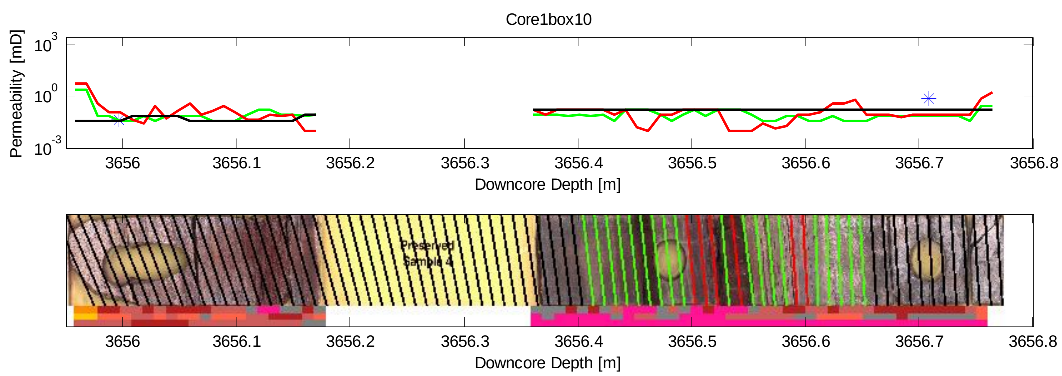
Core1box10
Permeability [mD]
10^3
10^0
10^-3
3656 3656.1 3656.2 3656.3 3656.4 3656.5 3656.6 3656.7 3656.8
Downcore Depth [m]
Preserved Sample 4
3656 3656.1 3656.2 3656.3 3656.4 3656.5 3656.6 3656.7 3656.8
Downcore Depth [m]

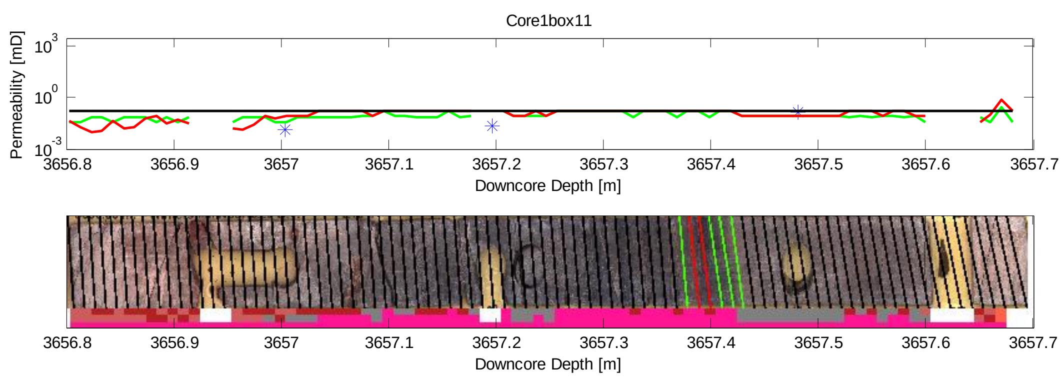
Core1box11
Permeability [mD]
10^3
10^0
10^-3
3656.8 3656.9 3657 3657.1 3657.2 3657.3 3657.4 3657.5 3657.6 3657.7
Downcore Depth [m]
3656.8 3656.9 3657 3657.1 3657.2 3657.3 3657.4 3657.5 3657.6 3657.7
Downcore Depth [m]

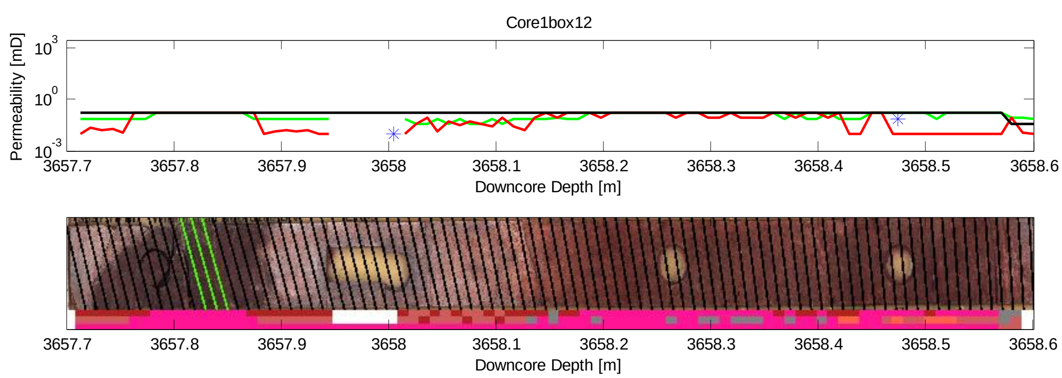
Core1box12
Permeability [mD]
10^3
10^0
10^-3
3657.7 3657.8 3657.9 3658 3658.1 3658.2 3658.3 3658.4 3658.5 3658.6
Downcore Depth [m]
3657.7 3657.8 3657.9 3658 3658.1 3658.2 3658.3 3658.4 3658.5 3658.6
Downcore Depth [m]

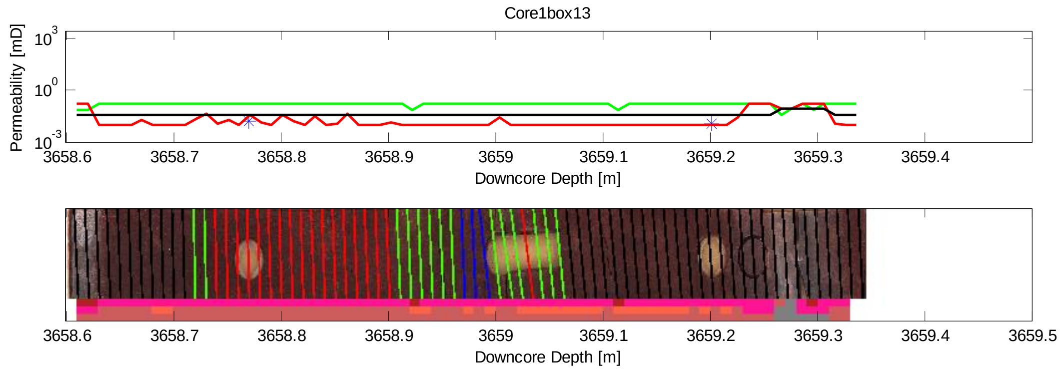
Core1box13
Permeability [mD]
Downcore Depth [m]
3658.6 3658.7 3658.8 3658.9 3659 3659.1 3659.2 3659.3 3659.4 3659.5

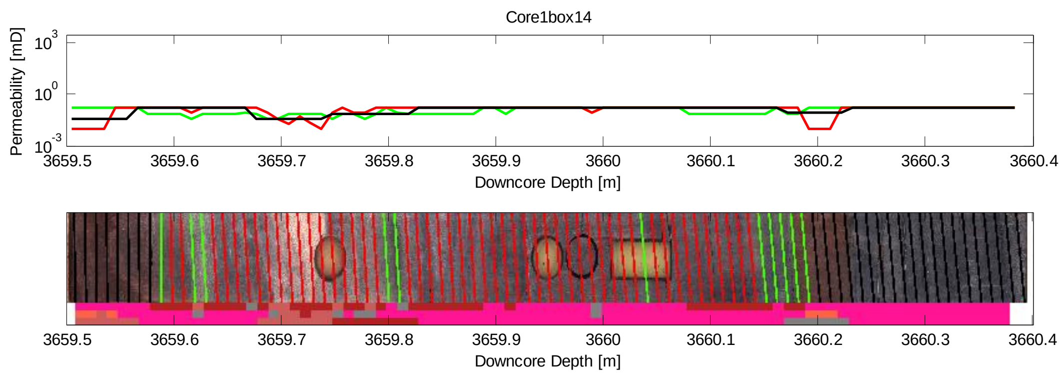
Core1box14
Permeability [mD]
Downcore Depth [m]
3659.5 3659.6 3659.7 3659.8 3659.9 3660 3660.1 3660.2 3660.3 3660.4

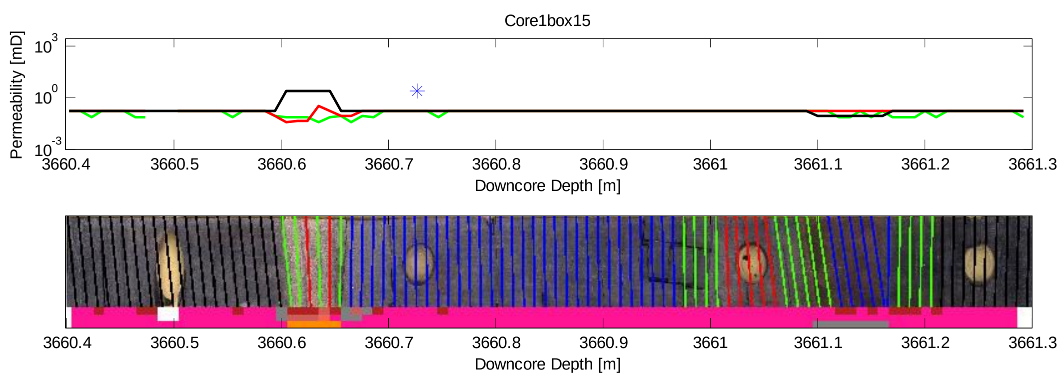
Core1box15
Permeability [mD]
Downcore Depth [m]
3660.4 3660.5 3660.6 3660.7 3660.8 3660.9 3661 3661.1 3661.2 3661.3

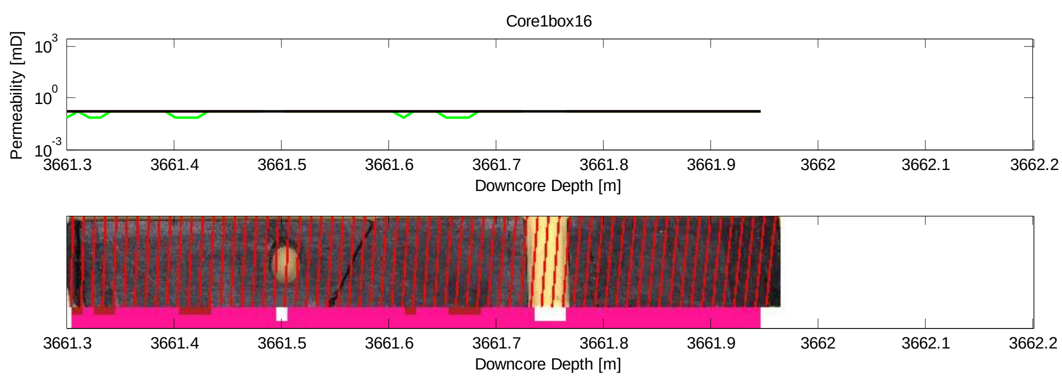
Core1box16
Permeability [mD]
Downcore Depth [m]
3661.3 3661.4 3661.5 3661.6 3661.7 3661.8 3661.9 3662 3662.1 3662.2

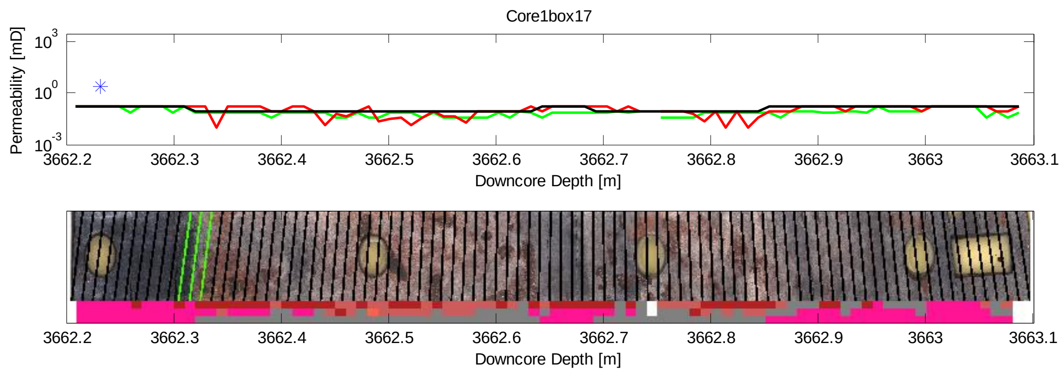
Core1box17
Permeability [mD]
10^3
10^0
10^-3
3662.2 3662.3 3662.4 3662.5 3662.6 3662.7 3662.8 3662.9 3663 3663.1
Downcore Depth [m]
3662.2 3662.3 3662.4 3662.5 3662.6 3662.7 3662.8 3662.9 3663 3663.1
Downcore Depth [m]

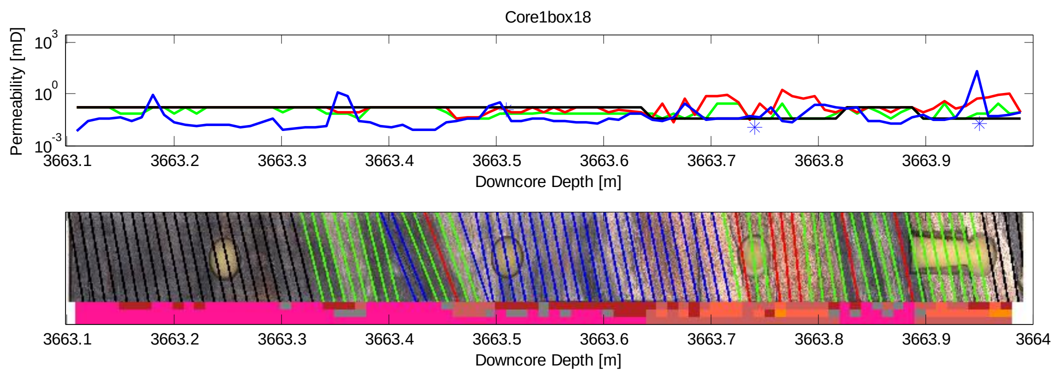
Core1box18
Permeability [mD]
10^3
10^0
10^-3
3663.1 3663.2 3663.3 3663.4 3663.5 3663.6 3663.7 3663.8 3663.9
Downcore Depth [m]
3663.1 3663.2 3663.3 3663.4 3663.5 3663.6 3663.7 3663.8 3663.9 3664
Downcore Depth [m]

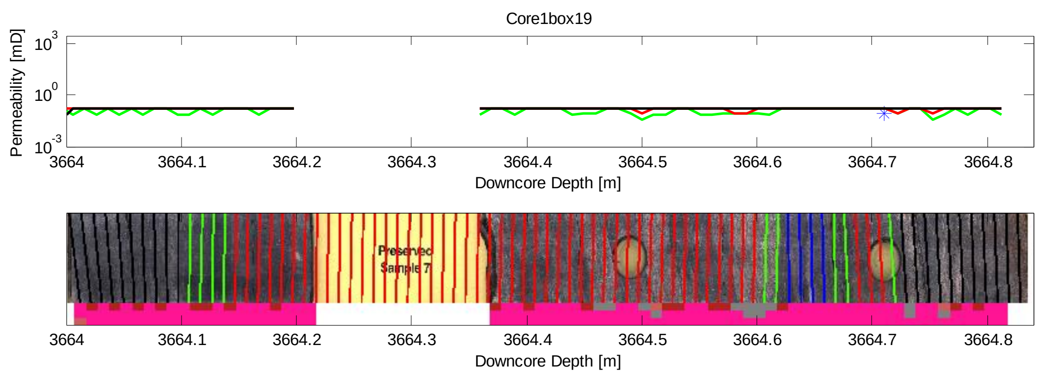
Core1box19
Permeability [mD]
10^3
10^0
10^-3
3664 3664.1 3664.2 3664.3 3664.4 3664.5 3664.6 3664.7 3664.8
Downcore Depth [m]
Preserved Sample 7
3664 3664.1 3664.2 3664.3 3664.4 3664.5 3664.6 3664.7 3664.8
Downcore Depth [m]

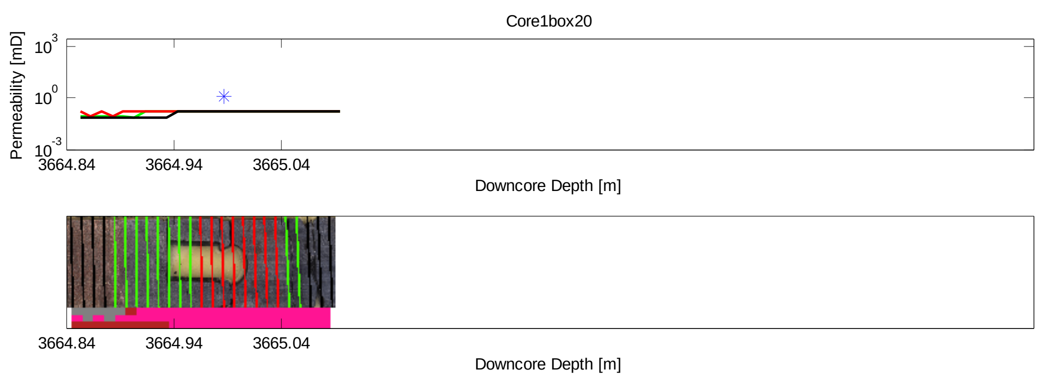
Core1box20
Permeability [mD]
10^3
10^0
10^-3
3664.84 3664.94 3665.04
Downcore Depth [m]
3664.84 3664.94 3665.04
Downcore Depth [m]

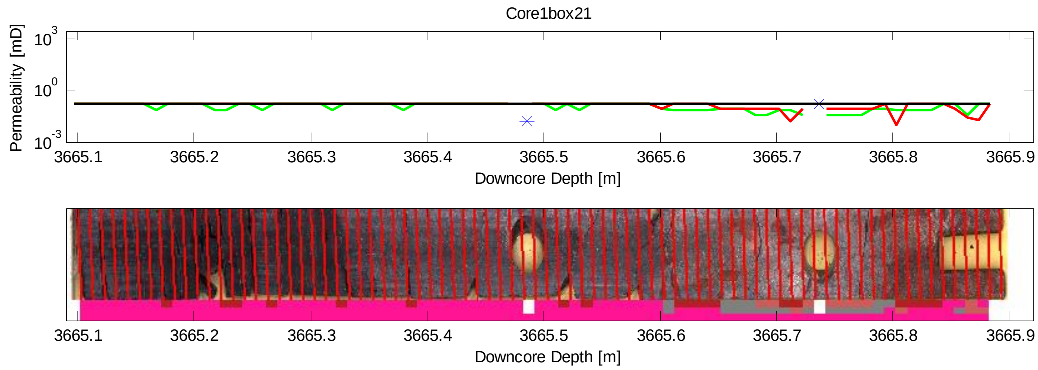
Core1box21
Permeability [mD]
10^3
10^0
10^{-3}
3665.1 3665.2 3665.3 3665.4 3665.5 3665.6 3665.7 3665.8 3665.9
Downcore Depth [m]
3665.1 3665.2 3665.3 3665.4 3665.5 3665.6 3665.7 3665.8 3665.9
Downcore Depth [m]

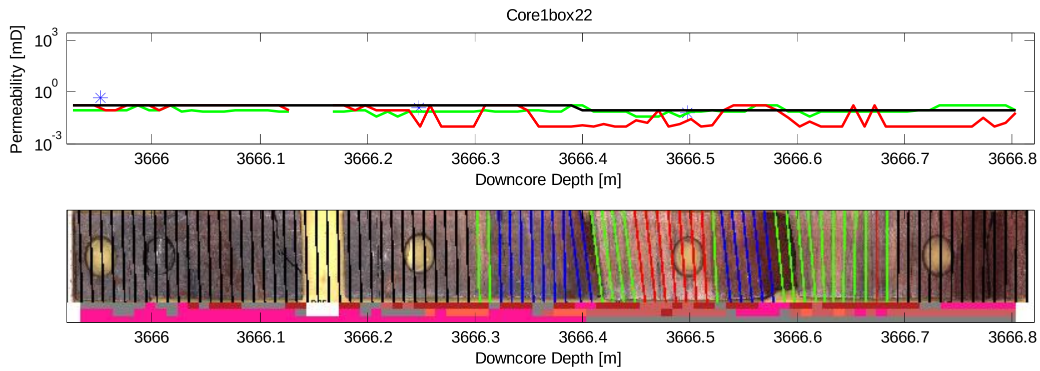
Core1box22
Permeability [mD]
10^3
10^0
10^{-3}
3666 3666.1 3666.2 3666.3 3666.4 3666.5 3666.6 3666.7 3666.8
Downcore Depth [m]
3666 3666.1 3666.2 3666.3 3666.4 3666.5 3666.6 3666.7 3666.8
Downcore Depth [m]

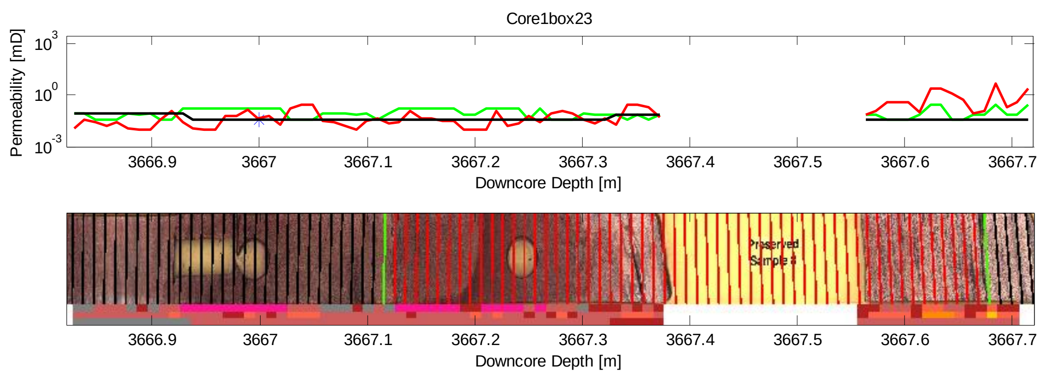
Core1box23
Permeability [mD]
10^3
10^0
10^{-3}
3666.9 3667 3667.1 3667.2 3667.3 3667.4 3667.5 3667.6 3667.7
Downcore Depth [m]
Preserved Sample #
3666.9 3667 3667.1 3667.2 3667.3 3667.4 3667.5 3667.6 3667.7
Downcore Depth [m]

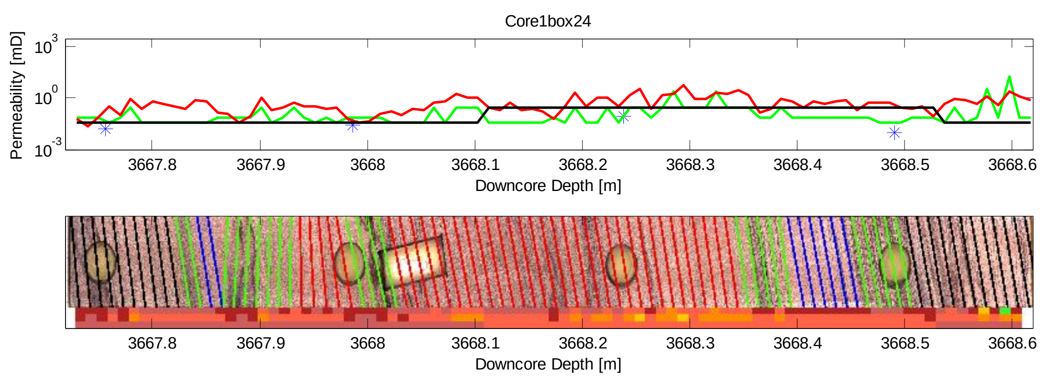
Core1box24
Permeability [mD]
10^3
10^0
10^{-3}
3667.8 3667.9 3668 3668.1 3668.2 3668.3 3668.4 3668.5 3668.6
Downcore Depth [m]
3667.8 3667.9 3668 3668.1 3668.2 3668.3 3668.4 3668.5 3668.6
Downcore Depth [m]

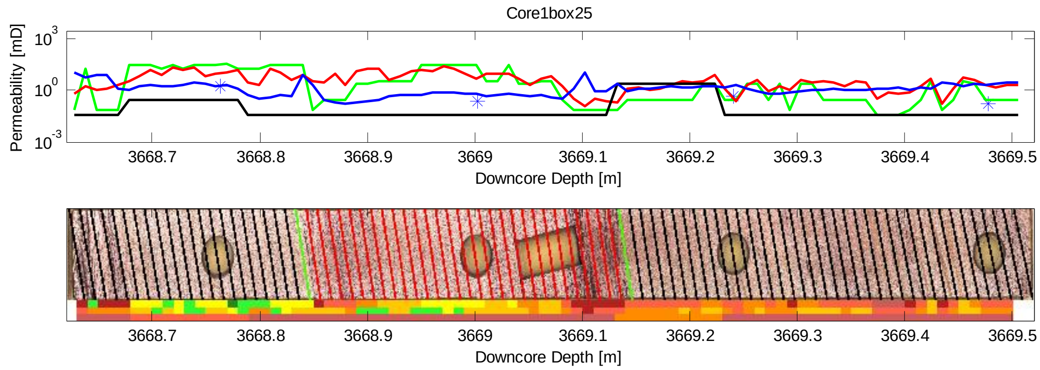
Core1box25
Permeability [mD]
10^3
10^0
10^-3
3668.7 3668.8 3668.9 3669 3669.1 3669.2 3669.3 3669.4 3669.5
Downcore Depth [m]
3668.7 3668.8 3668.9 3669 3669.1 3669.2 3669.3 3669.4 3669.5
Downcore Depth [m]

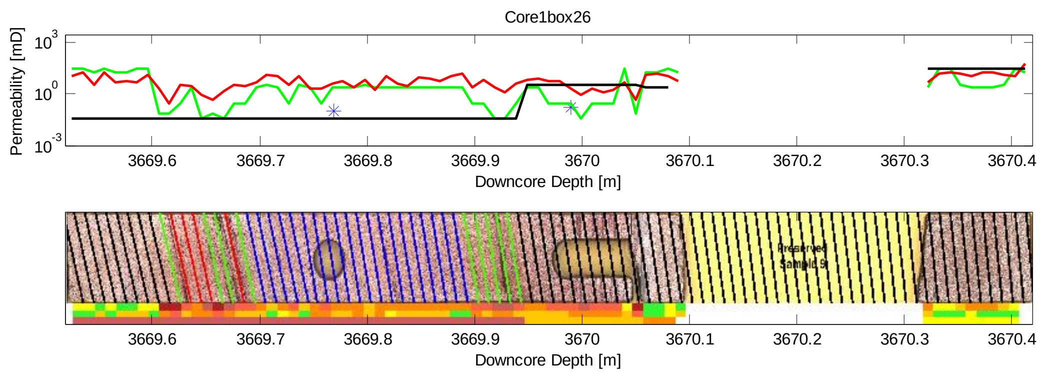
Core1box26
Permeability [mD]
10^3
10^0
10^-3
3669.6 3669.7 3669.8 3669.9 3670 3670.1 3670.2 3670.3 3670.4
Downcore Depth [m]
3669.6 3669.7 3669.8 3669.9 3670 3670.1 3670.2 3670.3 3670.4
Downcore Depth [m]

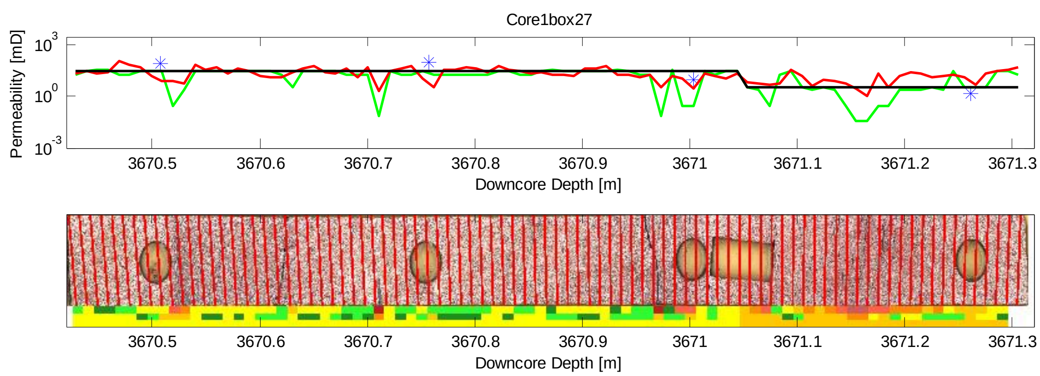
Core1box27
Permeability [mD]
10^3
10^0
10^-3
3670.5 3670.6 3670.7 3670.8 3670.9 3671 3671.1 3671.2 3671.3
Downcore Depth [m]
3670.5 3670.6 3670.7 3670.8 3670.9 3671 3671.1 3671.2 3671.3
Downcore Depth [m]

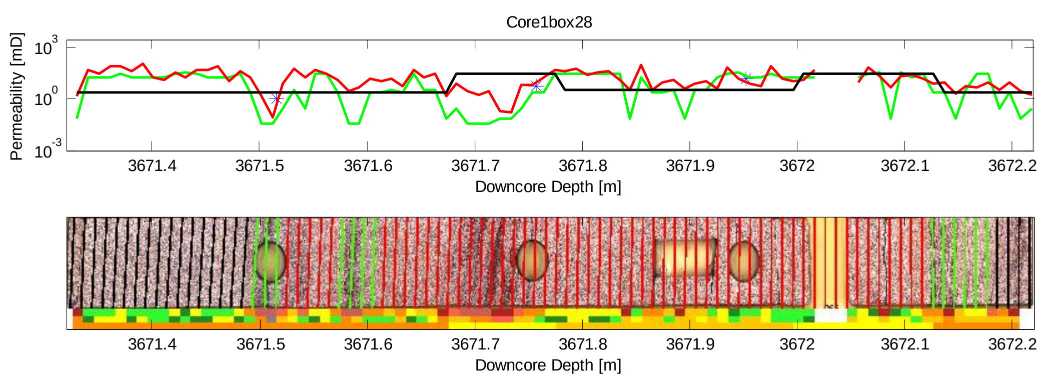
Core1box28
Permeability [mD]
10^3
10^0
10^-3
3671.4 3671.5 3671.6 3671.7 3671.8 3671.9 3672 3672.1 3672.2
Downcore Depth [m]
3671.4 3671.5 3671.6 3671.7 3671.8 3671.9 3672 3672.1 3672.2
Downcore Depth [m]

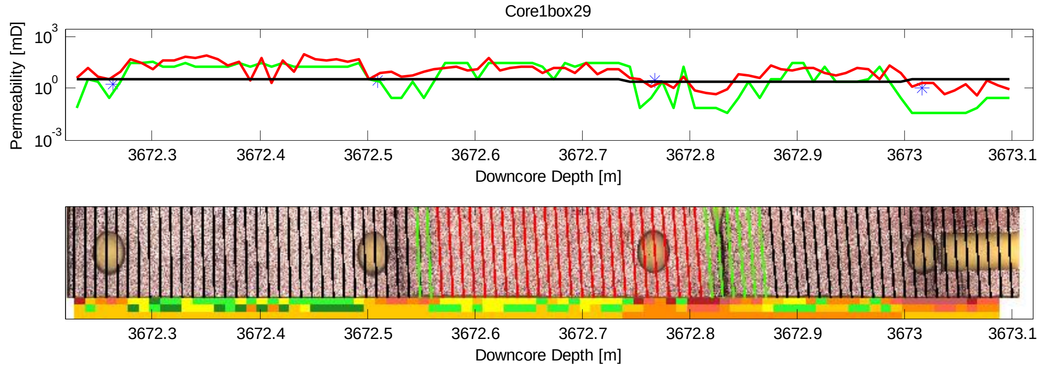
Core1box29
Permeability [mD]
10^3
10^0
10^-3
3672.3 3672.4 3672.5 3672.6 3672.7 3672.8 3672.9 3673 3673.1
Downcore Depth [m]
3672.3 3672.4 3672.5 3672.6 3672.7 3672.8 3672.9 3673 3673.1
Downcore Depth [m]

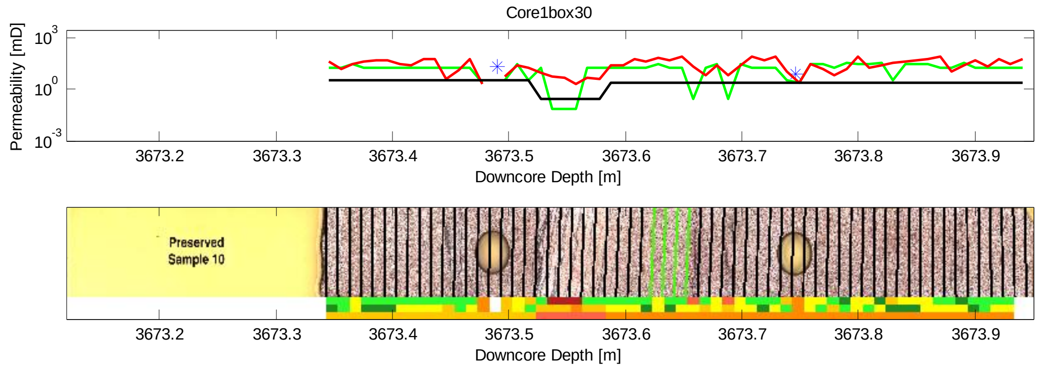
Core1box30
Permeability [mD]
10^3
10^0
10^-3
3673.2 3673.3 3673.4 3673.5 3673.6 3673.7 3673.8 3673.9
Downcore Depth [m]
Preserved
Sample 10
3673.2 3673.3 3673.4 3673.5 3673.6 3673.7 3673.8 3673.9
Downcore Depth [m]

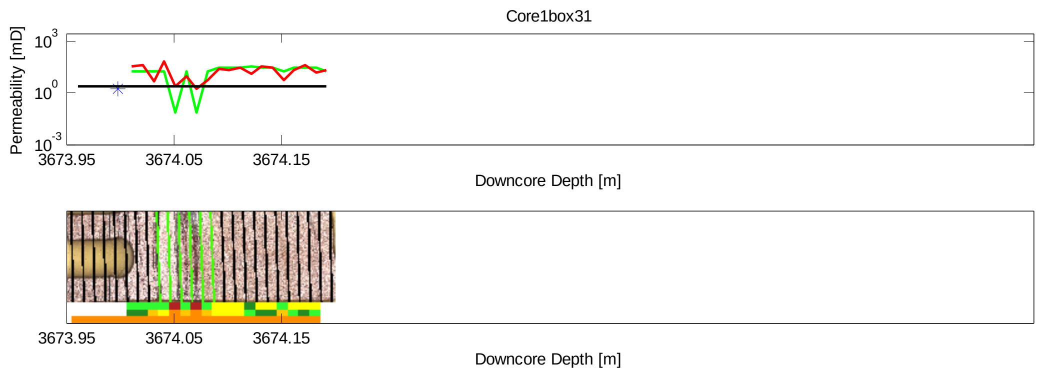
Core1box31
Permeability [mD]
10^3
10^0
10^-3
3673.95 3674.05 3674.15
Downcore Depth [m]
3673.95 3674.05 3674.15
Downcore Depth [m]

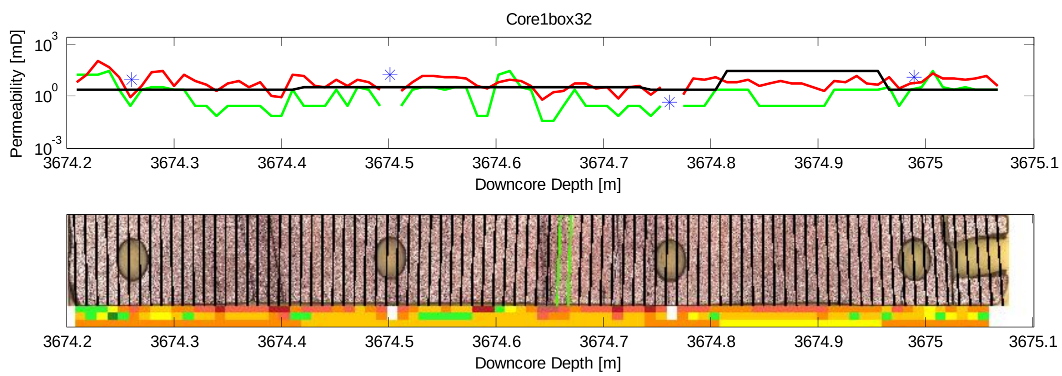
Core1box32
Permeability [mD]
10^3
10^0
10^-3
3674.2 3674.3 3674.4 3674.5 3674.6 3674.7 3674.8 3674.9 3675 3675.1
Downcore Depth [m]
3674.2 3674.3 3674.4 3674.5 3674.6 3674.7 3674.8 3674.9 3675 3675.1
Downcore Depth [m]

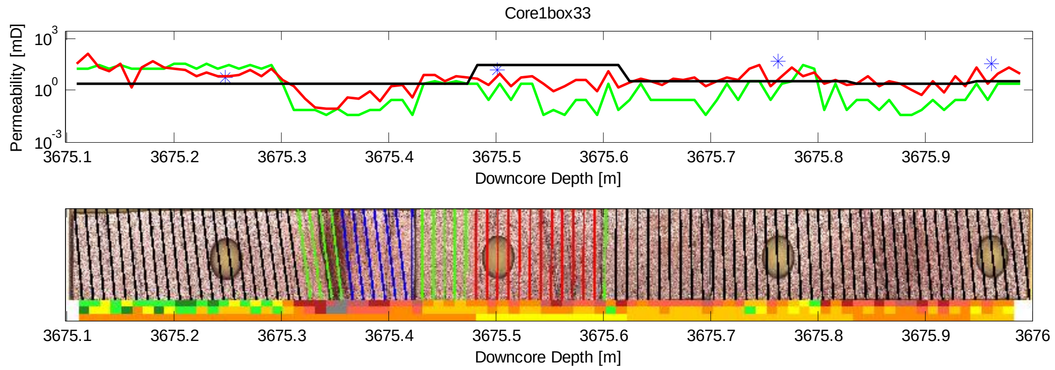
Core1box33
Permeability [mD]
10^3
10^0
10^{-3}
3675.1 3675.2 3675.3 3675.4 3675.5 3675.6 3675.7 3675.8 3675.9
Downcore Depth [m]
3675.1 3675.2 3675.3 3675.4 3675.5 3675.6 3675.7 3675.8 3675.9 3676
Downcore Depth [m]

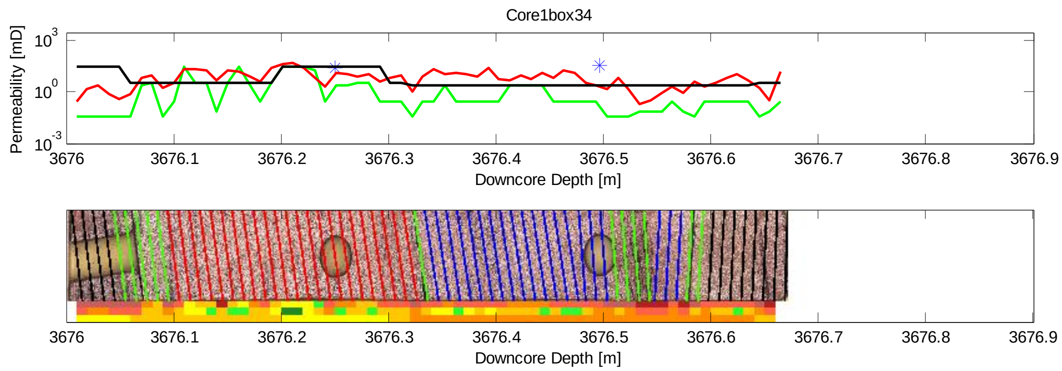
Core1box34
Permeability [mD]
10^3
10^0
10^{-3}
3676 3676.1 3676.2 3676.3 3676.4 3676.5 3676.6 3676.7 3676.8 3676.9
Downcore Depth [m]
3676 3676.1 3676.2 3676.3 3676.4 3676.5 3676.6 3676.7 3676.8 3676.9
Downcore Depth [m]

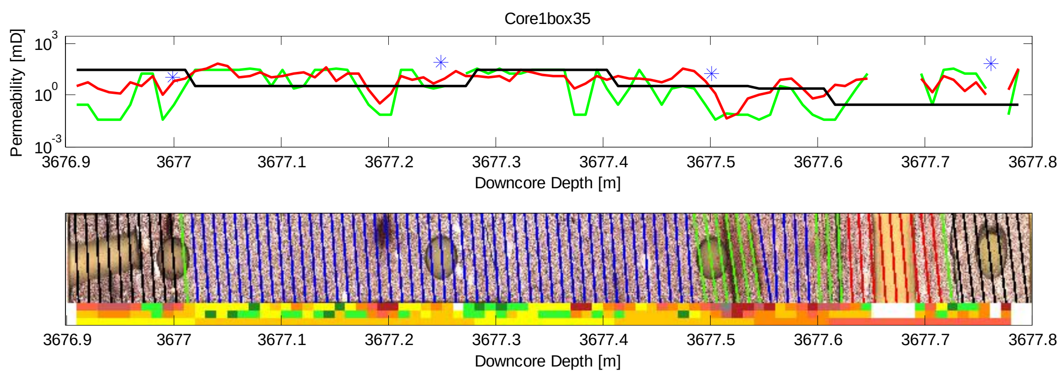
Core1box35
Permeability [mD]
10^3
10^0
10^{-3}
3676.9 3677 3677.1 3677.2 3677.3 3677.4 3677.5 3677.6 3677.7 3677.8
Downcore Depth [m]
3676.9 3677 3677.1 3677.2 3677.3 3677.4 3677.5 3677.6 3677.7 3677.8
Downcore Depth [m]

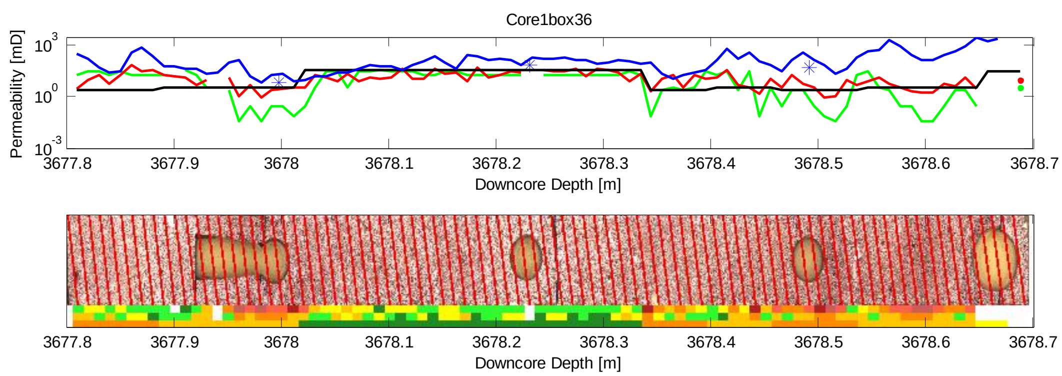
Core1box36
Permeability [mD]
10^3
10^0
10^{-3}
3677.8 3677.9 3678 3678.1 3678.2 3678.3 3678.4 3678.5 3678.6 3678.7
Downcore Depth [m]
3677.8 3677.9 3678 3678.1 3678.2 3678.3 3678.4 3678.5 3678.6 3678.7
Downcore Depth [m]

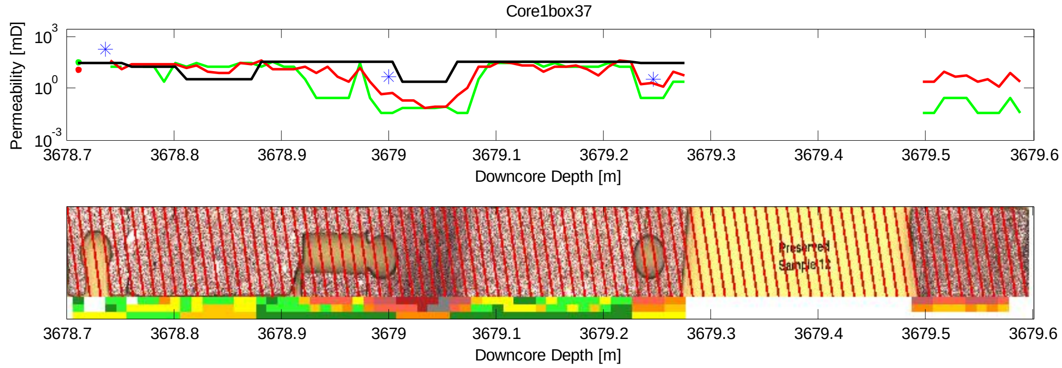
Core1box37
Permeability [mD]
Downcore Depth [m]
Downcore Depth [m]

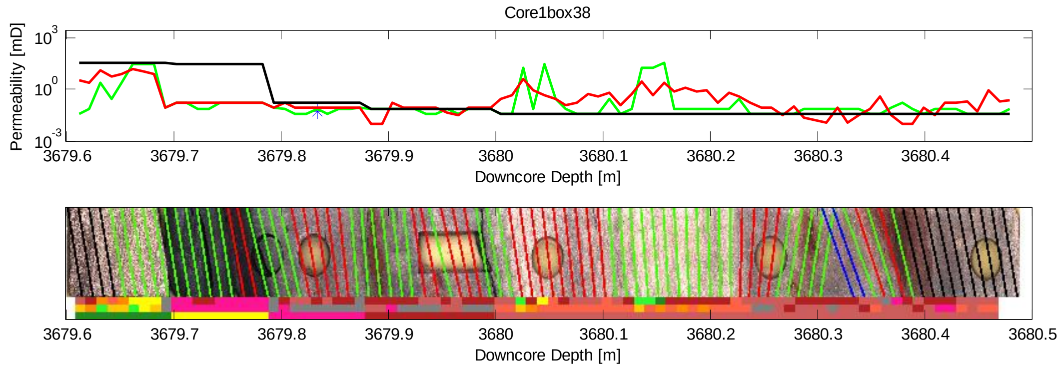
Core1box38
Permeability [mD]
Downcore Depth [m]
Downcore Depth [m]

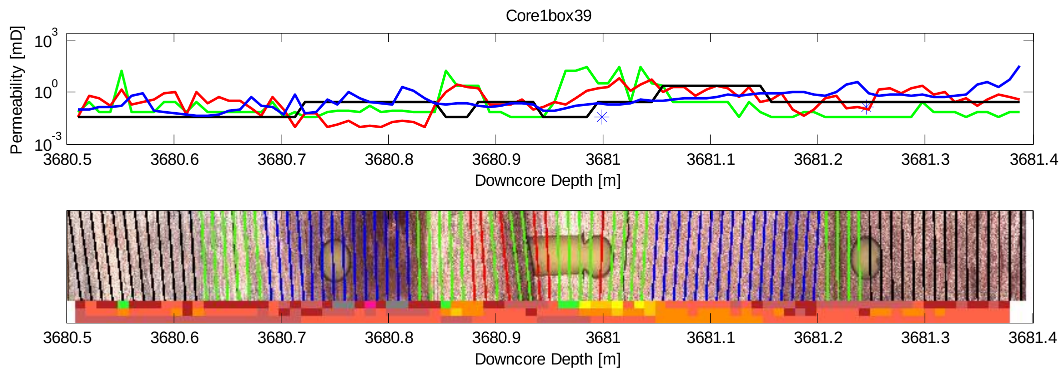
Core1box39
Permeability [mD]
Downcore Depth [m]
Downcore Depth [m]

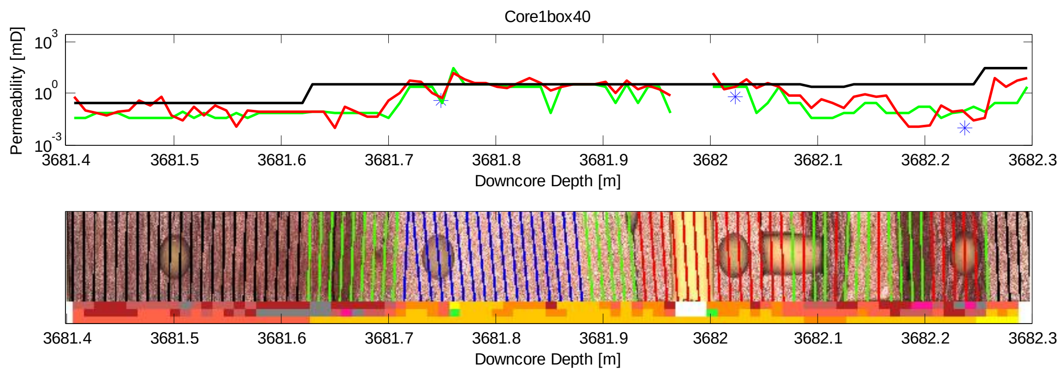
Core1box40
Permeability [mD]
Downcore Depth [m]
Downcore Depth [m]

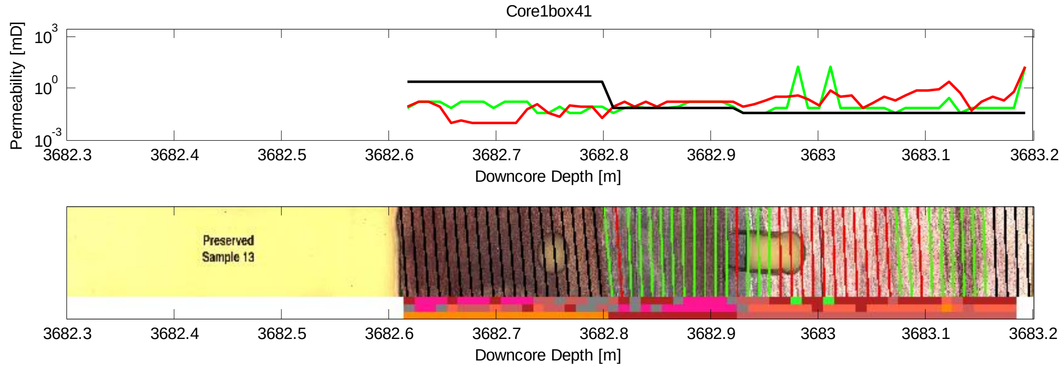
Core1box41
Permeability [mD]
10^3
10^0
10^-3
3682.3 3682.4 3682.5 3682.6 3682.7 3682.8 3682.9 3683 3683.1 3683.2
Downcore Depth [m]
Preserved
Sample 13
3682.3 3682.4 3682.5 3682.6 3682.7 3682.8 3682.9 3683 3683.1 3683.2
Downcore Depth [m]

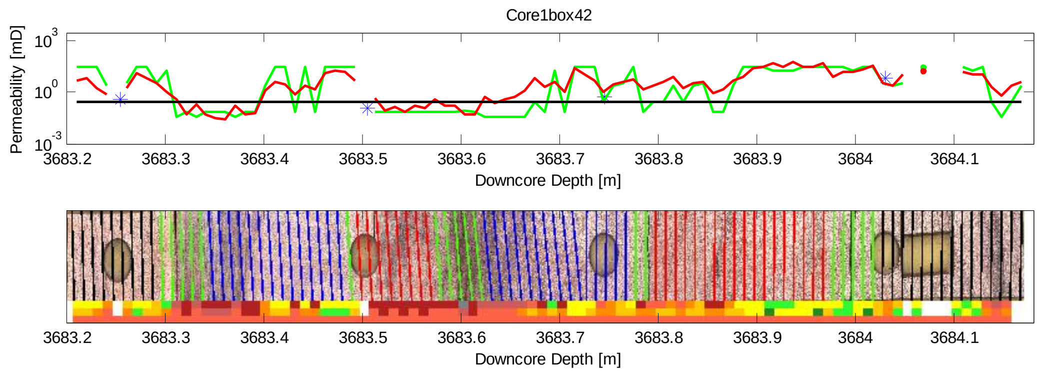
Core1box42
Permeability [mD]
10^3
10^0
10^-3
3683.2 3683.3 3683.4 3683.5 3683.6 3683.7 3683.8 3683.9 3684 3684.1
Downcore Depth [m]
3683.2 3683.3 3683.4 3683.5 3683.6 3683.7 3683.8 3683.9 3684 3684.1
Downcore Depth [m]

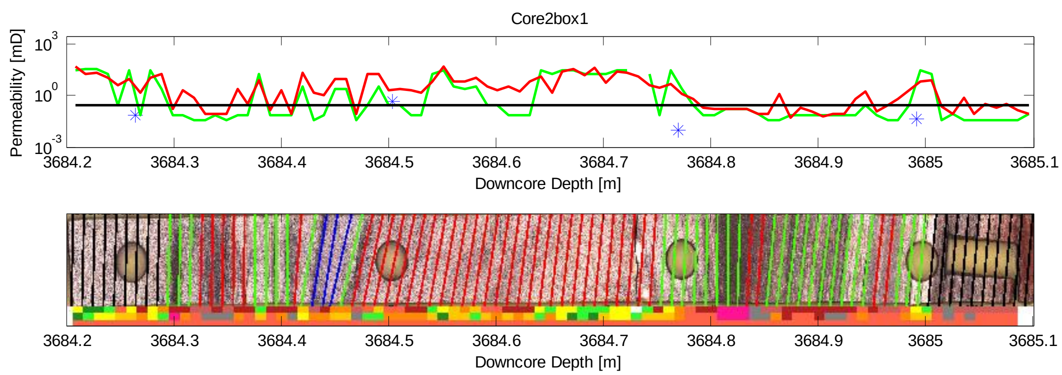
Core2box1
Permeability [mD]
10^3
10^0
10^-3
3684.2 3684.3 3684.4 3684.5 3684.6 3684.7 3684.8 3684.9 3685 3685.1
Downcore Depth [m]
3684.2 3684.3 3684.4 3684.5 3684.6 3684.7 3684.8 3684.9 3685 3685.1
Downcore Depth [m]

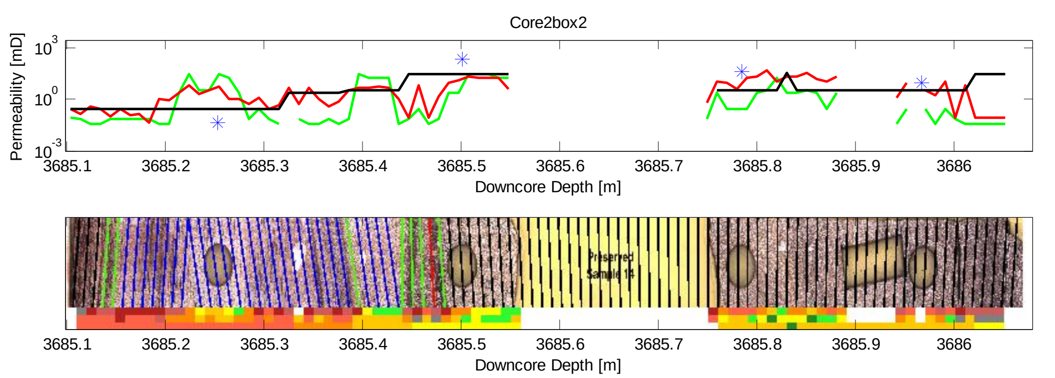
Core2box2
Permeability [mD]
10^3
10^0
10^-3
3685.1 3685.2 3685.3 3685.4 3685.5 3685.6 3685.7 3685.8 3685.9 3686
Downcore Depth [m]
3685.1 3685.2 3685.3 3685.4 3685.5 3685.6 3685.7 3685.8 3685.9 3686
Downcore Depth [m]

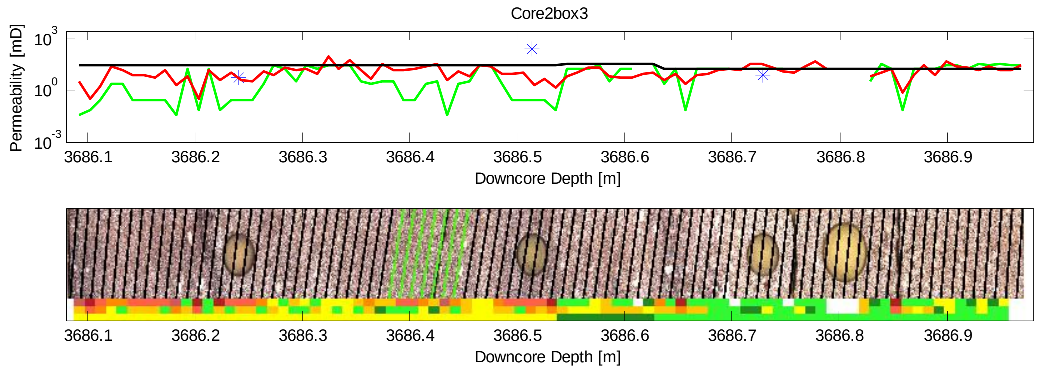
Core2box3
Permeability [mD]
10^3
10^0
10^{-3}
3686.1 3686.2 3686.3 3686.4 3686.5 3686.6 3686.7 3686.8 3686.9
Downcore Depth [m]
3686.1 3686.2 3686.3 3686.4 3686.5 3686.6 3686.7 3686.8 3686.9
Downcore Depth [m]

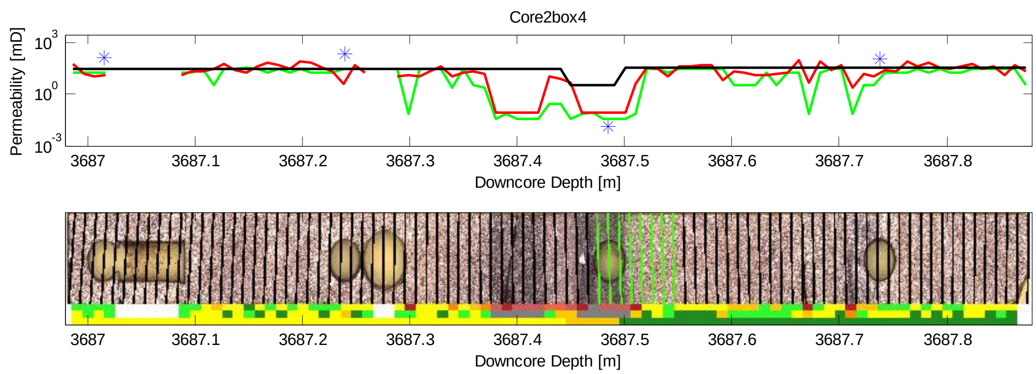
Core2box4
Permeability [mD]
10^3
10^0
10^{-3}
3687 3687.1 3687.2 3687.3 3687.4 3687.5 3687.6 3687.7 3687.8
Downcore Depth [m]
3687 3687.1 3687.2 3687.3 3687.4 3687.5 3687.6 3687.7 3687.8
Downcore Depth [m]

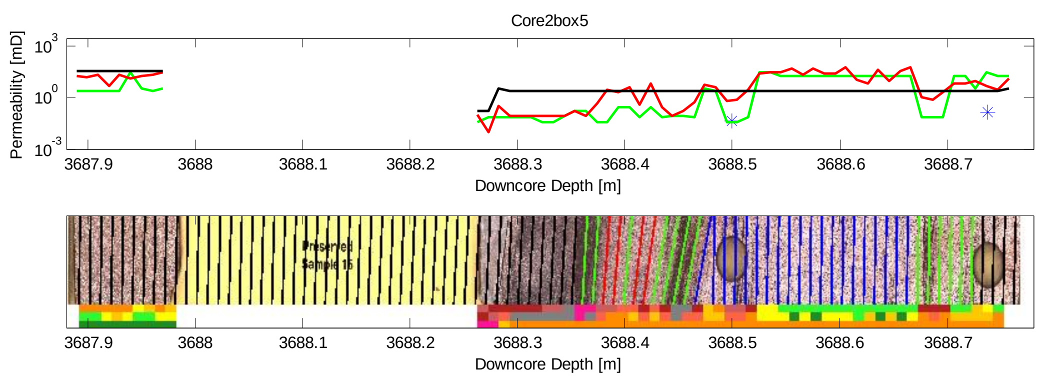
Core2box5
Permeability [mD]
10^3
10^0
10^{-3}
3687.9 3688 3688.1 3688.2 3688.3 3688.4 3688.5 3688.6 3688.7
Downcore Depth [m]
Preserved Sample 15
3687.9 3688 3688.1 3688.2 3688.3 3688.4 3688.5 3688.6 3688.7
Downcore Depth [m]

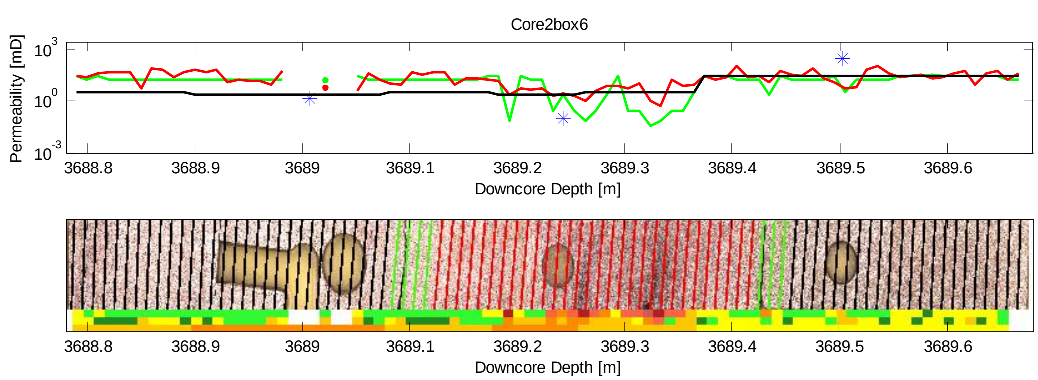
Core2box6
Permeability [mD]
10^3
10^0
10^{-3}
3688.8 3688.9 3689 3689.1 3689.2 3689.3 3689.4 3689.5 3689.6
Downcore Depth [m]
3688.8 3688.9 3689 3689.1 3689.2 3689.3 3689.4 3689.5 3689.6
Downcore Depth [m]

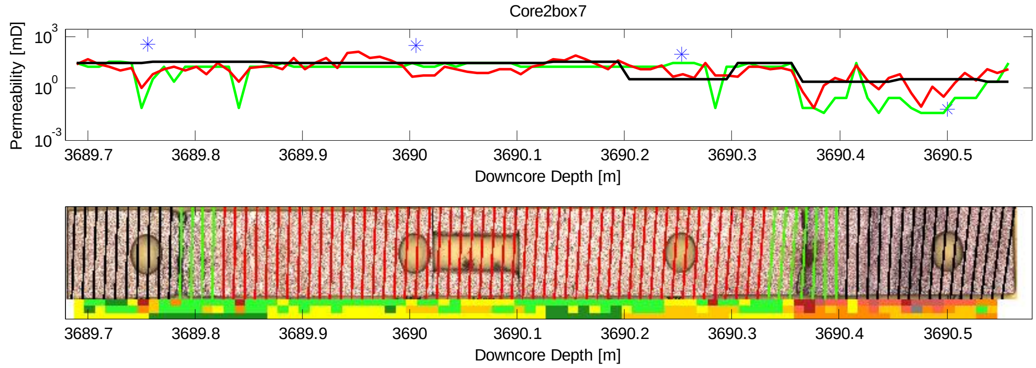
Core2box7
Permeability [mD]
10^3
10^0
10^{-3}
3689.7 3689.8 3689.9 3690 3690.1 3690.2 3690.3 3690.4 3690.5
Downcore Depth [m]
3689.7 3689.8 3689.9 3690 3690.1 3690.2 3690.3 3690.4 3690.5
Downcore Depth [m]

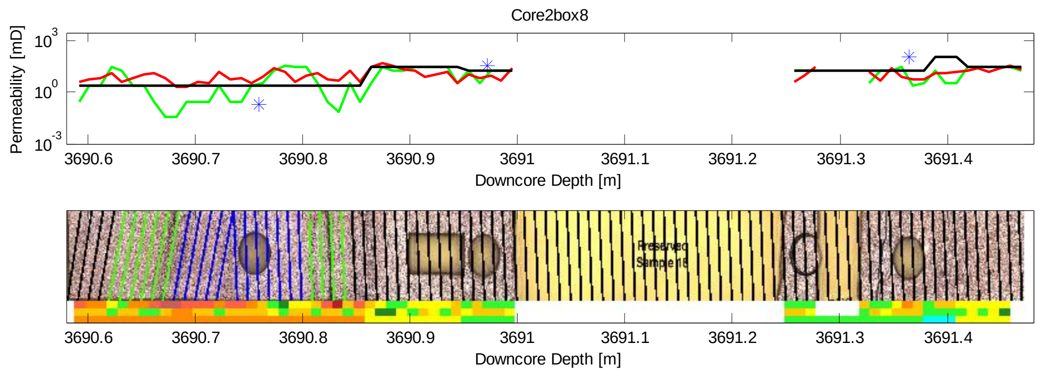
Core2box8
Permeability [mD]
10^3
10^0
10^{-3}
3690.6 3690.7 3690.8 3690.9 3691 3691.1 3691.2 3691.3 3691.4
Downcore Depth [m]
3690.6 3690.7 3690.8 3690.9 3691 3691.1 3691.2 3691.3 3691.4
Downcore Depth [m]

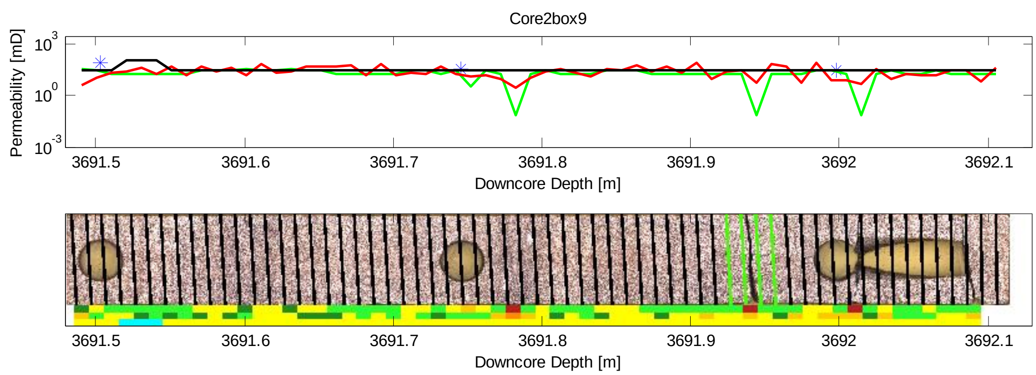
Core2box9
Permeability [mD]
10^3
10^0
10^{-3}
3691.5 3691.6 3691.7 3691.8 3691.9 3692 3692.1
Downcore Depth [m]
3691.5 3691.6 3691.7 3691.8 3691.9 3692 3692.1
Downcore Depth [m]

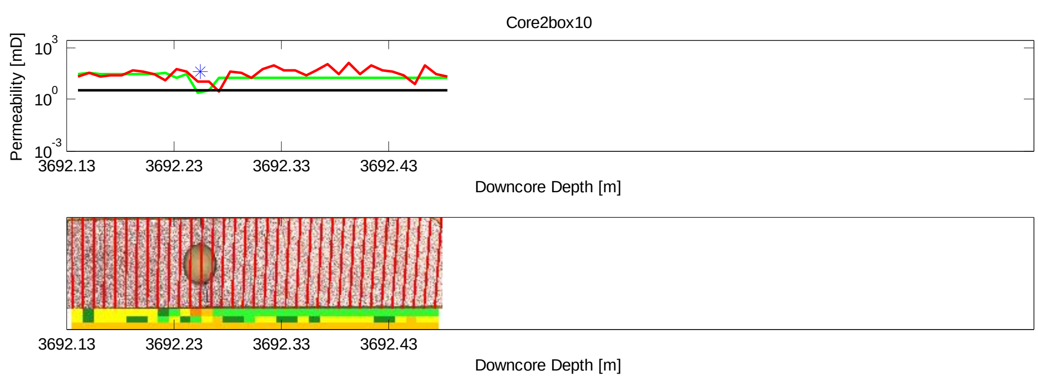
Core2box10
Permeability [mD]
10^3
10^0
10^{-3}
3692.13 3692.23 3692.33 3692.43
Downcore Depth [m]
3692.13 3692.23 3692.33 3692.43
Downcore Depth [m]

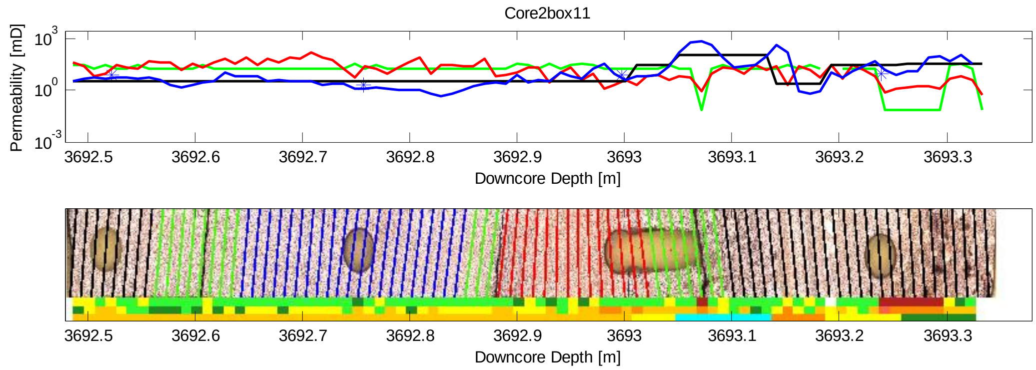
Core2box11
Permeability [mD]
10^3
10^0
10^-3
3692.5 3692.6 3692.7 3692.8 3692.9 3693 3693.1 3693.2 3693.3
Downcore Depth [m]
3692.5 3692.6 3692.7 3692.8 3692.9 3693 3693.1 3693.2 3693.3
Downcore Depth [m]

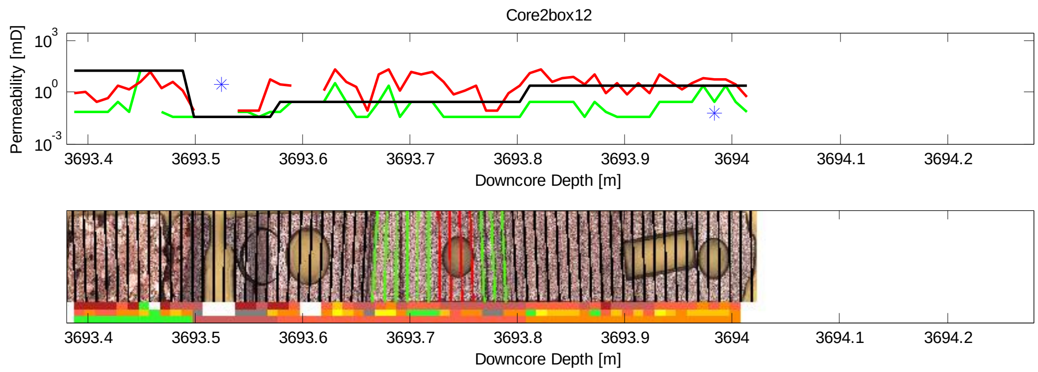
Core2box12
Permeability [mD]
10^3
10^0
10^-3
3693.4 3693.5 3693.6 3693.7 3693.8 3693.9 3694 3694.1 3694.2
Downcore Depth [m]
3693.4 3693.5 3693.6 3693.7 3693.8 3693.9 3694 3694.1 3694.2
Downcore Depth [m]

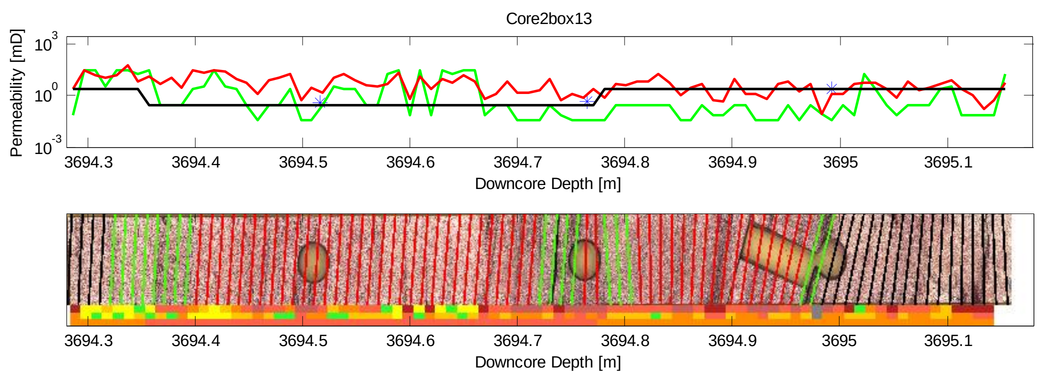
Core2box13
Permeability [mD]
10^3
10^0
10^-3
3694.3 3694.4 3694.5 3694.6 3694.7 3694.8 3694.9 3695 3695.1
Downcore Depth [m]
3694.3 3694.4 3694.5 3694.6 3694.7 3694.8 3694.9 3695 3695.1
Downcore Depth [m]

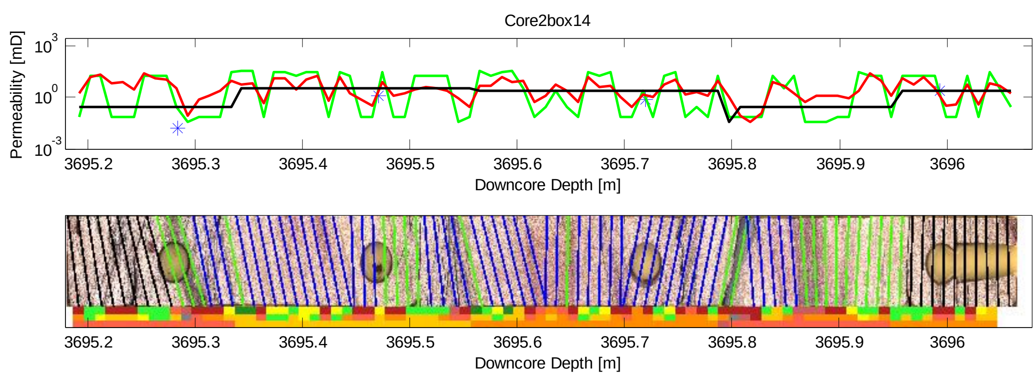
Core2box14
Permeability [mD]
10^3
10^0
10^-3
3695.2 3695.3 3695.4 3695.5 3695.6 3695.7 3695.8 3695.9 3696
Downcore Depth [m]
3695.2 3695.3 3695.4 3695.5 3695.6 3695.7 3695.8 3695.9 3696
Downcore Depth [m]

Core2box15

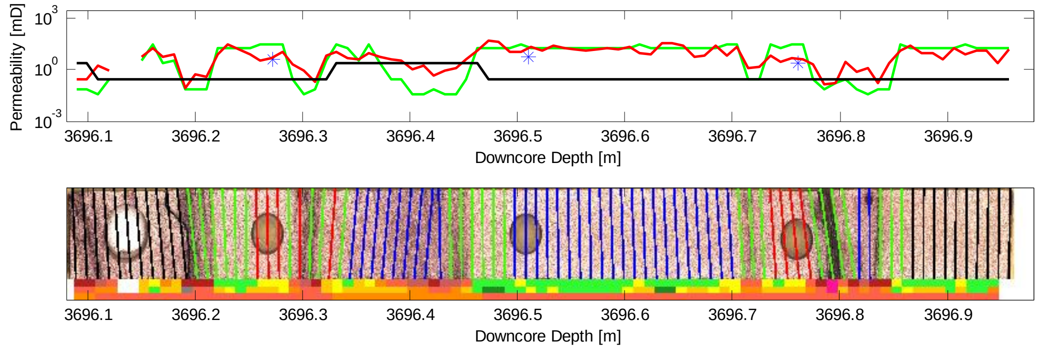

Core2box16

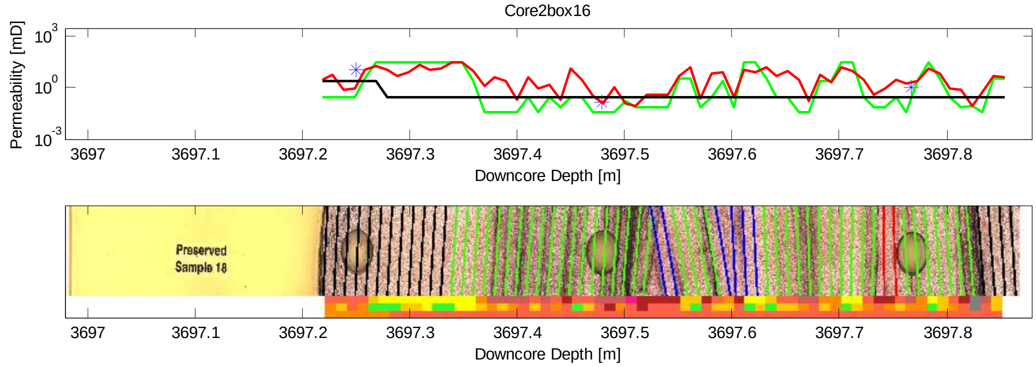

Core2box17

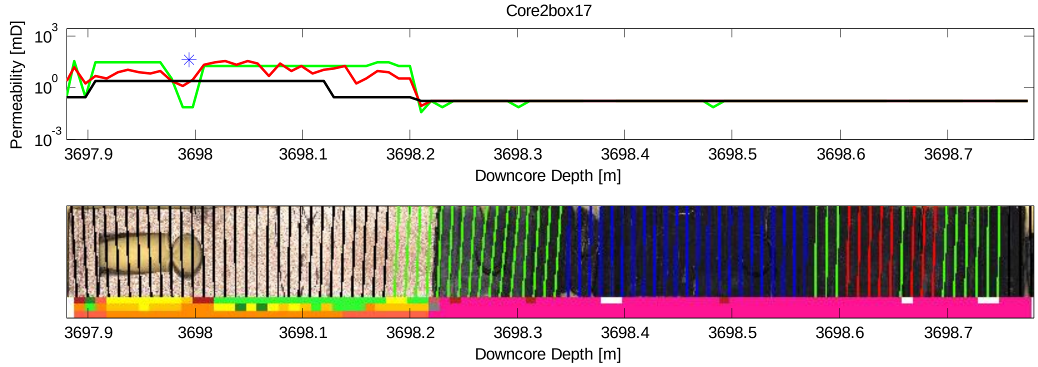

Core2box18

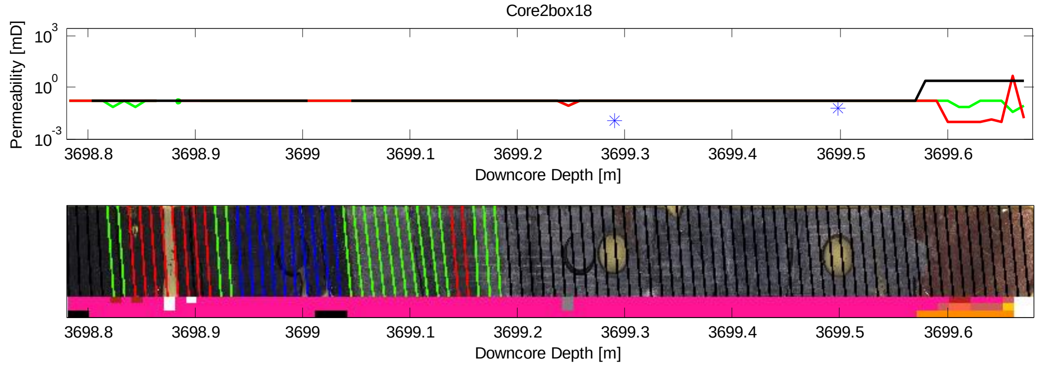

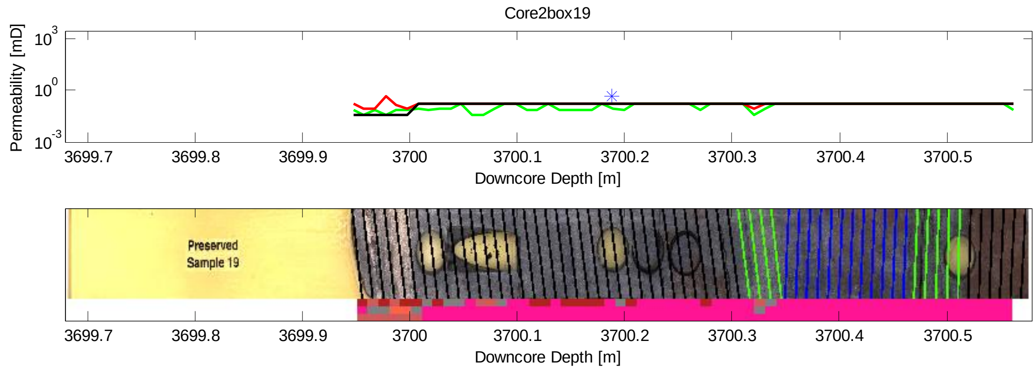
Core2box19
Permeability [mD]
10^3
10^0
10^{-3}
3699.7 3699.8 3699.9 3700 3700.1 3700.2 3700.3 3700.4 3700.5
Downcore Depth [m]
Preserved
Sample 19
3699.7 3699.8 3699.9 3700 3700.1 3700.2 3700.3 3700.4 3700.5
Downcore Depth [m]

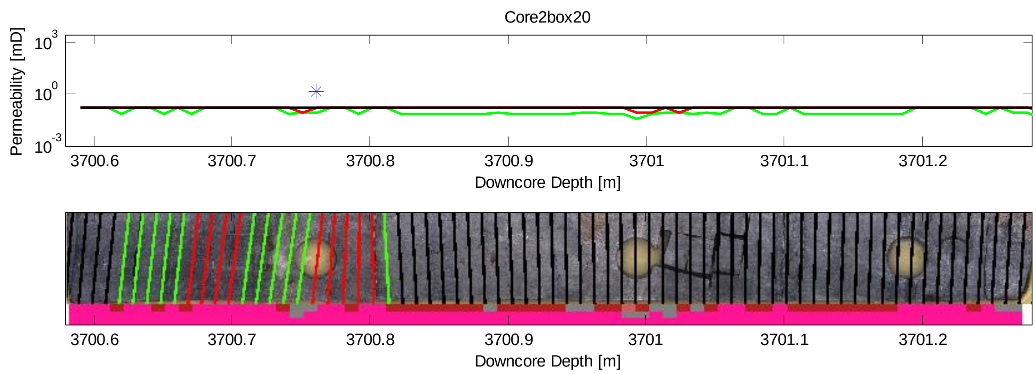
Core2box20
Permeability [mD]
10^3
10^0
10^{-3}
3700.6 3700.7 3700.8 3700.9 3701 3701.1 3701.2
Downcore Depth [m]
3700.6 3700.7 3700.8 3700.9 3701 3701.1 3701.2
Downcore Depth [m]

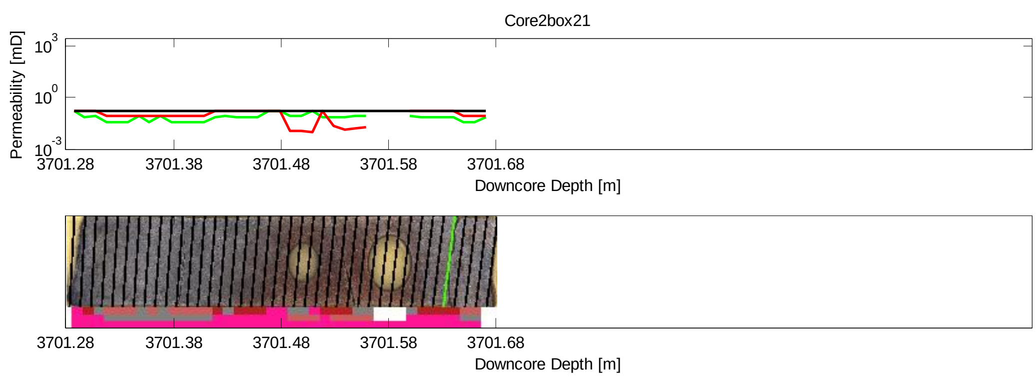
Core2box21
Permeability [mD]
10^3
10^0
10^{-3}
3701.28 3701.38 3701.48 3701.58 3701.68
Downcore Depth [m]
3701.28 3701.38 3701.48 3701.58 3701.68
Downcore Depth [m]

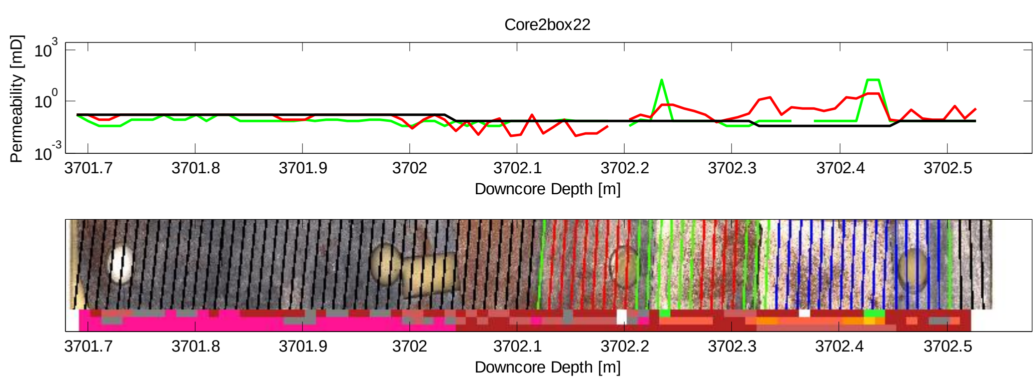
Core2box22
Permeability [mD]
10^3
10^0
10^{-3}
3701.7 3701.8 3701.9 3702 3702.1 3702.2 3702.3 3702.4 3702.5
Downcore Depth [m]
3701.7 3701.8 3701.9 3702 3702.1 3702.2 3702.3 3702.4 3702.5
Downcore Depth [m]

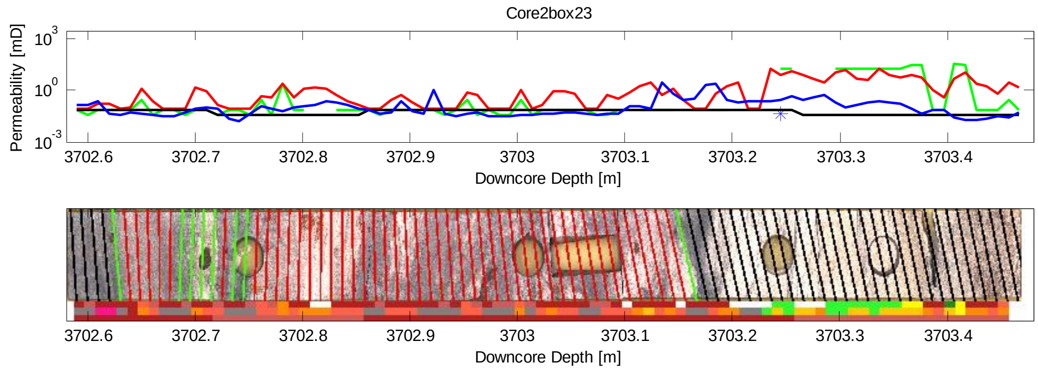
Core2box23
Permeability [mD]
10^3
10^0
10^-3
3702.6 3702.7 3702.8 3702.9 3703 3703.1 3703.2 3703.3 3703.4
Downcore Depth [m]
3702.6 3702.7 3702.8 3702.9 3703 3703.1 3703.2 3703.3 3703.4
Downcore Depth [m]

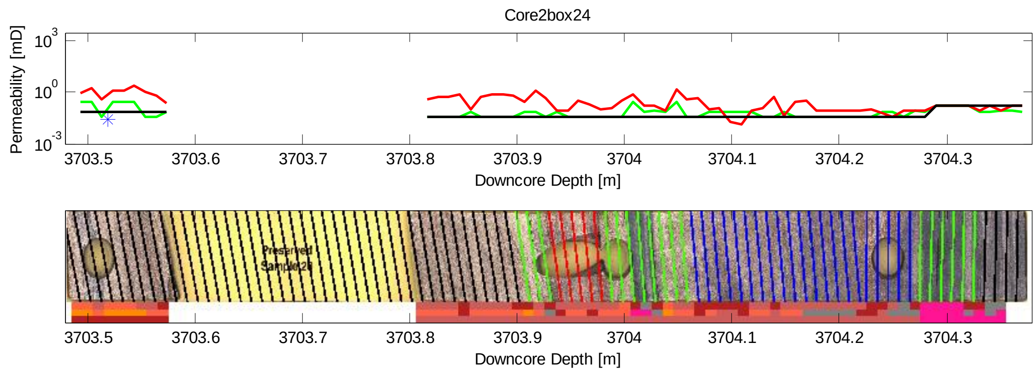
Core2box24
Permeability [mD]
10^3
10^0
10^-3
3703.5 3703.6 3703.7 3703.8 3703.9 3704 3704.1 3704.2 3704.3
Downcore Depth [m]
3703.5 3703.6 3703.7 3703.8 3703.9 3704 3704.1 3704.2 3704.3
Downcore Depth [m]

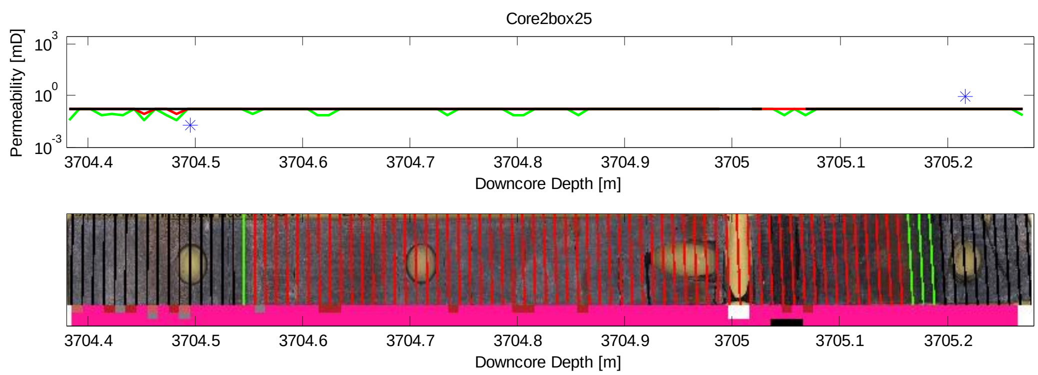
Core2box25
Permeability [mD]
10^3
10^0
10^-3
3704.4 3704.5 3704.6 3704.7 3704.8 3704.9 3705 3705.1 3705.2
Downcore Depth [m]
3704.4 3704.5 3704.6 3704.7 3704.8 3704.9 3705 3705.1 3705.2
Downcore Depth [m]

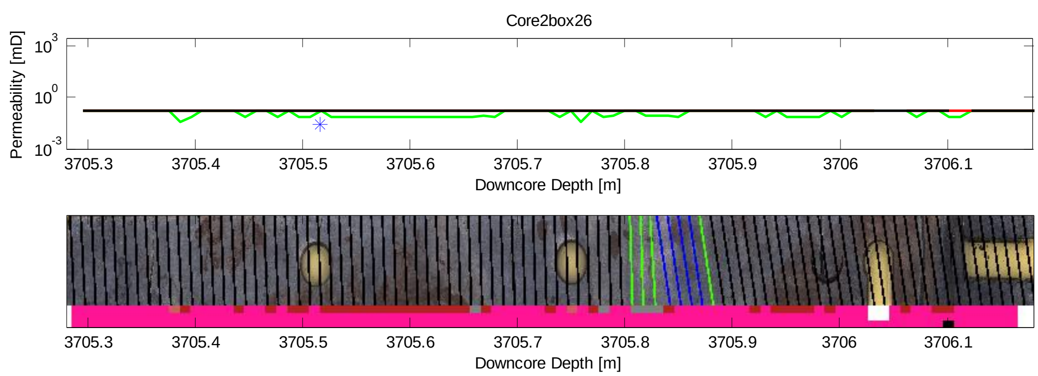
Core2box26
Permeability [mD]
10^3
10^0
10^-3
3705.3 3705.4 3705.5 3705.6 3705.7 3705.8 3705.9 3706 3706.1
Downcore Depth [m]
3705.3 3705.4 3705.5 3705.6 3705.7 3705.8 3705.9 3706 3706.1
Downcore Depth [m]

Core2box27

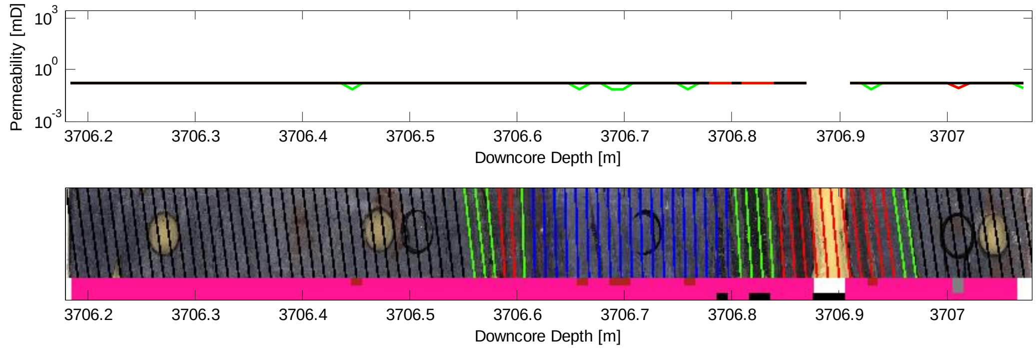

Core2box28

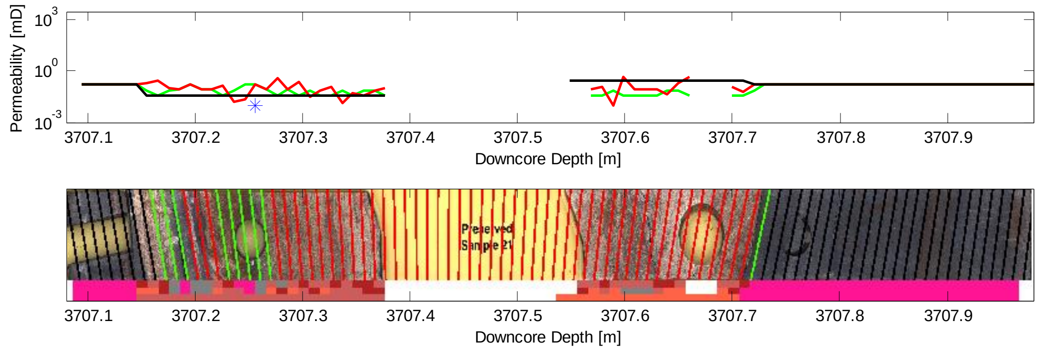

Core2box29

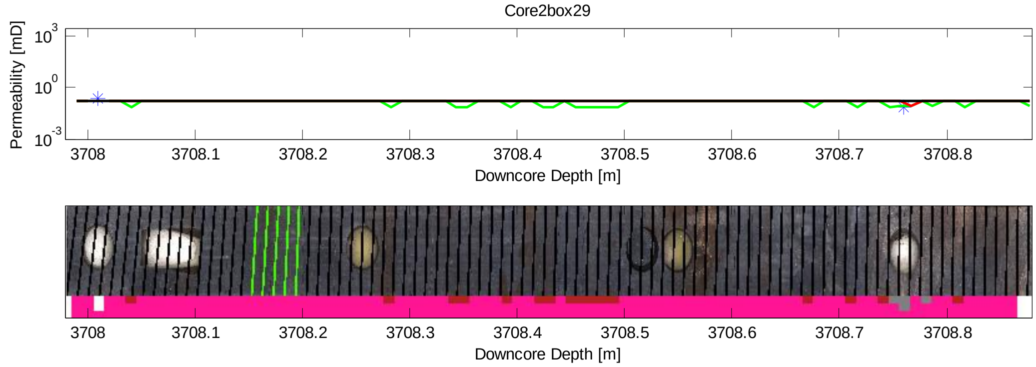

Core2box30

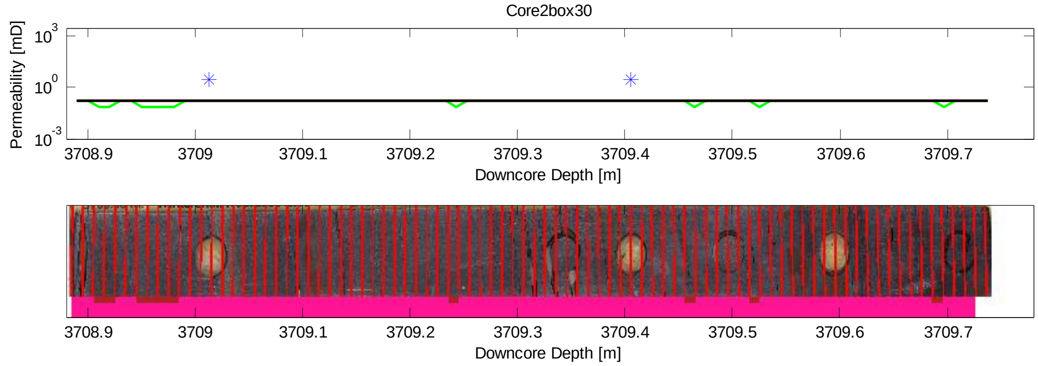

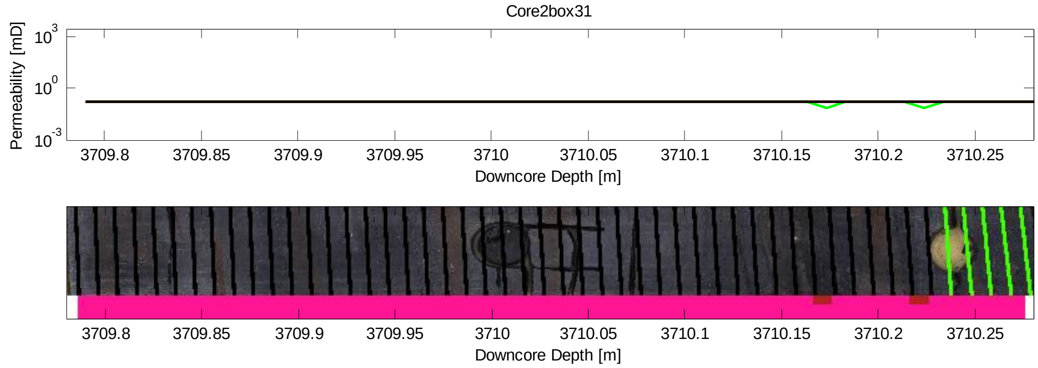
Core2box31
Permeability [mD]
10^3
10^0
10^{-3}
3709.8 3709.85 3709.9 3709.95 3710 3710.05 3710.1 3710.15 3710.2 3710.25
Downcore Depth [m]
3709.8 3709.85 3709.9 3709.95 3710 3710.05 3710.1 3710.15 3710.2 3710.25
Downcore Depth [m]

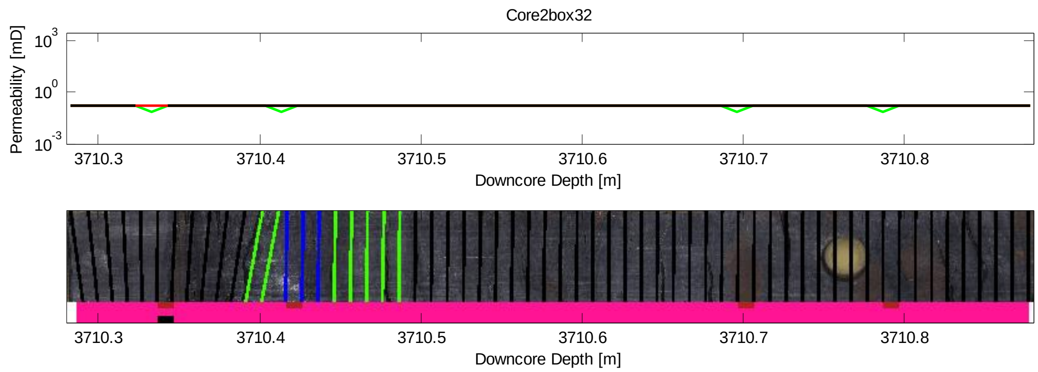
Core2box32
Permeability [mD]
10^3
10^0
10^{-3}
3710.3 3710.4 3710.5 3710.6 3710.7 3710.8
Downcore Depth [m]
3710.3 3710.4 3710.5 3710.6 3710.7 3710.8
Downcore Depth [m]

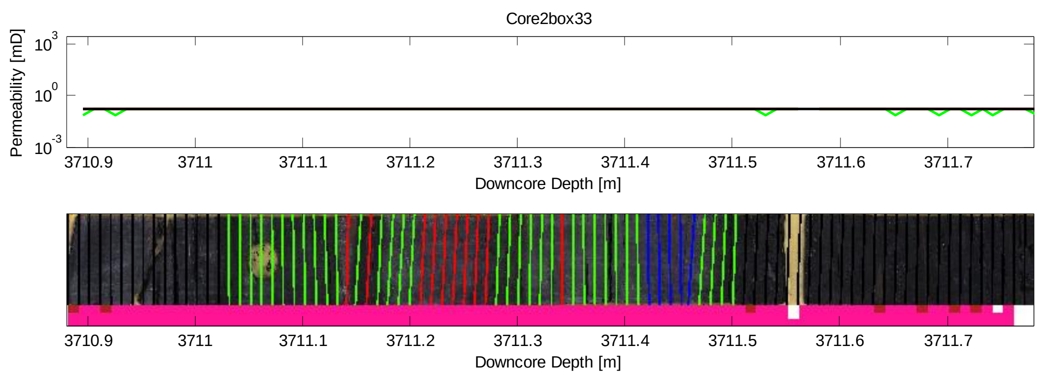
Core2box33
Permeability [mD]
10^3
10^0
10^{-3}
3710.9 3711 3711.1 3711.2 3711.3 3711.4 3711.5 3711.6 3711.7
Downcore Depth [m]
3710.9 3711 3711.1 3711.2 3711.3 3711.4 3711.5 3711.6 3711.7
Downcore Depth [m]

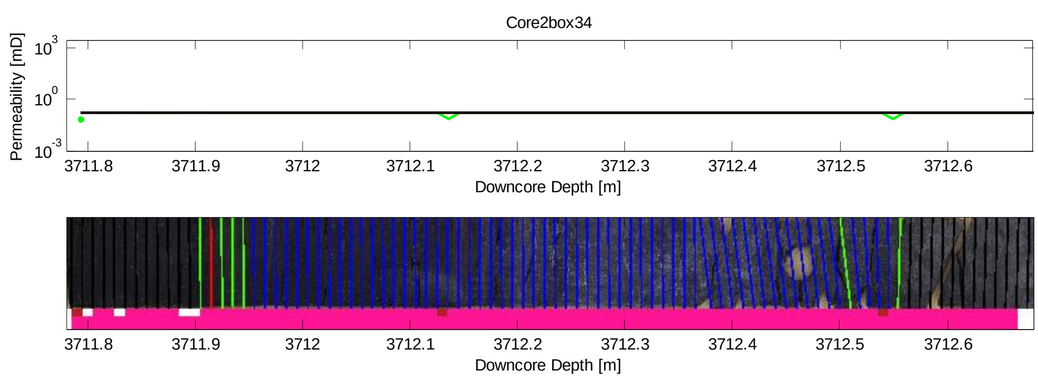
Core2box34
Permeability [mD]
10^3
10^0
10^{-3}
3711.8 3711.9 3712 3712.1 3712.2 3712.3 3712.4 3712.5 3712.6
Downcore Depth [m]
3711.8 3711.9 3712 3712.1 3712.2 3712.3 3712.4 3712.5 3712.6
Downcore Depth [m]

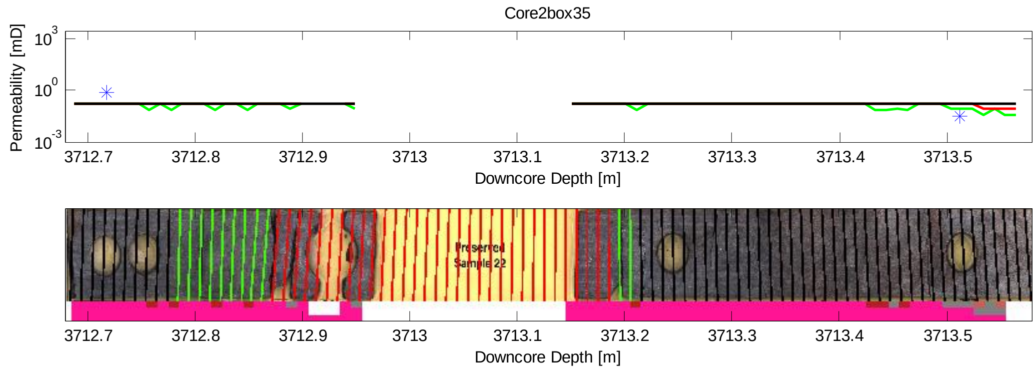
Core2box35
Permeability [mD]
10^3
10^0
10^-3
3712.7 3712.8 3712.9 3713 3713.1 3713.2 3713.3 3713.4 3713.5
Downcore Depth [m]
Preserved
Sample 22
3712.7 3712.8 3712.9 3713 3713.1 3713.2 3713.3 3713.4 3713.5
Downcore Depth [m]

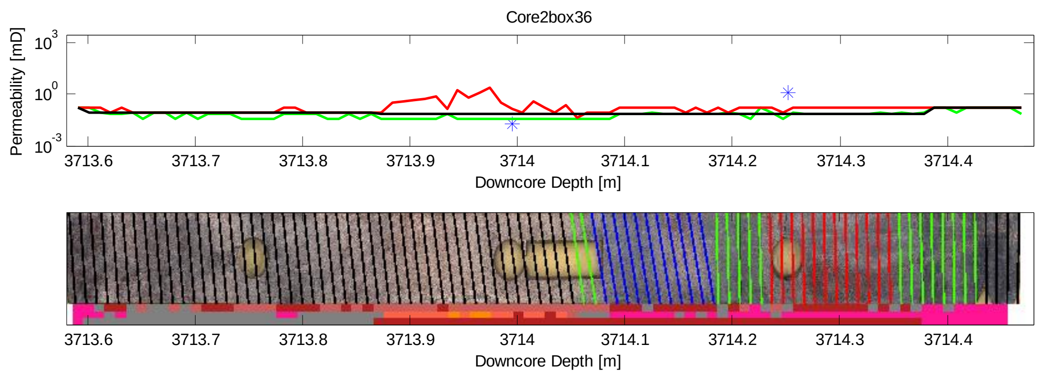
Core2box36
Permeability [mD]
10^3
10^0
10^-3
3713.6 3713.7 3713.8 3713.9 3714 3714.1 3714.2 3714.3 3714.4
Downcore Depth [m]
3713.6 3713.7 3713.8 3713.9 3714 3714.1 3714.2 3714.3 3714.4
Downcore Depth [m]

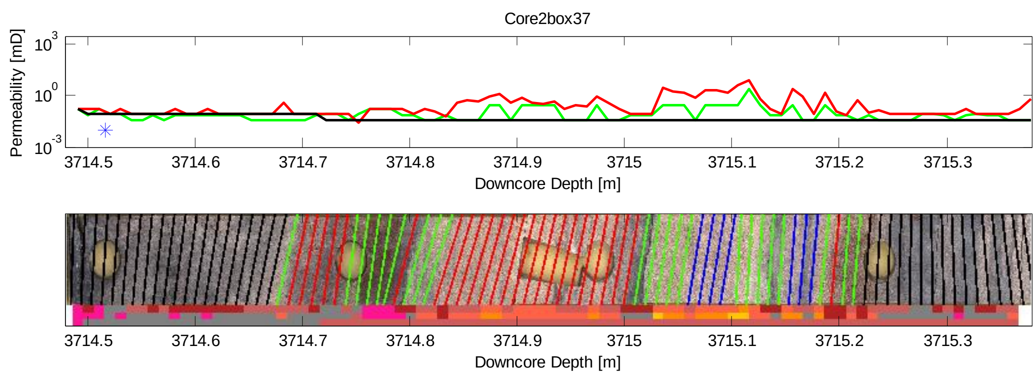
Core2box37
Permeability [mD]
10^3
10^0
10^-3
3714.5 3714.6 3714.7 3714.8 3714.9 3715 3715.1 3715.2 3715.3
Downcore Depth [m]
3714.5 3714.6 3714.7 3714.8 3714.9 3715 3715.1 3715.2 3715.3
Downcore Depth [m]

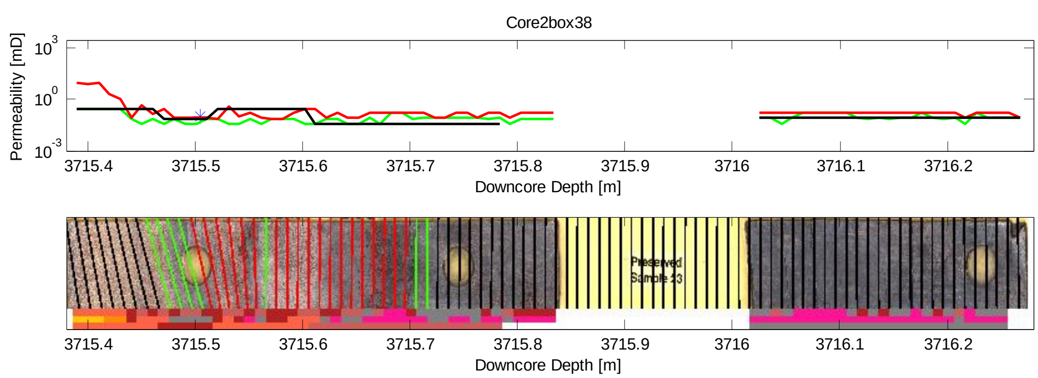
Core2box38
Permeability [mD]
10^3
10^0
10^-3
3715.4 3715.5 3715.6 3715.7 3715.8 3715.9 3716 3716.1 3716.2
Downcore Depth [m]
Preserved
Sample 23
3715.4 3715.5 3715.6 3715.7 3715.8 3715.9 3716 3716.1 3716.2
Downcore Depth [m]

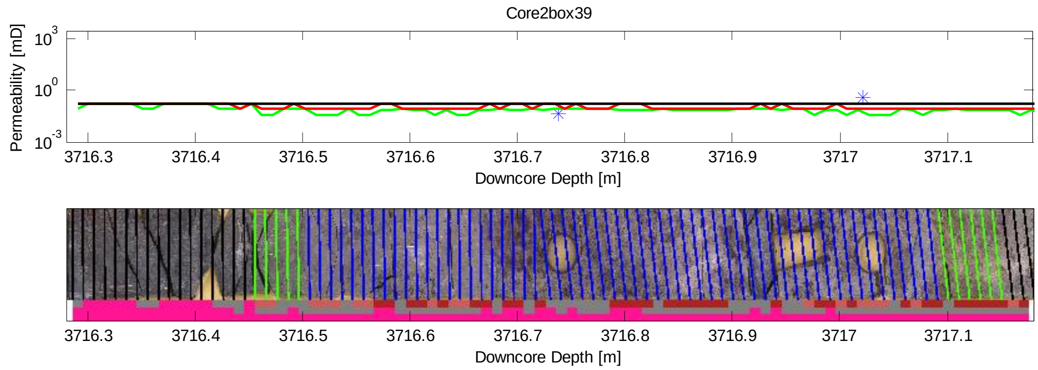
Core2box39
Permeability [mD]
10^3
10^0
10^-3
3716.3
3716.4
3716.5
3716.6
3716.7
3716.8
3716.9
3717
3717.1
Downcore Depth [m]

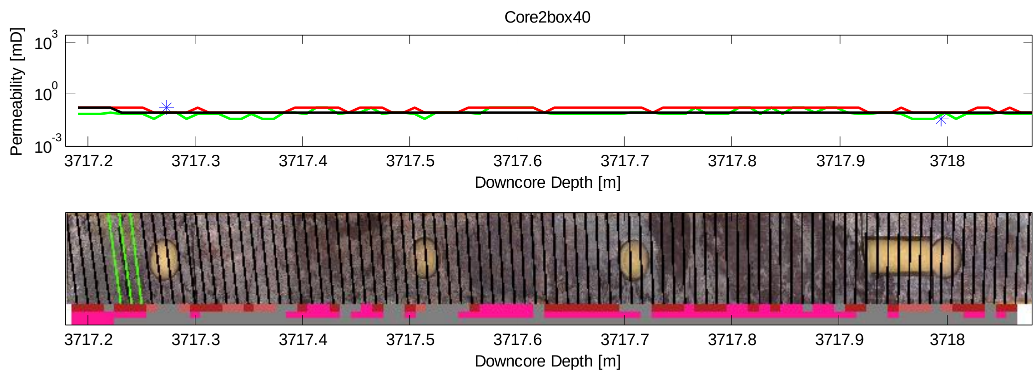
Core2box40
Permeability [mD]
10^3
10^0
10^-3
3717.2
3717.3
3717.4
3717.5
3717.6
3717.7
3717.8
3717.9
3718
Downcore Depth [m]

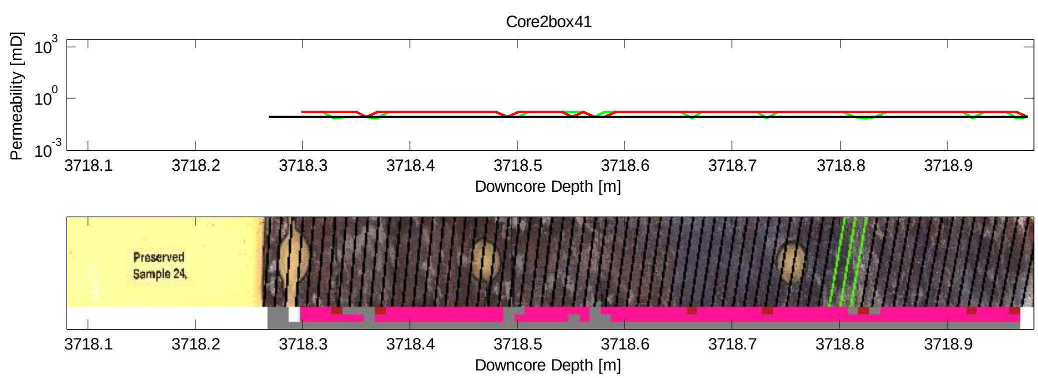
Core2box41
Permeability [mD]
10^3
10^0
10^-3
3718.1
3718.2
3718.3
3718.4
3718.5
3718.6
3718.7
3718.8
3718.9
Downcore Depth [m]
Preserved
Sample 24,

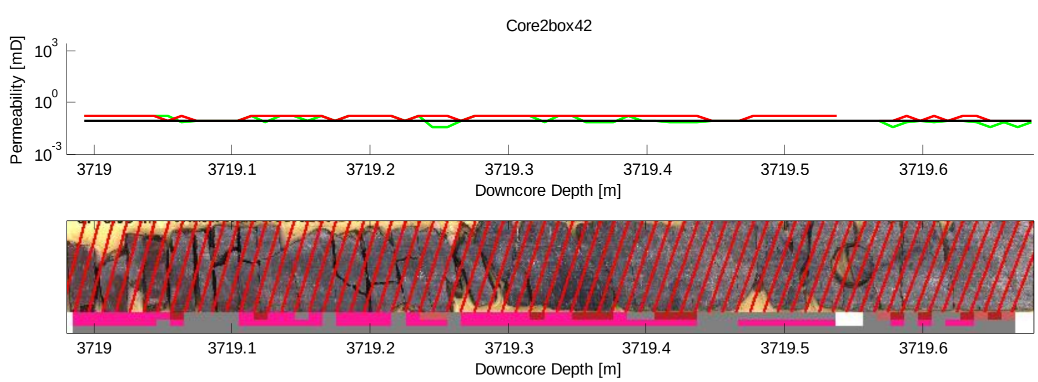
Core2box42
Permeability [mD]
10^3
10^0
10^-3
3719
3719.1
3719.2
3719.3
3719.4
3719.5
3719.6
Downcore Depth [m]

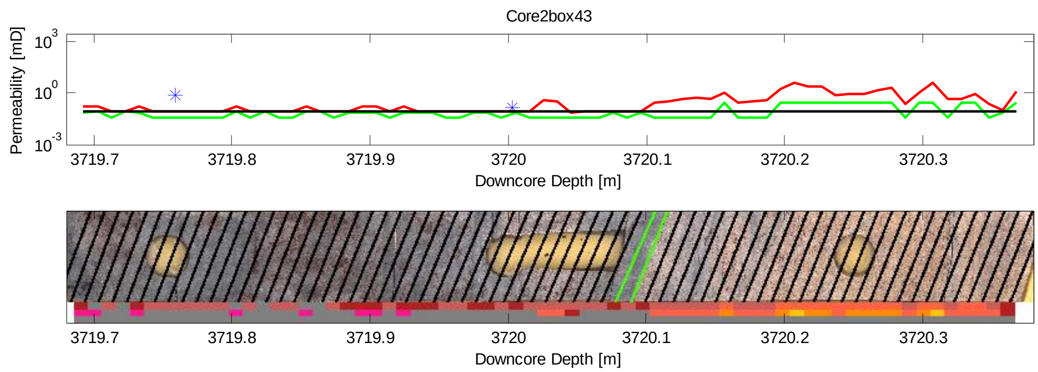
Core2box43
Permeability [mD]
10^3
10^0
10^{-3}
3719.7
3719.8
3719.9
3720
3720.1
3720.2
3720.3
Downcore Depth [m]
3719.7
3719.8
3719.9
3720
3720.1
3720.2
3720.3
Downcore Depth [m]

Appendix C

This appendix describes the different lithofacies present in the core, as identified in the core report of Core E10-3 (Boels, 2003).

Braided channel complex (BC3)

Roughly 55% of the cores from Well E10-3 consists of the braided channel lithofacies association, making it the dominant lithofacies association. The grain size of the sandstones is mainly upper fine to medium sand but varies from pebbles- to silt-sized sand. The sedimentary structures observed within the beds comprise alternations of massive, high-angle cross-bedding, low-angle cross-bedding, tangential cross-bedding, horizontal lamination, and ripple lamination.

The sandstones of the braided channel lithofacies association are interpreted as the bed load deposits of a high-energy braided channel complex system. The large continuous sandbody thickness, the general absence of a clear grain size trend, the abundance of tangential and low-angle cross lamination, and the coarse-grained internal erosive reactivation surfaces all suggest that these units make up deposits from high-energy braided streams.

Crevasse splay (CS)

About 11% of the cored interval was assigned to the Crevasse Splay deposits. The lithofacies association consists of parallel, low-angle, and ripple laminated very fine grained sandstone beds with moderate amounts of carbonaceous matter and clay (5-35%) occurring as intraclasts and laminations. Also, these deposits are moderately often rootletted at the top. The average bed thickness is 0.89 m. This association commonly marks the transition of IB (interdistributary bay) to IFL (poorly drained floodplain) facies associations. These deposits were interpreted as crevasse splay deposits on basis of the fine-grained nature of the sandstone beds, the relatively thin bed thickness, the clay occurring as laminae and the occurrence within floodplain sediments (IFL and IB, see below). These deposits formed on the floodplain as the result of a breaching of channel margins during high water discharge. The rootletting in the upper part of the deposits would imply an abrupt cessation of sediment deposition allowing development of vegetation on the sediment surface.

Poorly drained floodplain (IFL)

Poorly drained Floodplain deposits (IFL) comprise nearly 18% of the cored interval. The association consists of dark grey to black, abundantly rootletted claystones with regular coal laminae, frequent siderite nodules, and comon preserved organic matter. The poorly drained floodplain contains abundant intercalations of swamp (SW) and crevasse splay (CS) deposits. The poorly drained floodplain is recognized as such by the dark grey colour, the abundant rootletting and good preservation of organic matter. This all indicates a waterlogged or slightly submerged, reducing environment with intense plant growth. Being a lateral equivalent of the braided channel sandstones, the dominance of clay-sized deposits implies a setting distal to the active distributary.

Interdistributary bay deposits (IB)

Nearly 12% of the cored interval consists of Interdistributary Bay deposits. The association consists of dark grey, relatively undisturbed laminated claystones with a few silt or sand laminae. Some beds have a yellowish coloration due to siderite cementation. Distortion through soft sediment deformation occurs sporadically. The transition from IB (Interdistributary bay) to IFL (poorly drained floodplain) lithofacies association in the cored interval systematically occurs through CS lithofacies association (crevasse splay).

The well-preserved parallel lamination of the claystones, and the absence of rootletting imply deposition within a permanently standing body of water, hence the deposits classify as Interdistributary bay deposits. The upward transition from Interdistributary Bay to Poorly drained Floodplain deposits through Crevasse Splays is considered to reflect the progradation of fluvial facies.

Swamp (SW)

Swamps comprise a small percentage of the cored interval (ca. 3parallel laminated organic rich claystones with cm-thick coal laminae. The coal beds, and the abundance of organic material suggest a waterlogged, anoxic environment with abundant floral inhabitance and no clastic input. Hence, these deposits are classified as Swamp (SW).

Well drained Floodplain (F)

3% of the cored interval consists Well-drained Floodplain, which only occurs in the lowermost section of core 2. It consists of thoroughly rootletted sandy claystones with a mottled appearance and an overall reddish coloration. Dark fragments occur which may represent the former host sediments give the rock its brecciated appearance. These sediments are termed Well-drained Floodplain on basis of the following arguments. The strong disturbance of the sediment suggests slow sedimentation rates and pedogenesis. The primary red coloration indicated that at time of deposition the ground water table was periodically below the sediment surface at the time of deposition. For example, the environment could have been subject to seasonal flooding.

Appendix D

This appendix shows an overview of all plugs in core E10-3 for which data in terms of Hassler sleeve plug permeability or Helium porosity was available.

Plug Number	Horizontal Permeability [mD]	Helium Porosity [%]	Grain Size Group
1	333.2853	15.800	S3l
2	331.1913	16.400	S2u
3	306.4608	16.000	S3l
4	10.1194	8.900	S3l
5	0.1998	8.800	S2u
6	14.9903	13.800	S2u
7	8.4585	15.100	S2u
8	1.0356	11.600	S2u
9	3.5713	14.700	S3l
10	3.5957	15.100	S2u
11	5.0557	16.000	S2u
12	3.6134	14.700	S2l
13	1.0247	12.600	S3u
15	5.9837	14.000	S2u
16	2.2676	13.300	S3l
17	0.3925	12.100	S2u
18	14.6475	18.000	S2u
20	1.6276	13.600	S3l
21	0.7262	12.100	S2u
22	0.2690	11.000	S2u
24	0.0057	0.400	S1u
25	0.3116	18.600	S3l
26	0.0625	10.500	S2l
27	0.1578	11.800	S3l
28	0.2697	11.100	S3l
29	0.7757	12.900	S2u
30	0.1368	12.000	S3l
31	0.2858	12.400	S3l
32	0.0433	10.900	S2l
33	0.0399	9.000	S1l
35	0.0069	3.000	M
36	0.7638	0.800	M
37	0.0128	0.800	M
38	0.0225	0.500	M
39	0.1415	0.200	M
41	0.0104	0.200	M
42	0.0082	5.500	M
43	0.0691	4.100	M
44	0.0161	9.400	S1u
45	< 0.01	3.800	S1u

Plug Number	Horizontal Permeability [mD]	Helium Porosity [%]	Grain Size Group
46	0.0108	5.600	S1u
48	< 0.01	1.000	S1l
49	< 0.01	0.300	M
51	< 0.01	0.200	M
52	2.4718	0.600	M
53		1.400	M
54		0.900	M
55		3.500	M
58	2.2516	0.300	M
59	< 0.01	0.700	J
60	< 0.01	1.200	J
61	0.0065	0.500	M
62	< 0.01	0.500	M
63	0.1248	1.700	M
64	0.0111	4.400	S1u
65	0.0193	4.800	S1u
67	<0.01	0.900	M
68	0.0925	0.700	M
69	1.1492	0.800	M
71	0.0152	0.300	M
72	0.1668	0.700	M
73	0.4794	0.400	M
74	0.1194	0.800	M
75	0.0653	2.700	J
76	0.0068	5.000	J
77	0.0391	9.600	S1u
78	<0.01	7.800	S1u
80	0.0162	7.600	S1u
81	0.0264	7.300	S1u
82	0.0913	11.300	S2l
83	0.0098	7.500	S2l
84	1.8204	16.100	S2l
85	0.2478	13.400	S1u
86	0.4409	14.500	S1u
87	0.1780	12.400	S1u
88	0.0961	10.800	S1u
89	0.1738	9.400	S3l
91	87.8195	18.400	S3u
92	103.8256	18.300	S3u
93	9.4795	14.400	S3u
94	1.5318	15.600	S3l
95	0.9953	11.900	S2u
96	5.5545	14.200	S3u
97	14.1054	14.600	S3l
98	1.6761	12.600	S3l

Plug Number	Horizontal Permeability [mD]	Helium Porosity [%]	Grain Size Group
99	2.8268	13.100	S3l
100	2.8945	13.200	S2u
101	1.0568	12.400	S3l
103	22.2599	16.500	S3l
104	7.5900	15.500	S2u
105	1.8805	10.500	S2u
106	8.8085	15.800	S2u
107	17.5404	15.600	S3l
108	0.4391	11.400	S2u
109	12.7625	15.800	S2u
110	5.7999	14.400	S2u
111	14.6097	15.900	S3u
112	48.8576	18.900	S3l
113	33.3786	16.800	S3l
114	26.4988	16.300	S3u
115	34.7398	18.900	S2u
117	10.3746	14.100	S3u
118	86.9825	18.900	S3l
119	18.0572	14.100	S3l
120	72.1058	18.200	S2l
121	6.7800	14.000	S3l
122	74.3761	16.200	S4l
123	50.2922	17.000	S2u
124	200.4643	18.500	S3u
125	4.4805	14.600	S4l
126	3.4223	14.400	S3u
128	0.0534	0.600	S1l
129	<0.01	3.900	S1u
130	<0.01	0.900	S1u
131	<0.01	1.300	S1u
132	<0.01	6.100	S2l
133	0.0348	8.800	S2l
134	0.1495	6.200	S2l
135	<0.01	7.100	S2l
136	0.3575	10.000	S3l
137	0.6036	9.900	S3l
138	0.0099	12.000	S3u
140	0.0050	4.700	S2u
141	<0.01	3.700	S1u
142	0.3586	12.600	S2l
143	0.1116	10.500	S2l
144	0.5580	13.200	S2l
145	6.8632	17.400	S2l
146	0.0718	8.900	S2l
147	0.4312	12.800	S2l

Plug Number	Horizontal Permeability [mD]	Helium Porosity [%]	Grain Size Group
148	0.0100	6.800	S2l
149	0.0406	5.500	S2l
150	0.0452	9.400	S2l
151	213.3054	19.100	S3u
152	42.0644	17.900	S3l
153	8.6242	15.300	S3l
154	5.1793	14.300	S3u
155	260.4668	17.200	S3u
156	7.7969	14.900	S4u
157	145.8474	17.400	S3u
158	205.4561	19.400	S3u
159	0.0132	5.500	S3l
160	119.6625	17.000	S4l
163	0.0412	9.800	S2u
164	0.1495	9.100	S2u
165	1.5411	12.100	S2u
166	0.1077	8.000	S2u
167	319.4031	19.900	S3u
168	387.0145	20.800	S3u
169	329.5046	20.500	S3u
170	100.8067	19.800	S3l
171	0.0596	7.600	S3l
172	0.1974	9.200	S2u
173	37.0180	16.300	S4u
174	114.7761	18.300	S5l
175	79.9504	17.400	S3u
176	33.2885	15.800	S3u
177	29.8845	15.600	S3u
178	39.5202	15.700	S3l
179	7.6950	13.700	S3l
180	2.1750	11.100	S3l
181	7.3506	14.800	S3l
182	9.9306	13.800	S3u
183	0.0050	3.900	S1u
184	0.0619	9.700	S2l
185	2.6671	13.600	S2u
187	0.3638	10.700	S2l
188	0.4397	10.700	S2l
189	2.4775	13.600	S2u
190	0.0162	6.100	S2l
191	1.1731	13.200	S3l
192	0.7019	12.200	S2u
193	2.4023	12.500	S2u
194	4.3471	13.700	S2l
195	5.6955	14.000	S2l

Plug Number	Horizontal Permeability [mD]	Helium Porosity [%]	Grain Size Group
196	2.2787	11.800	S2l
198	11.2095	15.300	S2u
199	0.1400	10.200	S2l
200	1.0345	13.600	S2l
201	41.9423	17.800	S2u
206	0.0124	0.400	M
207	0.0632	0.400	M
209	0.0051	0.300	M
210	0.4695	0.500	M
211	0.0054	0.300	M
212	1.4796	0.300	M
213	< 0.01	1.800	M
214		0.800	M
215	< 0.01	0.100	M
216	< 0.01	0.100	M
217	< 0.01	0.500	M
218	< 0.01	1.300	S1l
219	< 0.01	3.800	S1l
220	< 0.01	1.500	S1u
221	< 0.01	2.900	S1l
222	0.0443	8.100	S1l
223	0.0271	3.500	S1l
225	< 0.01	1.500	S1u
226	< 0.01	1.200	S1u
227	0.0180	0.800	M
228	< 0.01	1.000	M
229	0.0051	0.700	M
230	0.8479	0.800	M
231	0.0280	0.600	M
232	< 0.01	0.400	M
233	< 0.01	0.400	M
234		0.600	M
235	< 0.01	0.400	M
237			M
238	0.0101	0.300	S1u
241	0.2293	0.100	M
242	< 0.01	0.100	M
243		0.200	M
244	0.0678	0.700	M
245	2.7780	0.600	M
246	3.0688	0.500	M
247	< 0.01	0.300	M
249	0.7633	0.500	M
250			M
252		0.700	M

Plug Number	Horizontal Permeability [mD]	Helium Porosity [%]	Grain Size Group
253		1.100	M
259		2.600	M
260	0.7022	0.400	M
262		0.400	M
263	0.0317	0.300	M
264	< 0.01	1.800	J
265	0.0197	5.800	S1l
266	1.2082	2.300	S1l
267	0.0100	1.300	J
268	< 0.01	1.200	S1u
269	< 0.01	3.600	S1u
270	< 0.01	3.400	S1u
271	0.1024	1.500	S1l
272	0.0052	0.500	S1u
274		0.400	J
276	0.0406	0.300	M
277	0.3976	0.400	M
278	0.1722	0.400	J
279	0.0051	0.200	J
280	< 0.01	0.100	J
281	0.0363	0.100	J
283		0.600	J
284		0.300	J
288	0.7511	0.400	J
289	0.1520	0.400	J
290	< 0.01	2.800	J

Appendix E

This appendix discusses the Pressure Decay Profile Permeameter, which is used to obtain independent high resolution permeability measurements of the core. These measurements are used as validation tool. Some specifics about CoreLab's PDPK-400 can be found in Table 20.

Pressure Decay Profile Permeameter workflow

The PDPK uses nitrogen as the working gas, because nitrogen is an inert gas that behaves relatively similar to an ideal gas. For this reason the equations used to calculate the pressure decay are simplified by making the correct assumptions. The gas storage tank is initially filled with nitrogen by opening a fill valve connected to a nitrogen source. The gas storage tank is connected to the probe by another valve, which is closed during the filling process.

When the tank has been filled, the probe is pressed against the sample with a set, non-destructive force (10 N) to ensure a good seal. When the nitrogen inside the storage tank reaches a set pressure (10 psi or 69 Kpa), the nitrogen supply is disconnected from the storage tank by closing the fill valve. Now the valve between the probe and the gas storage tank is opened, letting the nitrogen flow through the probe tip into the sample. Consequently the pressure will drop as nitrogen dissipates through the sample and the pressure decay in the gas storage tank is measured accurately. The Pressure Decay Profile Permeameter measures the pressure decay for 2 to 30 seconds, depending on the permeability of the sample and the user defined limits. After the measurement, the valve between the probe and the gas storage tank is closed and the device retracts the probe, starting the procedure from the beginning for a new measurement point.

Table 20; properties used for the measurements on the slabbed cores with the PDPK-400.

Constant	**Symbol**	**Value**	**Unit**
Inner tip radius	r_i	0.262	[cm]
Geometric Factor	$G_D\ r_i$	1.4	[cm]
Nozzle volume wrt to standard	ΔV_1	-0.0259	[cc]
Initial Pressure	P_{init}	10	[psi]

Pressure decay over time to permeability

The measured pressure decay over time can subsequently be converted to permeability by making some assumptions on the sample and flow geometry. These assumptions include the geometric factor of the probe and hemispherical flow conditions. The conversion of pressure decay to permeability has been described by *Jones (1994)* and a summary of this conversion is given in this section.

The probe tip of the PDPK is connected to the surface of the rock sample, the gas that flows through the probe tip is assumed to dissipate in a semi-hemispherical direction through the rock sample. Darcy's equation can be combined with the formula for hemispherical flow resulting in Equation 1.

$$k_g = \frac{29392 \cdot \mu_g(p_1 + P_a) \cdot q_1}{(2\pi \cdot r_i)p_1 \cdot (p_1 + 2p_a)}$$

Equation 1

This formula assumes that the probe seal has infinite size, in reality the seal has a finite size and beyond the outer radius of the probe r_o (probe seal radius) gas can curve upward and can escape through the surface of the sample. However, gas flow through any surface that is farther away than 4 times the inner probe radius (r_i) from the center of gas injection does not affect the calculation of the permeability appreciably. To account for different flow geometry, *Goggin et al (1988)* calculated a geometric factor G_D to replace the 2π in Equation 1. This geometric factor is calculated based on the factor of the inner and outer probe tip radii r_i and r_o. The results of this can be seen in Equation 2.

$$k_g = \frac{29392 \cdot \mu_g(p_1 + P_a) \cdot q_1}{(G_D \cdot r_i)p_1 \cdot (p_1 + 2p_a)}$$

Equation 2

Klinkenberg effect

Klinkenberg (1941) showed that the permeability measurements obtained with a gas as flowing fluid were dissimilar to permeability measurements with liquid. Klinkenberg describes this dissimilarity by the interaction of the fluids with the pore walls. At the pore surface, the liquid reaches a zero velocity, whereas gas exhibits some finite velocity at the pore surface. In other words: Gas shows a slippage effect at and near the boundaries of a pore, whereas liquids do not. To account for this difference a correction has to be made on the gas permeability to obtain the absolute permeability: The gas slippage correction. The Klinkenberg relation can be substituted into Equation 2 to obtain the slip corrected permeability (Equation 3).

$$k_\infty = \frac{29392 \cdot \mu_g(p_1 + P_a) \cdot q_1}{(G_D \cdot r_i)p_1 \cdot (p_1 + 2p_a + 2b_N)}$$

Equation 3

In this equation b is the Klinkenberg gas slippage factor.

Forchheimer flow correction

At low flow velocity, gas flowing through a porous medium obeys (a slip corrected) Darcy's Law, because the resistance is caused by viscous shear alone. At high flow velocities Darcy's Law underestimates the pressure gradient, because another resistance occurs: Inertial flow resistance. Energy dissipates due to the acceleration, deceleration and changes in direction of the flow through the pores and pore throats. This effect has been described by *Forchheimer (1901)*, and is today known as the Forchheimer flow correction. Probe Permeatry measurements are subjected to high gas velocities even when using a small pressure difference. This is the reason why a Forchheimer flow correction is necessary. When the Forchheimer flow correction is substituted into Equation 3, we obtain Equation 4.

$$\frac{P_{Gn} + 2P_a + 2b}{y_n} = \frac{29392 \cdot \mu_g}{(G_D \cdot r_i)p_1 \cdot k_\infty} + \frac{7.893 \cdot 10^{-10} \beta M}{T G_{F0}} \cdot \frac{p_{gn} y_n (p_{gn} + 2p_a + 2b_N)}{p_{gn} + 2p_a}$$

Equation 4

In this equation the subscript n refers to the nth point in a series of pressure/time measurements.

Appendix F

In this appendix a discussion of each of the methods used is given.

RGB to RGBD conversion

A fourth component can be extracted from the RGB data, namely the darkness. The darkness is a measure of lack of color. The darkness has similarities to the intensity of the color; the intensity of an image is the sum of the RGB components, whereas the darkness is the sum of the lack of color. This lack of color expresses itself as the maximum color minus the actual color. Each of the RGB components ranges from 0 to 255. A mathematical expression for the dark component of the color can be seen in Equation 5, from this equation it becomes clear that the darkness is a dependent variable.

$$\mathrm{D} = (255 - \mathrm{R}) + (255 - \mathrm{G}) + (255 - \mathrm{B})$$

Equation 5

Centered Log Ratio Transform

The Centered Log Ratio Transform is a technique used to represent (compositional) data by applying a standard log-ratio transformation. The result of the transform can be used in the same manner as the initial data, with the additional advantage of having a continuous interval where the distances scale correctly. This technique makes it easier to analyze data. Log transformed data can be transformed back to its original state by reversing the transformation. A mathematical representation of the Centered Log Ratio transform can be seen below in Equation 6.

$$clr(x) = z = [\log\left(\frac{\mathrm{x_i}}{\mathrm{g(x)}}\right); \ldots.; [\log\left(\frac{\mathrm{x_D}}{\mathrm{g(x)}}\right)]$$

Equation 6

With $g(x) = \sqrt[D]{x_1, \ldots..x_D}$

Correlation

Correlation is a statistical measure of dependence between two sets of variables; it is commonly represented by the Pearson's Product Moment Coefficient r_p. The Pearson Coefficient r_p is obtained by dividing the covariance of the two variables by the product of their standard deviations (Equation 7). The Pearson Coefficient thus is a linear measure of dependence between two sets of variables. An r_p (Pearson Coefficient) of 1 translates into a perfect correlation between the two variables. A Pearson Coefficient r_p of 0 translates into no correlation and a Pearson Coefficient r_p of -1 means a negative correlation between the two variables.

$$r_p = \frac{\sum_{i=1}^{n}(X_i - \bar{X})(Y_i - \bar{Y})}{\sqrt{\sum_{i=1}^{n}(X_i - \bar{X})^2}\sqrt{\sum_{i=1}^{n}(Y_i - \bar{Y})^2}}$$

Equation 7

In this equation the Pearson's Product Moment Coefficient of data set X and data set Y is obtained, where both datasets are comprised of n observations.

Principal Component Analysis

Principal Component Analysis (PCA) is a mathematical conversion of multivariate data that might contain correlations. PCA returns sets of values of linearly uncorrelated variables: The Principal Components. The first Principal Component (PC) is extracted by finding the direction where the variables show the most variance in an N-dimensional space (where N is the number of initial variables), the second Principal Component is extracted in the same manner, except for an extra limitation: it needs to be orthogonal (=uncorrelated) to the first Principal Component. The third Principal component needs to be orthogonal to the first two and so on.

To be able to extract the direction of highest variance, the PCA projects the initial variables in an N-dimensional space and for the first PC calculates the line where the sum of the distances from the line to each point is minimized.

Ultimately the PCA leads to a new coordinate system, where the first coordinate contains the most variance and gives the highest signal to noise ratio; the second coordinate is uncorrelated to the first and contains the second most variance and so on until the N-th Principal Component. The Nth principal component in a PCA on N variables where at least 2 variables are correlated contains a very small amount of information that is mainly a result of noise.

Auto-Covariance

Covariance is a measure of the strength of a correlation between two sets of data. If both data sets are uncorrelated the covariance between the two datasets will be zero, if the datasets are correlated and show a similar trend the covariance is a positive number. When the datasets are correlated, but show a negative trend, the covariance is negative. This is shown visually in Figure 53.

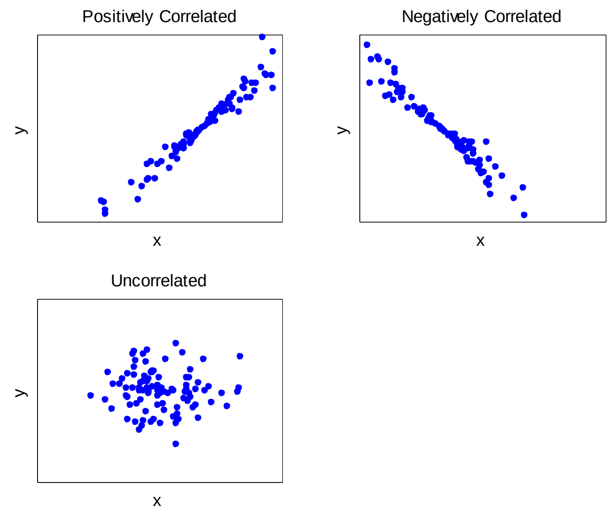

Figure 53: Example of different kinds of correlations between x and y.

The covariance between two jointly distributed real-valued random variables x and y with finite second moments is defined as shown in Equation 8.

$$\sigma_{xy} = E[\,(x - \mu_x)(y - \mu_y)$$

Equation 8

In Equation 8 μ_X and μ_Y are the expected value (or means) of x and y respectively. The Auto-Covariance of a dataset is the covariance of the dataset against a shifted version of itself. For each offset between the dataset and its shifted version, a covariance is calculated, resulting in a matrix of covariance values against offset. An example of an Auto-Covariance function can be seen in Figure 54.

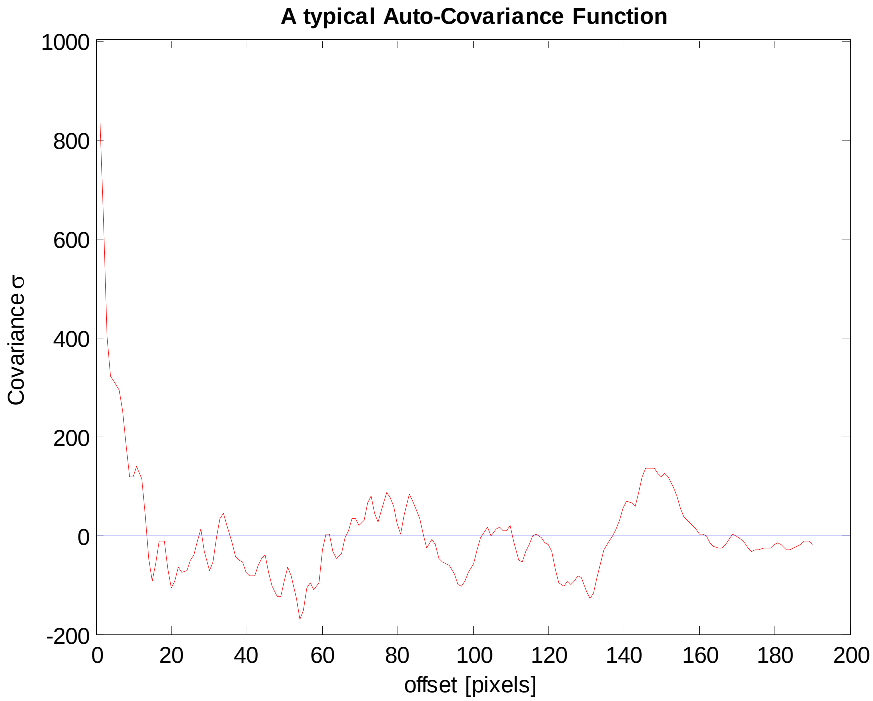

Figure 54: Auto-Covariance function

Clustering

Clustering is the task of grouping a set of objects in such a way that objects in the same group (called a cluster) are more similar (in some sense or another) to each other than to those in other groups. Clustering can be performed in a variety of ways, depending on the application. In this project K-means clustering is used. K-means clustering will cluster data into K clusters by minimizing the distance from each data point to a mean value of a cluster. This is an iterative process, where the mean value for each cluster is optimized and returned. The result of this is a partitioning of the data space into Voronoi cells (see Figure 55), where each cell is described by its mean. Boundaries between clusters are lines that are equidistant to closest means.

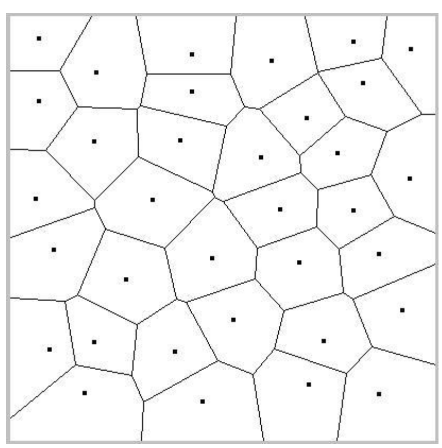

Figure 55: example of an area divided into Voronoi Cells, the result of K-means clustering. Source: www.cs.wustl.edu

Multivariate Gaussian Classification

Multivariate Gaussian distributions (see Figure 56 for an example) are the generalization of the one dimensional Gaussian distribution. Both distributions are used to describe a dataset that clusters around a mean value. In the case of a one-dimensional Gaussian distribution the spread of the data is described by a standard deviation. When considering a multivariate Gaussian distribution, the spread is described by a covariance matrix; this allows the distribution to describe a larger spread across one of its direction compared to the others. The probability density function in a one dimensional case is a simple bell curve, whereas in two-dimensions this is a 'hill' shaped surface, where each cross-section through the mean is a bell curve.

Each iso-density line of this two dimensional line is an ellipse, visible in Figure 56. Where an iso-density line is a line of points of which each point gives the same particular value of probability density. In a three dimensional space the iso-density surface is described by an ellipsoid. For example the density surface at 5 % probability will describe the volume of an ellipsoid in a three-dimensional space that includes 95 % of all data points.

When multivariate classification is used to classify data into a cluster, the probability of belonging to each multivariate Gaussian distribution is calculated and the distribution with the highest probability is assigned to the data point. To build a multivariate Gaussian classification model, a training set is needed around which the distribution is fitted. To fit a multivariate Gaussian distribution on a dataset, the decision was made to use the technique of minimum determinant covariance *(Rousseeuw, 1999)*. This technique is a robust way to fit a multivariate Gaussian distribution on a dataset, as it limits the effect of outliers by finding a covariance matrix for the distribution that has the smallest determinant when discarding a portion of the data. In other words, it finds the covariance matrix of a subset of the initial dataset for which the area of a (two-dimensional) Gaussian distribution is smallest. In more dimensions this will not be an area, but volume or a higher order volume, but the principle stays the same.

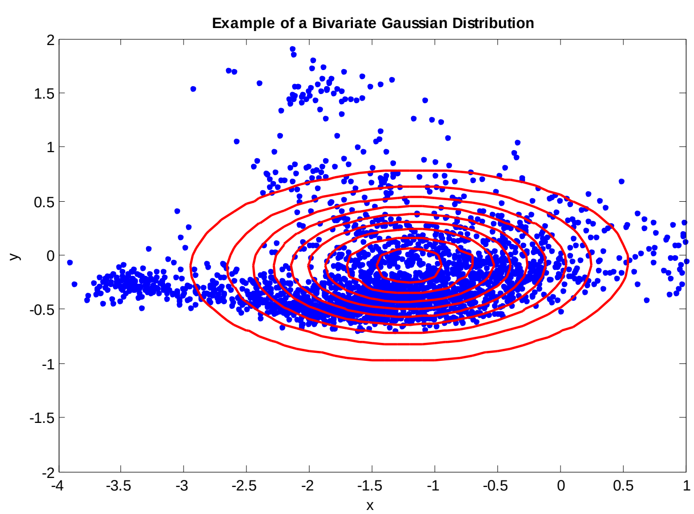

Figure 56: Plot of iso-density lines of a bivariate Gaussian distribution fitted on data points. Lines are plotted at a probability density of 10 % to 90 % in steps of 10%.

Classification based on a Quadratic Decision Boundary

A quadratic decision boundary is a method used in classification of a dataset in two classes. To distinguish between the two classes a multivariate Gaussian distribution is fitted on both datasets and the decision boundary between the two is located at the position where the probability density functions of both classes are similar. The difference of this quadratic decision boundary to the other multivariate Gaussian classification explained above is that a quadratic covariance matrix is used, instead of a linear one.

Morphological opening of image

Morphological opening of a selection in an image is an image analysis tool. This tool will first erode a set number of points of the edges of the selection. After the erosion a new edge is created by dilating the edges of the eroded selection. This routine smooths the edges of a selected area.

Region Growing

Region growing is an image analysis tool, which is used to select an area that has a similar color. A seed point (pixel) is used as the input for region growing. The routine then adds one of the neighboring pixels that resemble the color of the initial seed point the most to the selection. Now the average color of the resulting selection is calculated and again a neighboring pixel is added to the selection that resembles the average color of the selection best. This routine keeps adding neighboring pixels, until no neighboring pixel is within a set color difference between the average color of the selection, i.e. until the threshold value is reached.

Chi-Squared variance test

The chi-squared variance test is a statistical tool to compare two sets of variances; reduced chi-squared tests have previously been evaluated by *Taylor (1982)*. In this project, the variance of the error caused by the methods proposed is compared to the error present in the null model. By using a quadratic best fit function on the data, an estimation of the scatter could be calculated. In this case the scatter is approximated as the error compared to the best fit model, this assumption is not always correct, but it does provide a method to quantify the scatter and bias.

The formula used to calculate the chi-squared of the total error, the scatter and the bias compared to the error of the null model can be seen in Equation 9, Equation 10 and Equation 11 respectively.

Equation 9

$$\mathrm{X}_{\mathrm{tot}}^{2} = (n-1)\frac{\sum(K_{model} - k_{measured})^2}{\sum(K_{measured} - K_{null})^2}$$

In Equation 9 the numerator represents the total error made by the model (i.e. the difference between estimated and measured permeability). The denominator represents the inherent scatter in the data, which is the difference between the measured permeability and the null model (the mean of the plug permeability per facies). Thus this equation gives a X^2 value for the total error of the model versus the inherent scatter in the data.

Equation 10

$$X^2_{\text{scatter}} = (n-1)\frac{\sum(K_{model} - \overline{K_{bestfit}})^2}{\sum(K_{measured} - K_{null})^2}$$

In Equation 10 the numerator represents the scatter in the models estimated permeability; this is the difference between the models estimated permeability and a (quadratic) best fit model through the mean values of the facies. The best fit model represents the bias of the model and could be accounted for if calibrated correctly, whereas the scatter cannot be accounted for with a calibration. The denominator again represents the inherent scatter in the data.

Equation 11

$$X^2_{\text{bias}} = X^2_{\text{tot}} - X^2_{\text{scatter}}$$

Because X^2 values can be subtracted from each other, the bias can be estimated by subtracting the value of X^2 for scatter from the value of X^2 of the total error.

The resulting X^2 can be converted to a P-value that indicates if the error of the model is significantly larger or smaller compared to the inherent error. This Chi-Squared test will be performed on the plug data and the Pressure Decay Profile Permeameter data for each facies (as observed by the geologist) separately.

Appendix G

This appendix gives a more detailed about the extraction of the bedding direction from the core images and subsequent segmentation of the core into centimeter thick segments.

Segmenting in centimeter thick layers

The bedding direction of the core needs to be extracted to enable segmentation of the core parallel to bedding. Multiple attempts were made to extract the bedding direction and the method with the best result was eventually chosen. The workflow of this method can be seen in Figure 57.

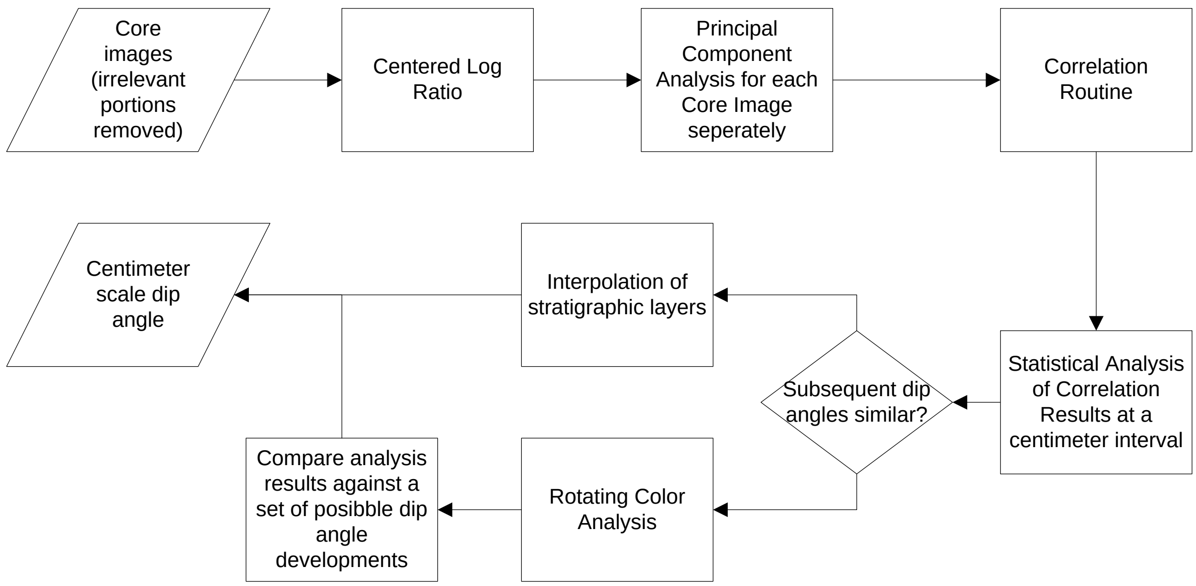

Figure 57: Workflow diagram of process 1.2: Segmenting in centimeter thick layers

Centered Log Ratio

The RGBD color data of each core image first undergoes a Centered Log Ratio (CLR) transformation, making the data continuous over the RGBD interval. The transformation also gives a better separation of color near the top and bottom of the RGBD-color space, because it stretches these intervals. These two consequences of the CLR transformation aid separation between stratigraphic layers and make subsequent calculations more reliable.

Principal Component Analysis

Following the CLR transformation, a Principal Component Analysis (PCA) is performed on the CLR transformed RGBD data of each core slab individually. The idea behind this is that the PCA locates the ‘odd’ areas in the image and gives a good separation between different colors. The mean color in a core image is given a score close to 0 and the less common colors are given a score significantly different from 0.

The assumption is made that color is relatively similar when evaluated parallel compared to perpendicular to the stratigraphic layers. This assumption implies that the PCA enhances the separation parallel to the stratigraphic layers.

Because the first principal component contains the strongest signal (i.e. captures the most variation) of the color data, this Principal Component is used in further analysis. The result of the PCA is a matrix that contains the first Principal Component score for each pixel in the core image.

Correlation Routine

PCA provides a means of separating intervals with different color characteristics and the next task is to find the dip angle between these differently colored intervals. This is performed by correlating two lines that are both parallel to depth. The advantage of applying a correlation is that a P-value and a Pearson Coefficient can be extracted for each correlation. The P-value is a measure of the significance of the correlation and a threshold can be used to discard all insignificant measurements. If the Pearson Coefficient is very low, this implies that the dependence between the lines that are correlated is very low. This means that correlations that are performed in for example homogeneous rock can be discarded, because the significance of the correlation is very low.

It is chosen to correlate lines that are equidistant from the center of the core, to aid comparison between multiple correlations.

Another choice that was made is to perform correlations at multiple distances L_y from the core's center (see Figure 59). The reason for this is that an erroneous dip angle could be extracted in areas where cross-bedding repeats itself (see Figure 58). A single correlation could not differentiate between these correct erroneous angles, whereas multiple correlations at different distances from the core's center (L_y) could. The distances from the core's center (L_y) that are chosen range from 1 cm from the center to 3 mm from the edge of the core with a step size of 1.5 mm. A distance L_y of less than 1 cm could induce errors caused by local heterogeneity.

The step size of 1.5 mm is chosen to be able to have a substantial set of data points at the plughole locations, where no correlation near the core's center can be performed. The correlation is performed for an angle α of -45 to 45 degrees; the reason is to reduce processing time and memory space, because the core does not contain any dip angles larger than 38 degrees.

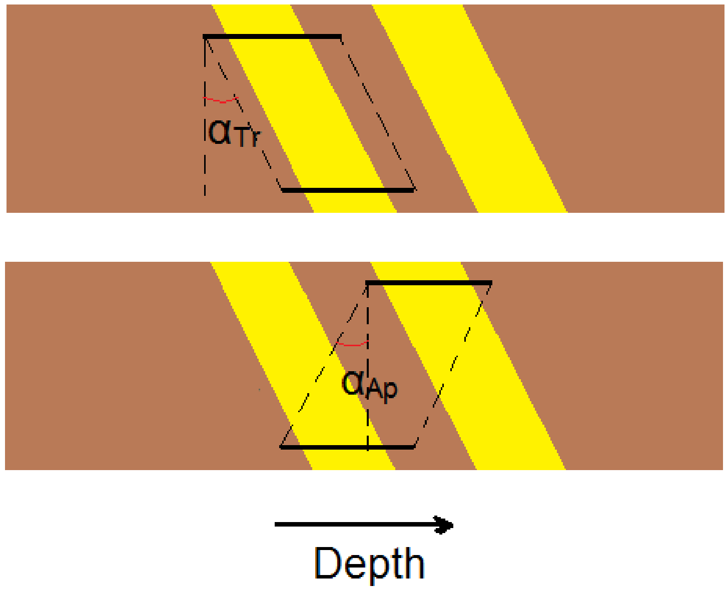

Figure 58: Schematic representation of a core visualizing an incorrectly extracted angle α_{Ap} from correlation due to repeating bedding. In this case the Pearson coefficient r_p of the correlations that obtain the true angle α_{Tr} and the apparent angle α_{Ap} can have similar values.

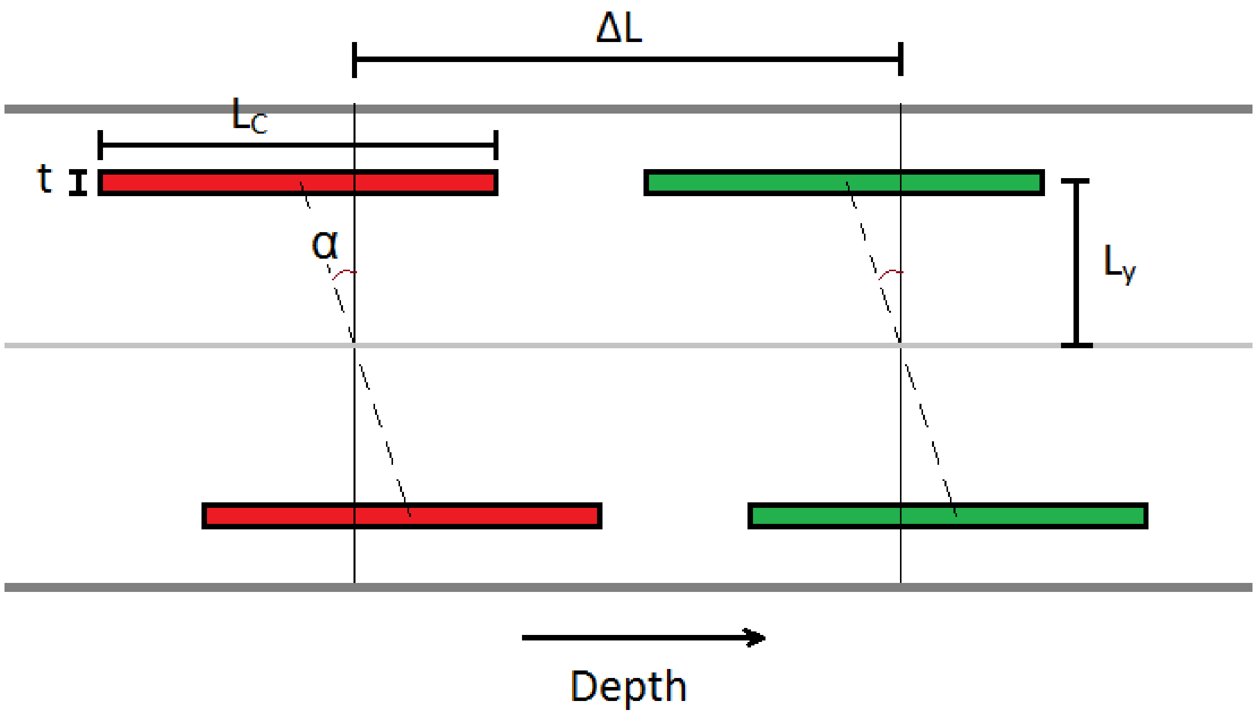

Figure 59: Schematic representation of the correlation performed on the core. Two correlations are shown; a correlation between the red lines and a correlation between the green lines. In this figure α is the angle, L_c is the correlation length, L_y is the distance from the center of the core, ΔL is the step size between correlations and *t* is the thickness of the correlation line.

Because some stratigraphic layers are thicker than others, correlation is performed for multiple correlation lengths L_c (Figure 59). The decision was made to set the correlation length L_c to a minimum of 1.5 cm to capture the smallest layers. The maximum correlation length was set to 6 cm, which is the size needed to capture larger layers and any trends in the color (i.e. subtle darkening), but this size will not smooth the results to such an extent that is unpractical in subsequent division in centimeter thick layers.

Because a large part of the rock samples constitute of siliciclastics, the grains introduce a kind of noise in the correlation. To account for this, the area over which the correlation is performed is averaged perpendicular to depth; this is done over a thickness *t* of 0.5 mm, because this thickness showed the best result.

Averaging over the thickness might result in slight errors when the bed slope is high, because it will average pixels that are not parallel to the bedding, but the positive effect of smoothing is larger than the errors caused by this effect. At a larger size of *t* this negative effect will become more of a problem; this is why the correlation thickness t was chosen to be 0.5 mm, which in terms of average grain size is 8 and 0.5 grains for the finest and coarsest sandstone present in the core respectively.

To be able to obtain independent measurements at the same correlation lengths, the step size ΔL was set to 2/3 the size of the correlation length L_c. An overview of all the property values used is given in Table 21.

Table 21: Overview of Correlation variables, the step size for the Angle given as <1, but cannot be given exact as the correlation is performed at a step size of 1 pixel, which makes the step size in terms of an angle dependent on L_y.

Variable	Symbol	Minimum value	step size	Maximum value
Correlation Length	L_C	1.5cm	1.5 cm	6 cm
Correlation Thickness	t	0.5 mm	-	-
Half Distance between correlations	L_y	1 cm	1.5 mm	3-3.5 cm
Step size	ΔL	2/3 L_C = 1 cm	1 cm	2/3 L_C = 4 cm
Angle	α	-45	<1 (1 pixel)	45

This full correlation routine is executed twice, with the difference between the two executions that the offset is half the size of the correlation length L_c. making it possible to double-check the results. These two sets are hereafter referred to as set A and set B. Thus the final result of this process is two sets of correlation results at different distances from the center and at different correlation lengths.

Statistical analysis of correlation results

Because a large part of the correlation is performed on homogeneous rock, the results of the correlation in these areas are unreliable. This expresses itself in the P-value for the correlation, which is a measure of significance of the correlation. A low significance means that the correlation has a relatively large chance to be caused by chance. Another measure of the reliability expresses itself in the Pearson Coefficient. If the Pearson Coefficient is low, it indicates a low dependence between the variables, thus both variables might not be correlated at all.

The Critical Pearson Coefficient (i.e. Pearson Coefficient at which the significance α is below 5 %) depends on the number of observations. In this case the observations are the number of pixels across the correlation length. All correlations with a Pearson coefficient below the critical Pearson Coefficient are discarded. Insignificant correlations with a P-value above 1% are discarded as well.

Now that all correlations that do not contain reliable data are discarded, the results are analyzed. The reliable correlations are evaluated and the offset between the two parallel lines at which the correlation is highest is converted to a dip angle. These dip angles are compared for each correlation length at each step ΔL (for set A en B separate). If the standard deviation of the dip angles is small, implying that the dip angles are similar a 'maximum correlation angle' (α_{max}) is assigned. Otherwise the 'maximum correlation angle' is unassigned.

The interval at which the angle α_{max} is assigned is irregular and angles are only assigned when a clear bedding was detected by the correlation. It was arbitrarily chosen to extract image analysis properties at a centimeter interval, which means that the core should be split up into centimeter thick segments as well. To be able to do this, centers of the edges of segments are set at a centimeter interval. For each of the segments edges the closest value for α_{max} (assigned or unassigned) at each correlation length is assigned. When values for α_{max} are similar for more than one correlation length, this value is assigned to the edge (for set A and B separate).

Finally the results of set A and set B are compared and at the locations where they are within 1 degrees difference, a final 'reliable' angle is assigned to the segments edges, otherwise no angle is assigned.

The result of this statistical analysis is a list of dip angles at a centimeter scale interval, where the dip angle is only assigned if the correlation results show a reliable result. This results in assigned dip angles where the color characteristics of the core change (i.e. where the bedding or boundaries of stratigraphic layers can be detected).

Interpolation of dip angles

Now that 'reliable' dip angles are obtained at certain intervals, these angles have to be interpolated, to obtain a full record of the dip angle.

If subsequent 'reliable' dip angles are similar within 2 degrees, it is assumed that the bedding will stay similar and straightforward interpolation is applied. If the dip angles are not similar within 2 degrees, the following assumption is made: the dip angle will either show a gradual change or a discontinuity is present in between the two 'reliable' angles. The decision between one of these scenarios is made based on a subsequent analysis; first a PCA is performed on the CLR transformed color data of the section between the two angles, amplifying any areas that show different color characteristics.

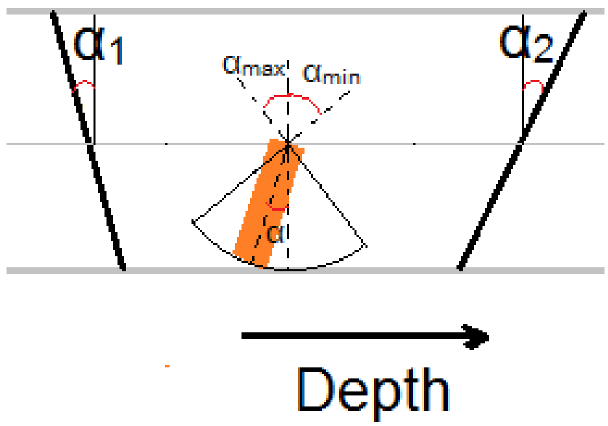

Figure 60: Schematic representation of a core segment showing the routine that estimates the angle between two 'reliable' angles. α_1 and α_2 are the respective 'reliable' angles. α_{min} and α_{max} represent the range of angles α at which measurements are performed

Next an area is rotated from angle α_{min} to α_{max} (See Figure 60) and the standard deviation of the first principal component of the CLR transformed color data is calculated in an area half the width of the core and with a thickness of 0.5 mm (the orange area in Figure 60). This calculation is performed at a 0.5 cm interval between α_1 and α_2 and at a stepsize of 0.5 degrees for α. The routine is performed for the top and bottom half of the core separately, to enable to detection of discontinuities.

α_{min} to α_{max} are two degrees larger and smaller than the largest and smallest 'reliable' angle α_1 and α_2 respectively.

The standard deviation of color is now obtained for plausible bedding direction in between the two 'reliable' angles. For each 0.5 cm interval the angle α that result in the minimum standard deviation is extracted. The resulting angles of this extraction are compared to the plausible dip angle scenarios (gradual change or discontinuity) and the scenario that shows the best fit is chosen.

The dip angle of the segments between two 'reliable' angles that are located in different core images is performed by simple interpolation (based on depth difference). It was not chosen to use the above described routine in these areas, because the different images do not line up perfectly. This would otherwise cause a dip angle model that is less reliable than the model obtained by simple interpolation. The average CPU time used to extract the bedding direction per core is about 35 minutes (CPU: 3 GHz).